



저작자표시-비영리-변경금지 2.0 대한민국

이용자는 아래의 조건을 따르는 경우에 한하여 자유롭게

- 이 저작물을 복제, 배포, 전송, 전시, 공연 및 방송할 수 있습니다.

다음과 같은 조건을 따라야 합니다:



저작자표시. 귀하는 원저작자를 표시하여야 합니다.



비영리. 귀하는 이 저작물을 영리 목적으로 이용할 수 없습니다.



변경금지. 귀하는 이 저작물을 개작, 변형 또는 가공할 수 없습니다.

- 귀하는, 이 저작물의 재이용이나 배포의 경우, 이 저작물에 적용된 이용허락조건을 명확하게 나타내어야 합니다.
- 저작권자로부터 별도의 허가를 받으면 이러한 조건들은 적용되지 않습니다.

저작권법에 따른 이용자의 권리는 위의 내용에 의하여 영향을 받지 않습니다.

이것은 [이용허락규약\(Legal Code\)](#)을 이해하기 쉽게 요약한 것입니다.

[Disclaimer](#)

Doctor of Philosophy

**A Study on the Improvement of Water Splitting
Performance of Transition Metal-Based Electrocatalysts**

The Graduate School of the University of Ulsan

Department of Chemical Engineering

Ngoc-Diem Huynh

**A Study on the Improvement of Water Splitting
Performance of Transition Metal-Based Electrocatalysts**

Supervisor: Professor Seung Hyun Hur

A Dissertation

Submitted to

The Graduate School of the University of Ulsan

In Partial Fulfillment of the Requirements for the Degree of

Doctor of Philosophy

by

Ngoc-Diem Huynh

Department of Chemical Engineering

University of Ulsan, Korea

May 2024

A Study on the Improvement of Water Splitting Performance of Transition Metal-Based Electrocatalysts

This certifies that the dissertation of Ngoc-Diem Huynh is approved.



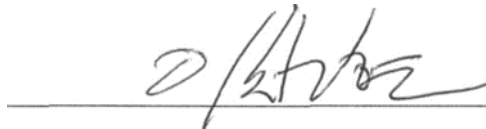
Committee Chair Professor Sung Gu Kang



Committee Member Professor Seung Hyun Hur



Committee Member Professor Won Mook Choi



Committee Member Professor Chan Hyun Lee



Committee Member Professor Mun Ho Kim

Department of Chemical Engineering

University of Ulsan, Korea

May 2024

ABSTRACT

Hydrogen energy is attracting attention not only due to its various applications but also because it is a green and sustainable energy source. Water splitting is an efficient method for producing hydrogen. Therefore, identifying suitable electrocatalysts for both the hydrogen evolution reaction (HER) and the oxygen evolution reaction (OER) in the water splitting process is essential. Despite the effectiveness of noble metal-based electrocatalysts, their high cost and scarcity pose significant challenges. Hence, there is a critical need for active, stable, and cost-effective electrocatalysts for water splitting.

Driven by this challenge, this study focused on improving transition metal-based electrocatalysts for water splitting applications, with a particular emphasis on reducing costs and enhancing sustainability compared to noble metal-based electrocatalysts. Through various methodologies, including the optimization of activity and stability in both the hydrogen evolution reaction (HER) and oxygen evolution reaction (OER), significant progress was made.

We synthesized heterostructure catalysts, combining multiple components to leverage synergistic effects and overcome individual limitations. Furthermore, we explored depositing active component catalysts onto supported two-dimensional (2D) materials to enhance catalytic activity, stability, and mass transport properties. Additionally, modulation of electronic structures was investigated by introducing rare element-based materials as promoter components to enhance electrocatalyst activity and stability. Moreover, we investigated the benefits of atomic geometries of the compounds containing anion phosphate group and cation transition metals. The flexible coordination of this anion and the various oxidation states of transition metal can stabilize the intermediates in water splitting reactions, facilitating favorable adsorption and oxidation of water molecules.

These findings collectively demonstrate promising advancements in transition metal-based electrocatalysts for water splitting, highlighting their potential for widespread adoption in green hydrogen technologies. Through cost-effective and sustainable approaches, this research contributes to the advancement of efficient and scalable methods for hydrogen production.

ACKNOWLEDGEMENT

It would be my pleasure to take this opportunity to express my thankfulness to every who supported me in finishing my thesis.

Foremost, I extend my heartfelt appreciation to Professor Seung Hyun Hur, my supervisor, for his unparalleled expertise and invaluable guidance during the entirety of my research journey. His insightful advice and feedback have improved my thinking and are valuable to my research.

I wish to express my gratitude to my esteemed committee members, Professor Sung Gu Kang, Professor Won Mook Choi, Professor Chan Hyun Lee, and Professor Mun Ho Kim, for their insightful critique and encouragement during the thesis defense.

Furthermore, I am thankful to Mrs. Kyung Jo Lim and all staff members of the Department of Chemical Engineering for their dedication and collaboration. In addition to these thank you notes, I would like to express my gratitude to my labmates Yen-Linh Thi Ngo, Jayasmita Jana, Ravi Nivetha, Aniruddha Jaiswal, Le Van Nam, Tran Van Phuc, Nguyen Duc Viet, and Thai Thi Dac Ngan for their great support and friendships.

Finally, I would like to acknowledge the encouragement and support I have received from family and my friends in the Department of Chemical Engineering and from other Departments at the University of Ulsan, which has been a valuable source of inspiration for me.

TABLE OF CONTENTS

Part 1. Overview of dissertation.....	1
Chapter 1. Introduction.....	1
1.1. Overview	1
1.1.1. Energy demand	1
1.1.2. Hydrogen energy.....	3
1.1.3. Water splitting.....	5
1.1.4. Electrocatalyst.....	10
1.1.5. Motivation.....	18
1.1.6. Research objectives.....	19
1.2. Outline of dissertation	19
Part 2. Depositing the active component on the 2D materials	21
Chapter 2. 2D Siloxene supported NiO/Co ₃ O ₄ electrocatalyst for the stable and efficient hydrogen evolution reaction.....	21
2.1. Introduction	21
2.2. Experimental details	22
2.2.1. Material	22
2.2.2. Instrumental analysis	23
2.2.3. Preparation of working electrode and electrochemical measurements	23
2.2.4. Synthesis of Siloxene.....	24
2.2.5. Synthesis of NiO/Co ₃ O ₄ @Siloxene	24
2.3. Results and discussion.....	25
2.3.1. Characterization of Siloxene, NiO/Co ₃ O ₄ , and NiO/Co ₃ O ₄ @Siloxene	25
2.3.2. Electrochemical activity of NiO/Co ₃ O ₄ @Siloxene towards hydrogen evolution reaction	33
2.4. Conclusion.....	40
Chapter 3. Exploring the Effects of Various Two-Dimensional Supporting Materials on the Water Electrolysis of Co-Mo Sulfide /Oxide Heterostructure	41
3.1. Introduction	41
3.2. Experimental details.....	42
3.2.1. Material.....	42

3.2.2.	Instrumental analysis	43
3.2.3.	Preparation of working electrode and electrochemical measurements	43
3.2.4.	Synthesis of Co-glycerate precursor	45
3.2.5.	Synthesis of two-dimensional (2D) materials	45
3.2.6.	Synthesis of CMSO@2D	45
3.3.	Results and discussion.....	47
3.3.1.	Characterization of prepared materials	47
3.3.2.	Electrochemical activity of CMSO@2D towards oxygen evolution reaction ..	54
3.4.	Conclusion.....	61
Part 3.	Modulating the electronic structure	62
Chapter 4.	Influence of Er ₂ O ₃ on Transition Metal Oxides in Water oxidation application ..	62
4.1.	Introduction	62
4.2.	Experimental details	63
4.2.1.	Material	63
4.2.2.	Instrumental analysis	63
4.2.3.	Preparation of working electrode and electrochemical measurements	64
4.2.4.	Synthesis of ErMO (M=Ni, Co, Fe).....	65
4.3.	Results and discussion.....	66
4.3.1.	Characterization of ErMO (M=Ni, Co, Fe).....	66
4.3.2.	Electrochemical activity of ErMO (M=Ni, Co, Fe) towards oxygen evolution reaction	79
4.4.	Conclusion.....	89
Part 4.	Modifying atomic geometries by phosphate group	90
Chapter 5.	Iron-Tin phosphate electrocatalyst applied for bifunctional water splitting	90
5.1.	Introduction	90
5.2.	Objectives.....	91
5.3.	Methodology	91
5.3.1.	Synthesis of Iron-tin Phosphate-Based Electrocatalyst.....	91
5.3.2.	Characterization	93
5.3.3.	Electrocatalytic Performance Evaluation.....	93
5.4.	Expected Outcomes.....	93

Part V: Summary.....	94
Part VI: Recommendations for future work.....	96
List of publications.....	110

LIST OF FIGURES

Figure 1.1: World primary energy demand by fuel (Source: IEA, WEO-2011).....	2
Figure 1.2: World CO ₂ emissions from fuel combustion by fuel, 1971-2019 (Mt of CO ₂)	2
Figure 1.3: Hydrogen energy applications	4
Figure 1.4: Grey, blue and green hydrogen production (Source: energy education)	4
Figure 1.5: HER mechanism in alkaline media (Source: reference [13])	7
Figure 1.6: (a) Relationship between j_0 and ΔG_{H^*} under the assumption of a Langmuir adsorption model (Source: reference [12]), and (b) Volcano plot for HER in alkaline medium for various metals (Source: reference [14]).....	7
Figure 1.7: (a) AEM, and (LOM) mechanism (Source: reference [13])	9
Figure 1.8: Volcano-shaped activity plot of the OER for oxides (Source: reference [19]).....	9
Figure 1.9: the polarization curves of OER (right) /HER (left). Inset is the Tafel plot obtained from the corresponding polarization curve (Source: reference [21])	11
Figure 1.10: (a) a time-dependent potential creates an alternating current, and (b) Nyquist plot (Source: reference [22])	13
Figure 1.11: Randles equivalent electrical circuit over a wide frequency range.....	13
Figure 1.12: the structure of dissertation.....	20
Figure 2.1: a) FT-IR spectra, (b) Raman spectra, (c) XRD pattern, and (d) N ₂ adsorption–desorption isotherms of as-prepared samples	27
Figure 2.2: FESEM images of (a) Siloxene, (b) NiO/Co ₃ O ₄ , (c) NiO/Co ₃ O ₄ @Siloxene, and (d-g) element mapping of NiO/Co ₃ O ₄ @Siloxene	29
Figure 2.3: HRTEM lattice-fringe image of NiO/Co ₃ O ₄ @Siloxene	29

Figure 2.4: XPS spectra of (a) Si 2p, (b) O 1s, (c) Ni 2p, and (d) Co 2p of prepared materials	31
Figure 2.5: XPS spectra of (a) Si 2p, and (b) O 1s of NiO/Co ₃ O ₄ @Siloxene	31
Figure 2.6: Broad range XPS spectra of prepared materials	32
Figure 2.7: (a) LSV curves, (b) Tafel slopes, (c) Nyquist plots, and (d) Linear fit of the current density as a function of the scan rates	35
Figure 2.8: Corresponding J _{geo} , J _{ECSA} , and J _{BET} at -0.5 V vs. RHE of synthesized materials	35
Figure 2.9: TOF values at the overpotential of -0.1 V, at scan rate 50 mV/s by using the methods reported previously [47]	36
Figure 2.10: (a) Chronopotentiometry at 10 mA/cm ² , (b) LSV curve before and after the stability test (c) XRD pattern, and (d) FESEM image of NiO/Co ₃ O ₄ @Siloxene after stability test	39
Figure 2.11: XPS spectra of (a) Ni 2p, (b) Co 2p, and (c) Raman spectra of NiO/Co ₃ O ₄ @Siloxene after stability test	39
Figure 3.1: Calibration of Hg/HgO electrode	44
Figure 3.2: (a) XRD patterns and (b) Raman spectra of various materials	48
Figure 3.3: Raman spectrum of (a) rGO, (b) gC ₃ N ₄ , and (c) SiSh	48
Figure 3.4: (a) N ₂ adsorption–desorption isotherms of various materials, and (b) Pore size distribution by density functional theory method of various materials	50
Figure 3.5: FESEM images of (a) CMSO, (b) CMSO@rGO, (c) CMSO@ gC ₃ N ₄ , and (d) CMSO@SiSh	51
Figure 3.6: Deconvoluted high-resolution XPS spectra of (a) Mo 3d, (b) Co 2p, (c) S 2p, and (d) O 1s of various materials	53

Figure 3.7: (a) LSV curves, (b) Comparison of the overpotential at 10 mA/ cm ² , (c) Tafel slope, (d) Linear fitting of the current density against scan rates, (e) Nyquist plots of various materials. (f) Comparison of the overpotential and Tafel slope of CMSO@rGO with [148-159] in OER.	55
Figure 3.8: Cyclic voltammetry curves at scan rates from 20 to 100 mV/s of prepared materials	55
Figure 3.9: Comparison of BET and ECSA of synthesized materials	56
Figure 3.10: (a) Chronoamperometry curves of CMSO (at 1.60 V), CMSO@rGO (at 1.49 V), CMSO@ gC ₃ N ₄ (at 1.50 V), and CMSO@SiSh (at 1.52 V). (b) LSV curves of CMSO@rGO before and after a 40-h stability test	59
Figure 3.11: FESEM of CMSO@rGO at different magnification after OER	59
Figure 3.12: Comparison of (a) Raman spectrum, (b) XRD pattern, and (c) XPS of Co 2p of CMSO@rGO before and after OER	59
Figure 3.13: (a) LSV curves of two-electrode systems, (b) Chronopotentiometry curve for the overall water splitting reaction at 10 mA/ cm ² (inset photograph: CMSO@rGO(anode)//Pt/C(cathode); the overall water splitting system).....	60
Figure 4.1: (a) XRD patterns and (b) Raman spectra of the synthesized materials	67
Figure 4.2: (a) FTIR spectra and (b) N ₂ adsorption–desorption isotherms of the as-prepared samples.....	69
Figure 4.3: Pore size distribution by density functional theory method of (a) NiO, ErNiO, (b) Co ₃ O ₄ , ErCoO, and (c) Fe ₂ O ₃ , ErFeO	69
Figure 4.4: FESEM of Er ₂ O ₃	71
Figure 4.5: FESEM of (a) NiO, (b) ErNiO; (c) Co ₃ O ₄ , (d) ErCoO; (e) Fe ₂ O ₃ , and (f) ErFeO... 71	
Figure 4.6: Elemental mapping of (a-d) ErNiO, (e-h) ErCoO, and (i-l) ErFeO.....	71

Figure 4.7: HRTEM of (a,b) ErNiO, (c,d) ErCoO, and (e,f) ErFeO	73
Figure 4.8: XPS survey spectra of prepared materials	75
Figure 4.9: XPS spectra of (a) Ni 2p, (b) O 1s of NiO and ErNiO; (c) Co 2p; (d) O 1s of Co ₃ O ₄ and ErCoO; and (e) Fe 2p, (f) O 1s of Fe ₂ O ₃ and ErFeO.....	76
Figure 4.10: XPS spectra of Er 4d of prepared materials.....	77
Figure 4.11: (a) EPR spectra and (b) g-factor of the synthesized materials.....	78
Figure 4.12: (a) LSV curves, (b) Comparison of overpotential, (c) Tafel slope, (d) Nyquist plots, and (e) Linear fitting of current density against scan rates of the synthesized materials.....	81
Figure 4.13: the cyclic voltammetry in the non-faradaic region of OER of synthesized materials	82
Figure 4.14: (a) Chronopotentiometry of various materials at 10 mA/cm ² , and (b) LSV curve of ErFeO before and after 30 h of stability testing.....	85
Figure 4.15: (a) FESEM, (b) XRD pattern, and (c) XPS of Fe 2p, and (d) XPS of O 1s of ErFeO before and after OER	85
Figure 4.16: (a) LSV curve of two-electrode systems, and (b) CP for overall water splitting at 10 mA/cm ² of the ErFeO Pt/C system.....	86
Figure 4.17: (a) LSV curves, (b) Chronopotentiometry at 10 mA/cm ² , and (c) comparison of activity retention after 30h OER operation and overpotential at 10 mA/cm ² of ErFeO (x) (x=1/1, 1/4, 1/8, 1/12, and 1/16).....	88
Figure 4.18: (a,b) the cyclic voltammetry in the non-faradaic region of OER, (b) Linear fitting of current density against scan rates, and (d) Nyquist plots of ErFeO (1/12) and (1/16).....	88

LIST OF SCHEMES

Scheme 3.1: Schematic of CMSO and various CMSO@2D materials (2D materials: rGO, gC ₃ N ₄ , and SiSh).....	46
Scheme 5.1: synthesis procedure of iron-tin phosphate	92

LIST OF TABLES

Table 2.1: The pore volume and pore size of prepared materials calculated by using non-local density functional theory method (NLDFT)	26
Table 2.2 ; composition of O, Si, Co, and Ni (At. %) elements present in NiO/Co ₃ O ₄ @Siloxene as recorded by XPS analysis	30
Table 2.3: Activities of the as-synthesized materials toward the HER	34
Table 2.4: Comparison of HER activity in 1 M KOH of different electrocatalyst.....	38
Table 3.1: Specific surface area, pore volume, and pore radius of various materials	49
Table 3.2: OER properties and interfacial charge transfer resistance of various materials.....	56
Table 3.3: Comparison of OER activity in 1 M KOH of different electrocatalyst.....	57
Table 4.1: Specific surface area, pore volume, and pore radius of the synthesized materials....	68
Table 4.2: XPS results of all the materials	75
Table 4.3: The summarized activities of the synthesized materials toward the OER	80
Table 4.4: Comparison of OER activity in 1 M KOH of different electrocatalyst.....	80
Table 4.5: XPS results of ErFeO before-after OER process	83

NOMENCLATURES

RE	Renewable energy
HER	Hydrogen evolution reaction
OER	Oxygen evolution reaction
RHE	Reversible hydrogen electrode
TMOs	Transition metal oxides
rGO	Reduced graphene oxide
gC ₃ N ₄	Graphitic carbon nitride
SiSh	Siloxene
XRD	X-ray diffraction
XPS	X-ray photoelectron spectroscopy
FT-IR	Fourier transform infrared spectra
EPR	Electron paramagnetic resonance
BET	Brunauer-Emmett-Teller equation
FESEM	Field emission scanning electron microscopy
HRTEM	High resolution transmission electron microscopy
NF	Nickel foam
WE	Working electrode
CV	Cyclic voltammetry
LSV	Linear sweep voltammetry
EIS	Electrochemical impedance spectroscopy
ECSA	electrochemical active surface area
C _{dl}	Double layer capacitance
C _s	Specific capacitance

Part 1. Overview of dissertation

Chapter 1. Introduction

1.1. Overview

1.1.1. Energy demand

Over the years, the energy demand has increased alongside population growth, industrial expansion, and technological advancements. It can be seen in **Figure 1.1** that the total primary energy demand was forecasted to increase by 40% over the outlook period to reach more than 16,950 Mtoe in 2035 [1]. Predominantly sourced from fossil fuels such as coal, oil, and natural gas. These energy sources are used for many sectors including residential/commercial, electricity generation, transportation, and industries. Their prevalence owes to their accessibility, affordability, and the existing infrastructure supporting their utilization [2]. Despite various benefits, the use of fossil fuels confronts significant environmental and social drawbacks, energy source depletion, air and water pollution, greenhouse gas emissions, climate change, and health impacts. **Figure 1.2** exhibited a substantial rise in CO₂ emissions between 1971 and 2019 attributed to fossil fuel usage. Consequently, the exploration of alternative energy sources to alter fossil fuel becomes imperative.

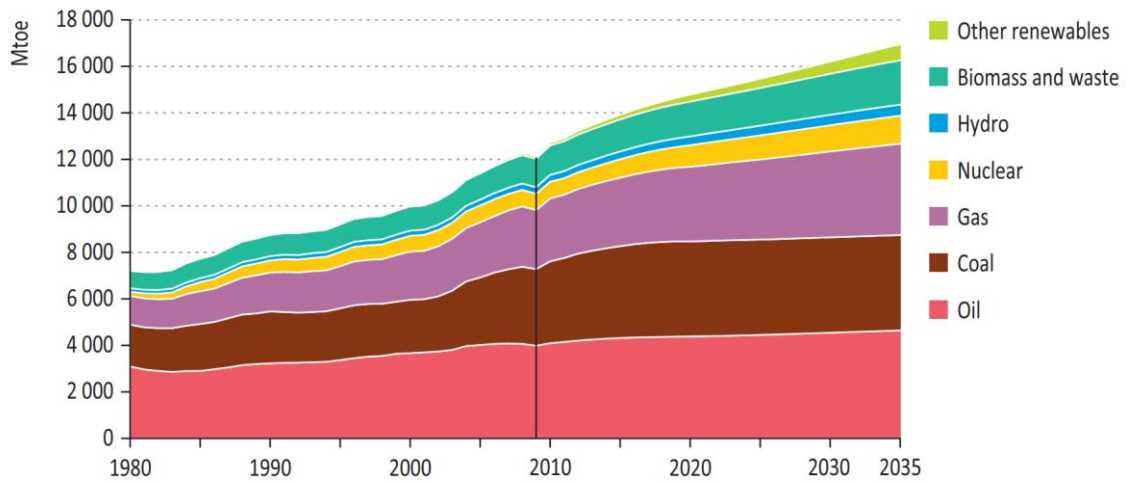


Figure 1.1: World primary energy demand by fuel (Source: IEA, WEO-2011)

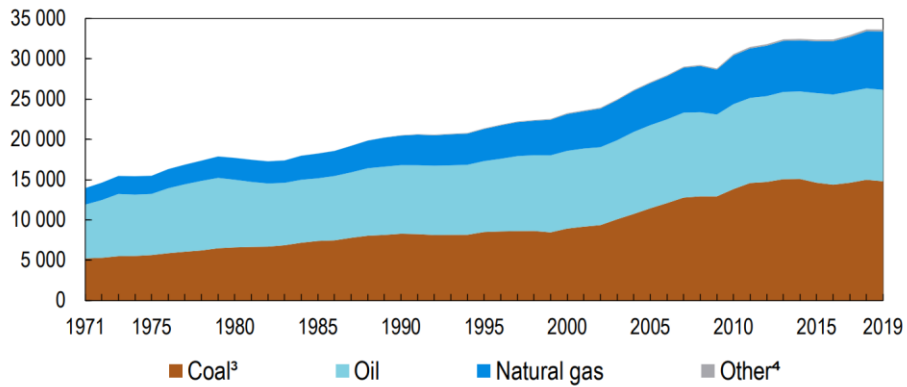


Figure 1.2: World CO₂ emissions from fuel combustion by fuel, 1971-2019 (Mt of CO₂) (Source: IEA, CO₂ Emissions from Fuel Combustion, 2021)

1.1.2. Hydrogen energy

Nowadays, renewable energy (RE) has been drawing attention for its sustainability, environmental friendliness, contribution to climate change mitigation, and potential to reduce reliance on fossil fuels. There are seven types of RE [3] encompassing: solar energy, wind energy, hydropower, tidal energy, bioenergy, geothermal energy, and hydrogen energy

Hydrogen emerges as a promising energy carrier, boasting high energy efficiency, emission-free attributes, and minimal environmental impact. The energy density of hydrogen is relatively high compared to other conventional fuels. Hydrogen has nearly three times the energy content of gasoline—120 MJ/kg for hydrogen versus 44 MJ/kg for gasoline [4]. Moreover, hydrogen can be stored in various forms including compressed gas, liquefied hydrogen, and chemical compounds like metal hydrides and ammonia, facilitating flexibility in storage method with suitable application [5]. Notably, its production can stem from both renewable and non-renewable energy sources, rendering it adaptable for various applications across diverse sectors, as demonstrated in **Figure 1.3** [6] [7].

Based on the method of production, hydrogen is categorized into three types [8] as shown in **Figure 1.4** [9]:

- **Grey/Black Hydrogen:** This type of hydrogen is primarily produced from fossil fuels, predominantly through processes like steam-methane reforming or methane reforming. A significant byproduct of this process is carbon dioxide (CO₂).
- **Blue Hydrogen:** Similar to grey hydrogen, blue hydrogen is also derived from fossil fuel feedstocks. However, the key distinction lies in the mitigation of CO₂ emissions through capture and underground storage.

Green Hydrogen: This form of hydrogen is generated using electricity from renewable sources such as solar or wind energy to conduct electrolysis. Unlike grey and blue hydrogen, green hydrogen production results in zero emissions. Currently, the majority of hydrogen production is the grey hydrogen [8]. To advance towards sustainable, environmentally friendly, and efficient energy practices, there is a pressing need to prioritize the investigation and development of green hydrogen technologies.

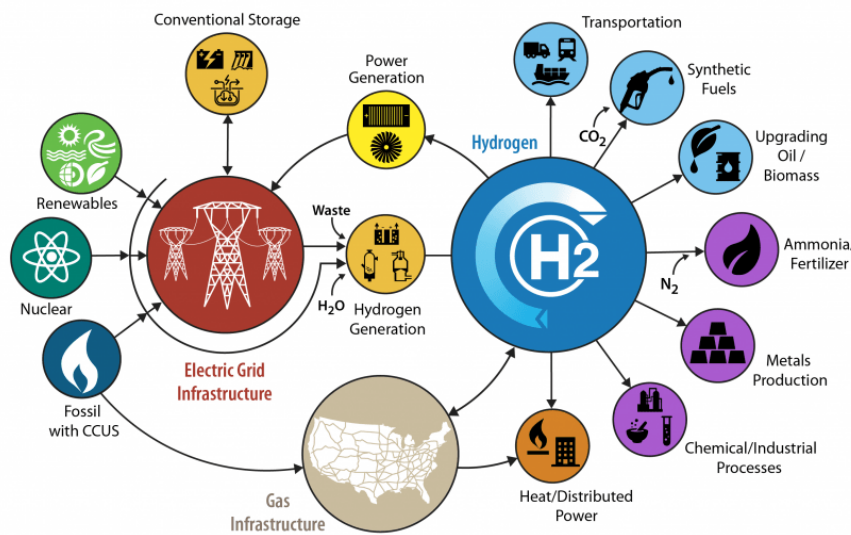


Figure 1.3: Hydrogen energy applications
(Source: Office of energy efficiency & renewable energy)

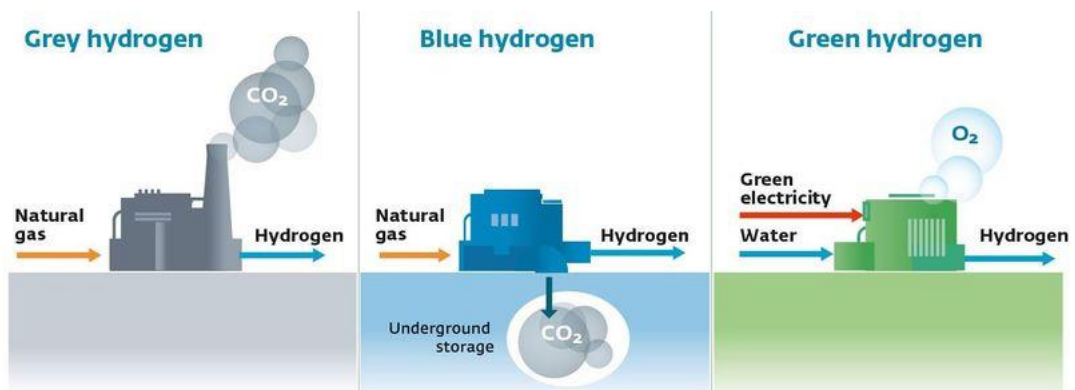


Figure 1.4: Grey, blue and green hydrogen production (Source: energy education)

1.1.3. Water splitting

Water splitting, also known as water electrolysis, is a method that employs electricity to divide water into hydrogen (H₂) and oxygen (O₂) gases as reaction (1). This process involves an electrolysis cell containing electrodes, an electrolyte, and an electric current. Within the cell, reduction reactions occur at the cathode, where H₂ gas is produced by gaining electrons, while oxidation reactions occur at the anode, leading to the production of O₂ gas through the loss of electrons.

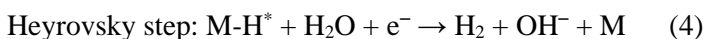
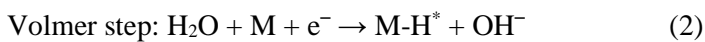
$$\text{H}_2\text{O (l)} \rightarrow \text{H}_2 \text{ (g)} + \frac{1}{2} \text{O}_2 \text{ (g)} \quad (1), \Delta G^\circ = +237.2 \text{ kJ mol}^{-1}, \Delta E^\circ = 1.23 \text{ V vs normal hydrogen electrode (NHE)}.$$

Hydrogen produced by electrolysis of water is of relatively high quality, as no carbon, sulfur, or nitrogenous compounds are generated in the process. Water is the most promising candidate for hydrogen resource because it contains more hydrogen (111 kg/m³)

The electrolyte in water splitting can be acid, alkaline or neutral media. In acidic media, hydrogen evolution benefits from the presence of H⁺ ions readily available, while in alkaline media, water needs to undergo dissociation to generate H⁺ ions for hydrogen formation [10]. Given this disadvantage, the focus of this thesis will be on investigating water electrolysis in alkaline environments.

Hydrogen evolution reaction

The hydrogen evolution reaction (HER) entails a two-electron transfer process and the standard electrode potential $E^0 = 0.00 \text{ V}$ [11]. In alkaline media, the mechanism of HER comprises the initial Volmer reaction, followed by either the Tafel or Heyrovsky reaction, as the following reactions and depicted in **Figure 1.5**:



Where M is electrocatalyst surface, H* is the adsorbed hydrogen atom.

The determination of the rate-determining step (RDS) of the hydrogen evolution reaction (HER) can be made based on the value of the Tafel slope (b). If the Volmer step (discharge reaction) is sluggish, the Tafel slope is expected to be around 120 mV/dec. Conversely, if the Tafel step, also referred to as the chemical desorption or combination reaction, is the limiting factor, the Tafel slope is typically lower, around 29 mV/dec. Alternatively, if the electrochemical desorption, often associated with the Heyrovsky reaction, governs the rate, the Tafel slope is expected to be around 39 mV/dec [11].

The key factor of HER is the free energy of hydrogen adsorption and desorption (ΔG_{H^*}). The hydrogen adsorption ability should not be too weak or too strong. According to the Sabatier principle, excessively strong binding between H^* and the electrocatalyst stabilizes H^* , hindering subsequent elemental steps. Conversely, if the binding is too weak, the Volmer step becomes RDS. The ideal ΔG_{H^*} should be zero with the highest HER j_0 as the top of the volcano, as shown in **Figure 1.6(a)** [12]. Based on **Figure 1.6(b)**, the Pt is near the peak of the volcano, and it is the benchmark material for the HER currently.

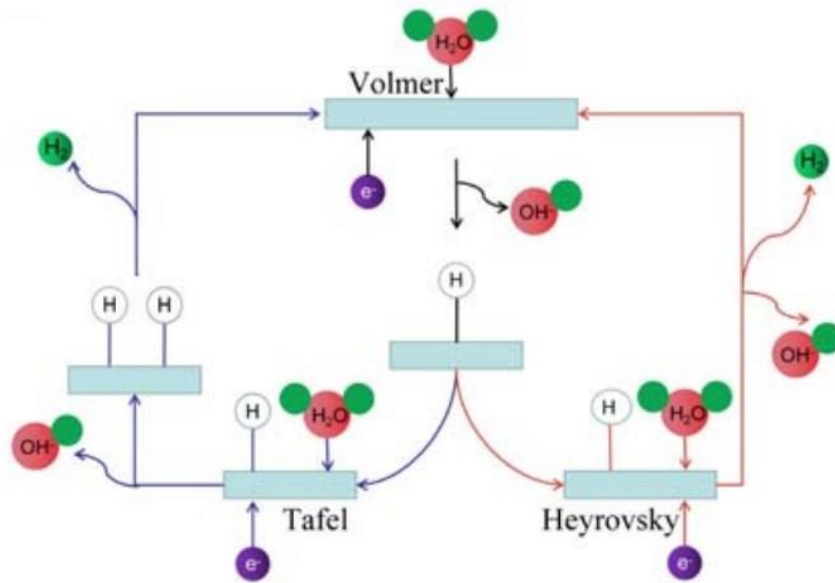


Figure 1.5: HER mechanism in alkaline media (Source: reference [13])

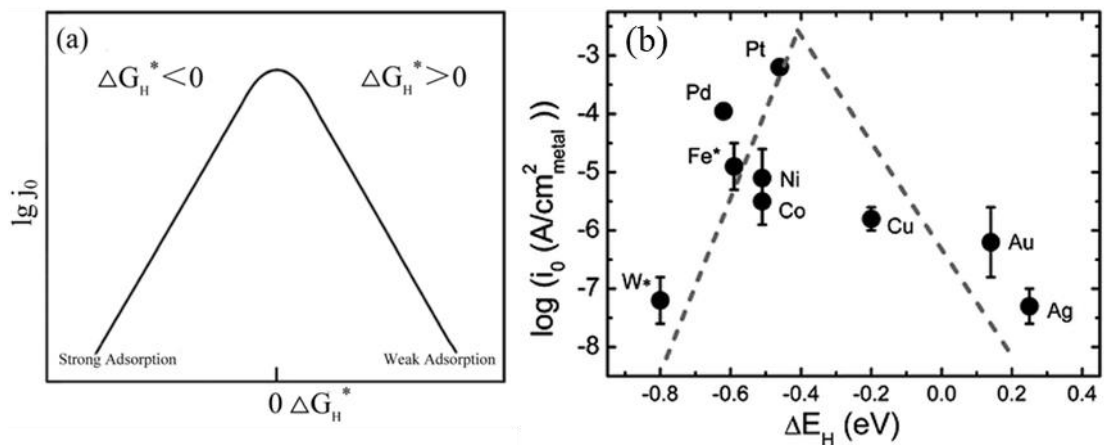
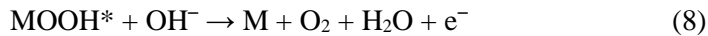
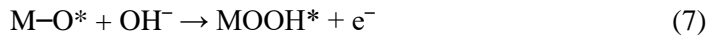
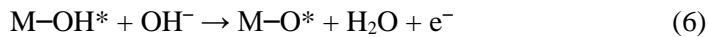


Figure 1.6: (a) Relationship between j_0 and ΔG_H^* under the assumption of a Langmuir adsorption model (Source: reference [12]), and (b) Volcano plot for HER in alkaline medium for various metals (Source: reference [14])

Oxygen evolution reaction

As mentioned OER is the half reaction in water splitting process at the anode, involving four-electron transfer reaction. With the $E^0 = 1.23$ V, OER requires a remarkably high overpotential compared to HER. The adsorbate evolution mechanism (AEM) has conventionally been used to describe the various reactions in the previous studies [15-17]. The reaction pathway of alkaline OER includes the following steps (5)-(8):



In the AEM, the OER involves the intermediates of $M-OH^*$, $M-O^*$, and $M-OOH^*$. The minimum theoretical overpotential for the investigated catalysts based on AEM is predicted to be ~ 0.37 V resulting from a linear scaling relation between the adsorption energies of $*OH$ and $*OOH$ intermediates ($\Delta G_{M-OOH^*} = \Delta G_{M-OH^*} + 3.2$ eV) [18]. However, this scaling relation cannot explain some reported catalysts with lower overpotentials. Therefore, researchers have proposed an alternative mechanism known as the lattice oxygen oxidation mechanism (LOM), in which the oxygen sites serve as the redox center for reactions, (as depicted in **Figure 1.7(a,b)**). Specifically, the adsorbed OH^- undergoes deprotonation to form O_2^- , and electrons from the oxygen orbital of O_2^- are transferred to the external circuit, forming radical O^- species, eventually form $(O-O)2p$ bands. This alternative mechanism aims to address the limitations of the AEM. Nevertheless, whether the oxygen redox reaction is reversible or irreversible, the LOM mechanism indicates instability in the electrocatalyst due to changes in the catalyst surface and disruption of crystal structure. Therefore, the true advantages of LOM may not be realized [18].

The density functional theory (DFT) calculations allow the prediction of the trend of OER catalytic activity. The activity of RuO_2 is theoretically anticipated based on the binding energy of the chemical intermediate and the catalyst, and it is near the top of the volcano (**Figure 1.8**) [19].

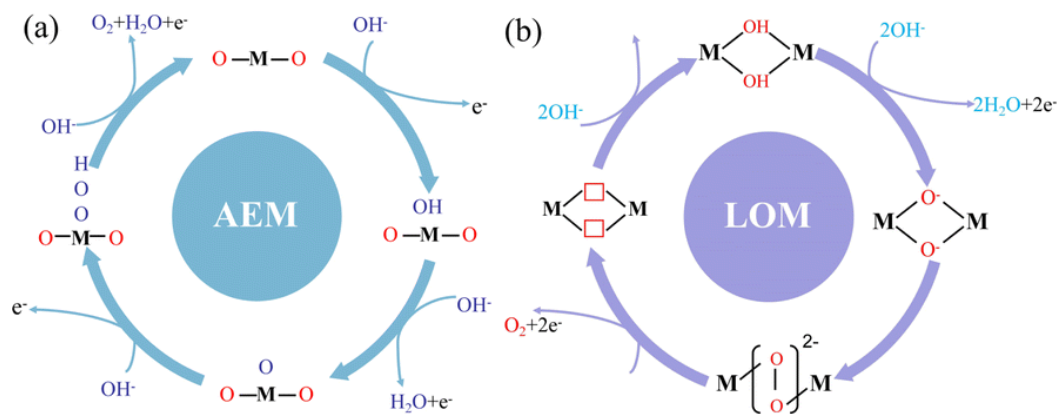


Figure 1.7: (a) AEM, and (LOM) mechanism (Source: reference [13])

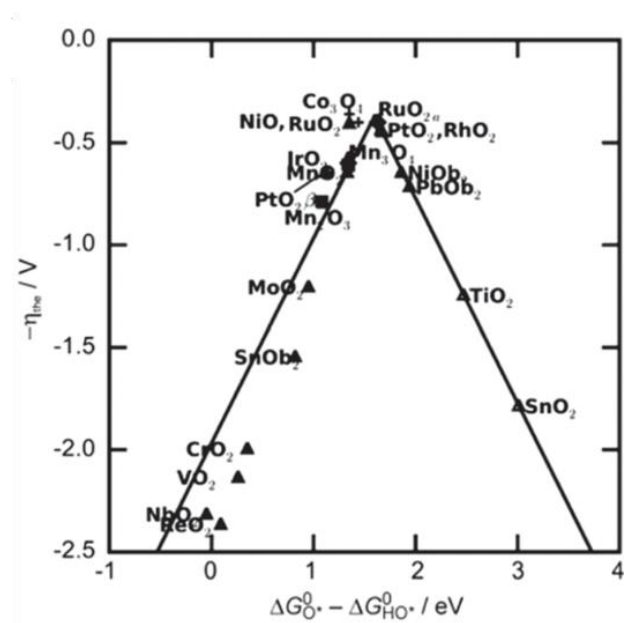


Figure 1.8: Volcano-shaped activity plot of the OER for oxides (Source: reference [19])

1.1.4. Electrocatalyst

1.1.4.1. Evaluation of an electrocatalyst

Overpotential (η)

The difference between the Nernst potential and the required potential to drive reactions at a certain rate defines the corresponding overpotential (η) (mV) of the catalyst, known as polarization or voltage loss. Specifically, for the HER, the Nernst potential is zero ($E_{\text{HER}} = 0 \text{ V}$) with respect to the reversible hydrogen electrode (RHE). In this case, the η is equal to the difference between the applied potential (E) and the Nernst potential (0 V), thus $\eta = E$. In contrast, for the OER, the Nernst potential is 1.23 V ($E_{\text{OER}} = 1.23 \text{ V}$) vs RHE, thus $\eta = E - 1.23$.

Usually, two specific overpotentials are often considered to compare the activities of different catalysts: η_1 , known as the onset potential, and η_{10} , which represents the overpotential required to achieve a current density of 10 mA/cm^2 . The η_1 marks the point at which the reaction begins to occur, while η_{10} is equivalent to corresponding to a 10% solar energy conversion efficiency [20], so the overpotential needed for this current density can provide a means for comparison.

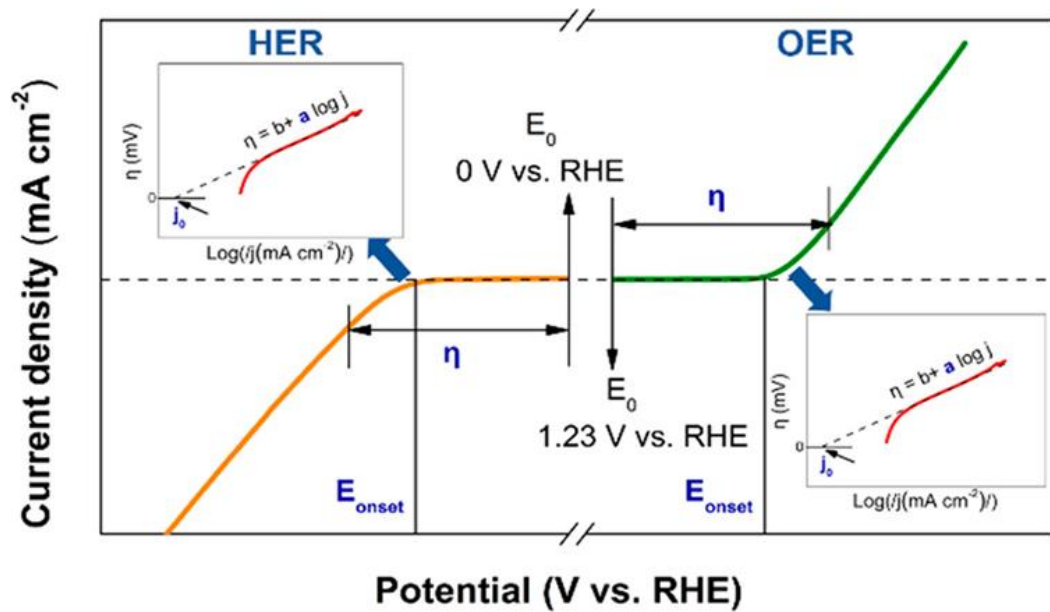


Figure 1.9: the polarization curves of OER (right) /HER (left). Inset is the Tafel plot obtained from the corresponding polarization curve (Source: reference [21])

Tafel slope (b)

This is a parameter to evaluate the intrinsic activity of an electrocatalyst and understand reaction mechanisms. It is denoted by “b” (mV/dec) and describes how the reaction rate changes with changes in η . Tafel slope was determined as the slope of the linear fitting of the potential vs. RHE against $\log(j)$, utilizing the Tafel equation $\eta = b \times \log(j/j_0)$, where j and j_0 are the current density and exchange current density, respectively. The j_0 can be determined by the Tafel equation when η is equal to zero. A material characterized by low b and high j_0 exhibits a high electrocatalyst performance.

Electrochemical Impedance Spectroscopy (EIS)

As far as we know, applying a constant voltage V across a resistance R induces a constant current I according to Ohm’s law. In a similar way, application of a sinusoidally varying potential across an electrochemical cell induces an alternating current (AC) (as **Figure 1.10(a)**). The AC analogue of Ohm’s law is given by the following: $\bar{V} = \bar{I}Z$, where Z is impedance, \bar{V} , \bar{I} denote the time-dependent voltage and current, respectively. Z is a resistance that varies in a cyclical manner, and therefore, Z has the units of ohms (Ω) [22].

The symbol Z^* is the overall impedance. In fact, Z^* comprises two components, which are real (Z') and imaginary (Z''). $Z^* = Z' - j \times Z''$, where $j = \sqrt{-1}$

An electrochemical cell is constructed, and its impedance Z^* determined as a function of frequency. From these impedance values, the Z' and Z'' are computed and hence a Nyquist plot is drawn which is a plot of Z'' (as ‘y’) against Z' (as ‘x’), as shown in **Figure 1.10(b)**.

From the Nyquist plot, an equivalent circuit of electrochemical cell can be determined. **Figure 1.11** shows the convention of an equivalent circuit is determined by Nyquist plot [23]. This plot is constructed with R_u (electrolyte resistance) and RCW element (R_{ct} -interface charge-transfer resistance, C_{dl} -double layer capacitance, and Z_w -diffusion resistance) in a series. EIS is helpful for kinetic studies, a smaller R_{ct} value suggests a faster reaction rate, leading to a smaller overpotential.

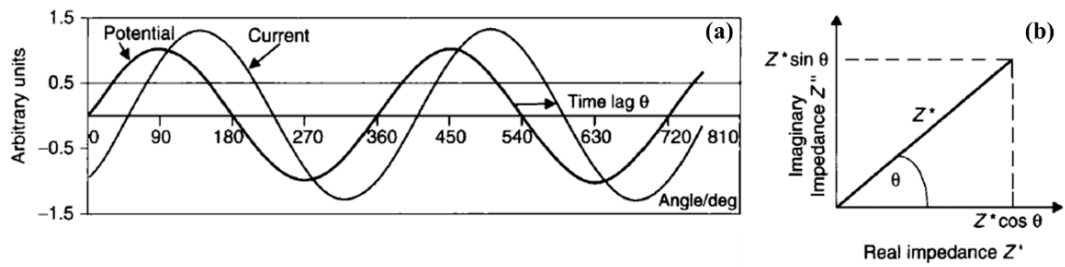


Figure 1.10: (a) a time-dependent potential creates an alternating current, and (b) Nyquist plot (Source: reference [22])

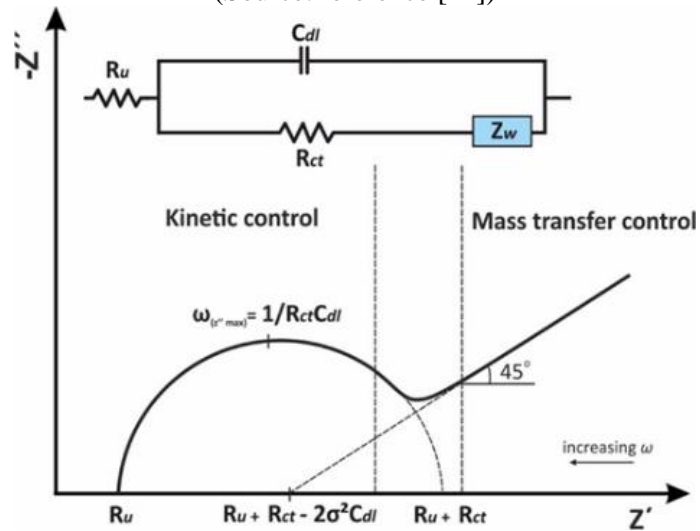


Figure 1.11: Randles equivalent electrical circuit over a wide frequency range (Source: reference [23])

Stability

Besides activity performance, stability is another crucial parameter for evaluating an electrocatalyst. One common method to assess stability is by conducting repeated cyclic voltammetry (e.g., over 5000 or 10000 cycles) within the range of the onset potential. A stable electrocatalyst typically exhibits minimal change in η over these cycles. Additionally, chronoamperometry (CA) and chronopotentiometry (CP) are other techniques used to evaluate the stability of electrocatalysts. In CA, a constant potential is applied to the electrochemical cell, with the resulting current measured over time at the working electrode. Conversely, in CP, the current is held constant while the potential of the working electrode is monitored.

Turnover Frequency (TOF)

TOF is the ratio of product formed per unit time and the amount of catalyst used [24]. While accurately calculating TOF remains challenging, researchers have found it to be a valuable means of comparing the intrinsic activity of electrocatalysts within similar systems. The formula for calculating TOF is as follows:

$$\text{TOF} = j / (x \times n \times F) \text{ (s}^{-1}\text{)}$$

Where j denotes the current density (mA/cm^2), x represents the number of active sites calculated using the electrochemically active surface area (ECSA) of the catalyst, n signifies the number of electrons transferred (with $n=2$ for HER, $n=4$ for OER), F is the faraday constant ($96,485 \text{ C/mol}$).

Faradaic Efficiency

Faradaic efficiency describes the efficiency with which charge (electrons) is transferred in a system facilitating an electrochemical reaction. Faradaic efficiency (%) is defined as the ratio of the experimental to theoretical amount of hydrogen in HER and oxygen in OER generation using the formular:

$$\text{Faradaic efficiency} = \frac{\text{experimental } \mu\text{mol of H}_2(\text{O}_2)\text{ gas}}{\text{theoretical } \mu\text{mol of H}_2(\text{O}_2)\text{ gas}} \times 100$$

The theoretical amount of $\text{H}_2(\text{O}_2)$ gas was calculated from Faraday's law:

$$n = \frac{I \times t}{z \times F}$$

Where n is the number of mol, I is the current (A), t is the time (s), z is the transfer of electrons (for HER $z = 2$, OER $z = 4$), and F is Faraday constant ($96,485 \text{ C/mol}$)

1.1.4.2. Fabrication of electrocatalysts

Hydrothermal/solvothermal

Hydrothermal and solvothermal synthesis methods are techniques used to fabricate electrocatalysts by employing high-temperature and high-pressure conditions in an aqueous or organic solvent environment, respectively.

Typically, a precursor containing metal salts or metal-containing compounds was dissolved in aqueous solution or organic solvent, then it is sealed in a reaction vessel and heated under autogenous pressure in an oven or autoclave at certain temperature. Commonly used metal salt precursors include nitrates, chlorides, and acetates, while organic solvents such as ethanol, ethylene glycol, isopropanol, PEG, tertiary butanol, and dimethylformamide (DMF) are often employed.

Hydrothermal/solvothermal synthesis method is widely used to prepare a variety of electrocatalysts including oxides, nanosized spinels, perovskites, etc. due to its good chemical homogeneity, high purity, and controlled nanostructure [25]. Sanka et al. successfully synthesized nanocomposite rGO-CoS₂ applying for HER by the one-step facile hydrothermal method [26]. By using DMF as organic solvent to prepare Fe₃O₄@Co₉S₈/rGO, Jing et al. revealed that DMF reduced partially Fe³⁺ to Fe²⁺, which induced the formation of pure phase Co₉S₈ and highly improves the catalytic activity for OER [27].

Precipitation

Precipitation method is a convenient method for preparing various electrocatalysts, including metal oxides, metal sulfides, and metal nanoparticles etc. This method does not require any complicated process, hard precipitation conditions, or any special instruments [25].

In precipitation process, electrocatalysts are formed through the precipitation of metal ions or compounds from a solution containing their precursor salts. This precipitation is induced by the addition of a precipitating agent or by altering the solution conditions, such as pH or temperature. Common precipitants include hydroxides (such as NaOH, KOH, NH₄OH), sodium carbonate (Na₂CO₃), sodium bicarbonate (NaHCO₃), ammonium carbonate ((NH₄)₂CO₃), ammonium bicarbonate (NH₄HCO₃), tetramethylammonium hydroxide, urea (CO(NH₂)₂) etc. He et al. used a co-precipitation method to prepare Mn-doped CuCo₂O₄ electrocatalyst. The

resulting $\text{CuMn}_{0.5}\text{Co}_2\text{O}_4$ catalyst had a high OER performance, with a low overpotential of 340 mV at a current density of 10 mA/cm^2 and a smaller Tafel slope of 69.8 mV/dec [28]. Cui et al. synthesized core-ring NiCo_2O_4 nanoplatelets using the coprecipitation decomposition method with sodium hydroxide as the precipitant, resulting in the highest electrocatalytic properties for OER in alkaline water electrolysis [29].

1.1.4.3. Material classification

Both HER and OER need an electrocatalyst to lower the activation energy required for the reactions, reducing the overpotential, thereby improving the efficiency hydrogen production. These electrocatalysts can be based on various materials.

Noble metal-based electrocatalyst

These materials include the platinum group metals (PGMs), which include Pt, Pd, Ru, Rh, Ir, and Os, and their derivatives. As illustrated in **Figures 1.8** and **1.6(b)**, the ΔG values of Pt and RuO_2 are located near the peak the volcano curve, leading to Pt and RuO_2 as benchmark materials for HER and OER, respectively. These materials are usually utilized in various nanoparticle forms to maximize their surface area and their defect-rich surfaces. The surface properties are well known to strongly influence the overall catalytic performance of noble metal nanoparticles.

Regardless of high activity, noble metals face challenges due to their scarcity and high cost, rendering them economically unfeasible. Furthermore, noble metal-based electrocatalyst suffered from a severe stability issue. The Pt nanocrystals exhibit limited shape variations owing to high internal strain energies and susceptibility to oxidative etching. Additionally, the small nanocrystal are prone to sintering or aggregation during the catalytic reaction [30]. On the other hand, as a benchmark for OER, RuO_2 demonstrates extreme instability due to dissolution from excessive oxidation at high overpotential of above 1.4 V during the OER process [31]. Consequently, noble metal-based electrocatalysts are considered less promising for industrial applications, which typically require excellent activity, chemical and electrochemical stability, and cost-effectiveness.

Transition metal-based electrocatalyst

These materials encompass transition metal and their compound including transition metal oxides (TMOs), transition metal nitrides (TMNs), transition metal carbides (TMCs),

transition metal dichalcogenides (TMDs), transition metal phosphides (TMPs), and transition metal borides (TMBs). These materials have been drawing attention due to their low toxicity, earth abundance, cost-effective, and environmental friendliness, which make them a potential candidate electrode for energy conversion systems [32]. Particularly, the TMOs have diversity in morphology, and they are easy to synthesize, enabling their scalability, rendering them commonly utilized as electrocatalysts for water splitting.

Cobalt oxide includes two easily obtained cationic oxidation states: Co^{2+} and Co^{3+} , which are mainly divided into CoO , Co_2O_3 , and Co_3O_4 . Their high redox potential and thermal stability render cobalt oxide a promising candidate for electrocatalysis. However, cobalt oxide suffers from low conductivity. To address this limitation, particle size, morphology, crystallinity, and dispersion of these materials are regulated to optimize active site distribution and exposure. Han et al. studied different morphology of Co_3O_4 nanocrystals anchored on nitrogen-doped reduced graphene oxide (N-rGO) including nanocube (NC), nanotruncated octahedron (NTO), and nanopolyhedron (NP). The exposed lattices of different morphology on the N-rGO were different. Electrochemical results indicate that the unusual (112) plane enclosed Co_3O_4 NP on rGO with abundant Co^{3+} sites exhibit superior bifunctional activity for oxygen reduction and evolution reactions [33]. Li et al. demonstrated that driving urchin-like Co_3O_4 spheres onto conductive nickel foam enhanced electrocatalytic activity by providing more active sites, facilitating electrolyte transfer, reducing contact resistance, and accelerating charge transportation [34]. Defect engineering is another efficient approach to modify the electrochemical activity of cobalt oxide including heteroatom substitution, vacancy and interstitial atoms [35]. Du et al. proved that oxygen vacancies enriched Co_3O_4 nanoflowers with single layer porous structures displays superior water splitting performances, maintaining activity for at least 9 days without significant decay [36]. Combining oxygen vacancies and heteroatom doping in Co_3O_4 , Yan et al. found that oxygen vacancies significantly enhanced OER activity, while Co–C bond formation delivered ideal HER activity [35].

Nickel oxide (NiO) is characterized as a p-type semiconductor with a band gap width of 4 eV, presenting traits of low toxicity, environmental friendliness, abundance in nature, and cost-effectiveness. It has gained considerable attention due to its flexibility in tailoring the crystalline phases, i.e., cubic, monoclinic, rhombohedral, and hexagonal, and the chemical composition, i.e., NiO, Ni_2O , and Ni_2O_3 for multifunctional applications. In the past few years, numerous reports on enhancing the catalytic performance of nickel oxide by means of

morphology control and optimization of the chemical structures, along with external excitation using strain, magnetism, and an electric field, have been documented. Manjunath et al. investigated the 0D nanoparticles and 2D porous nanoplates of NiO for bifunctional water splitting applications. The 0D nanoparticles, offering a larger surface area and active sites, demonstrated overpotentials of 373 mV and 268 mV for OER and HER activities, respectively, outperforming the 2D porous NiO nanoplates [37]. Cation doping serves as another strategy to enhance the catalytic performance of nickel oxide. For example, Fominykh et al. reported that $\text{Fe}_{0.1}\text{Ni}_{0.9}\text{O}$ exhibited superior electrocatalytic water oxidation activity in basic media [38].

Among the transition metal oxides, Fe based oxide is considered as a valuable substitute for OER electrocatalysts because of its abundant resources and easy preparation. Similar to Ni, Co-based oxide, there are many approaches to boost the electrocatalyst activity of Fe-based oxide, by providing more active sites with large surface area, like incorporation of foreign elements or doping, defect engineering, designing hybrid materials. Samanta et al. reported the preparation of iron oxide (Fe_2O_3), Ni-doped iron oxide (Ni- Fe_2O_3), Co-doped iron oxide (Co- Fe_2O_3), and Mn-doped iron oxide (Mn- Fe_2O_3) nanostructures. Ni- Fe_2O_3 exhibits the highest catalytic activity and stability in an alkaline medium with the resultant doped structures offer an enhanced conductivity and better charge transfer behavior toward OER and thus boost the electrocatalysis [39]. By using the structure-direct agent and varying the temperature, Xu et al. synthesized the γ - Fe_2O_3 and α - Fe_2O_3 microspheres. The result showed that α - Fe_2O_3 yolk-shell microspheres with higher exposure of Fe active sites exhibit more excellent OER kinetics [40].

1.1.5. Motivation

As the world shifts towards renewable energy sources to mitigate climate change, hydrogen has emerged as a promising clean energy carrier. Water splitting is an efficient method to produce green hydrogen, providing a sustainable way to meet energy demands. Therefore, identifying a suitable electrocatalyst with high activity, cost-effectiveness, and abundant availability to enhance both the HER and OER in the water-splitting process is essential. Transition metal-based electrocatalysts have the potential to drive the efficient and scalable production of hydrogen via water splitting. By the unique properties of transition metals, these catalysts have the potential to be applied in hydrogen generation technologies. This thesis aims to provide the frontier of knowledge electrocatalysis, contributing to future developments in hydrogen production technologies.

1.1.6. Research objectives

This research investigated cost-effective and sustainable electrocatalysts for HER and OER, thereby decreasing the dependence on the precious metal-based electrocatalyst. Improving the transition metal-based electrocatalysts by:

- Modifying the physicochemical properties of transition metal-based electrocatalysts to create heterostructure catalyst materials with appropriate composition, morphology, and electronic structure to determine the most effective configuration for enhancing HER and OER performance.
- Investigating the stability and durability of the selected electrocatalysts under prolonged electrolysis conditions to evaluate their long-term viability for practical applications.
- Assessing the catalytic activity of various transition metal-based electrocatalysts for both the HER and OER in water splitting processes. Comparing them to benchmark catalysts such as noble metal-based catalysts, to evaluate their competitiveness and potential for practical implementation.

1.2. Outline of dissertation

The structure of this dissertation includes four parts as following:

Part I: Overview of dissertation

Chapter 1 provides an introduction to the dissertation, discussing energy demand, the role of hydrogen as an energy carrier, the importance of electrocatalysts in water splitting, and various approaches for their classification, fabrication, and evaluation. The chapter also outlines the motivation and objectives of the thesis.

Part II: Depositing the active component on the two-dimensional materials

Chapter 2 presents the investigation of improving HER activity and stability of bimetallic oxide (NiO/Co₃O₄) by depositing them on the supporting siloxene. The chapter highlights the multifunctional role of siloxene as a reducing agent, surfactant, and support for bimetallic oxides, along with proposing mechanisms to explain the material's performance.

Chapter 3 explores the modification of CoMoO₄ through the incorporation of sulfur and oxygen into the lattice structure, supported by 2D materials such as reduced graphene oxide

(rGO), graphitic carbon nitride (gC_3N_4), and siloxene (SiSh). The resulting CMSO@2D material is investigated for its potential in the OER.

Part III: Modulating the electronic structure

Chapter 4 investigates the influence of rare earth oxide (Er_2O_3) on transition metal oxides (NiO , Co_3O_4 , and Fe_2O_3) for OER applications. The chapter elucidates the role of Er_2O_3 in modifying the physicochemical properties of transition metal oxides to enhance their OER performance.

Part IV: Modifying atomic geometries by phosphate group

Chapter 5 studies the compounds containing phosphates exhibit various atomic geometries. Their flexible coordination can stabilize the active oxidation state of transition metals, facilitating favorable adsorption and oxidation of water molecules.

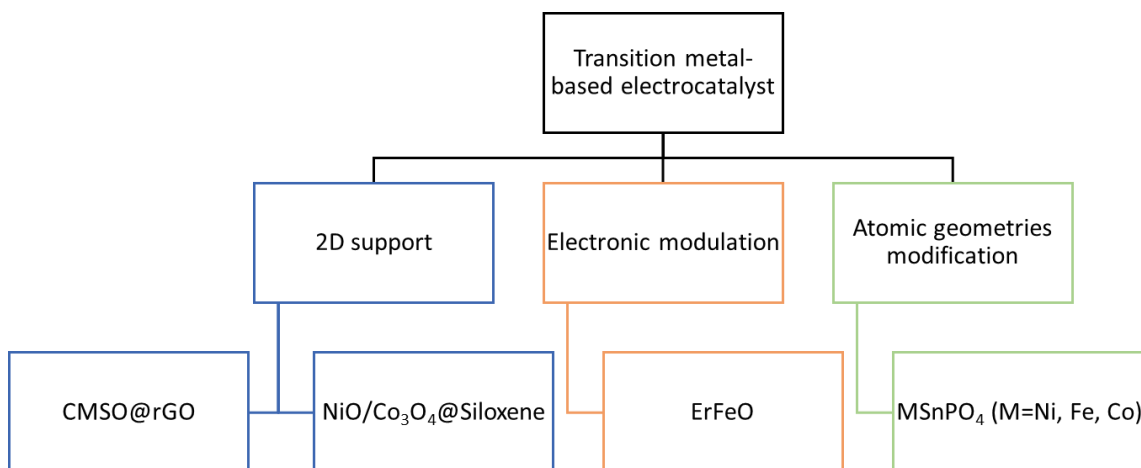


Figure 1.12: the structure of dissertation

Part 2. Depositing the active component on the 2D materials

Chapter 2. 2D Siloxene supported NiO/Co₃O₄ electrocatalyst for the stable and efficient hydrogen evolution reaction

2.1. Introduction

Water splitting is a sustainable method for generating hydrogen gas due to the abundance of water and the near-zero emission of byproducts during splitting [41, 42]. The process is associated with the cathodic hydrogen evolution reaction (HER) and anodic oxygen evolution reaction (OER). Thermodynamically, the dissociation of water is not favorable, and a catalyst is needed to lower the activation energy [43]. Previously, platinum or platinum-based materials have been used as the electrocatalyst for the HER [44]. On the other hand, their scarcity and high price limit their wide range of applications. Under this context, developing non-precious metal-based efficient and stable catalysts for facile water splitting has become an important research topic.

Hetero-structured materials, which are combinations of multi-components, have several heterojunctions acting as active sites [45]. A recent investigation reported the utilization of non-noble metal composites along with nonmetal carbon-based composite materials [46-49]. Among other transitional metals, Ni-Co chalcogenides (oxides, sulfides, and selenides) have emerged as efficient alternatives to traditional precious metal electrocatalysts with high activity and stability in alkaline medium [50-54]. In addition, Ni and Co are cheap and abundant. Moreover, their functionalities are easy to synthesize, and they have structural diversity, making them attractive as electrocatalysts. Abdul et al. studied a Co₃O₄/NiO composite that showed an overpotential of -0.65 V vs. RHE at 10 mA/cm² [52]. The hybrid Co₃O₄-NiO exhibited a good activity for bifunctional water splitting with an overpotential of 203 and 378 mV for the OER and HER, respectively, at 10 mA/cm² [51]. Wei et al. synthesized a carbon-incorporated NiO/Co₃O₄, which produced a low overpotential of 169.5 mV and 290 mV at 10 mA/cm² for the HER and OER, respectively [55]. Although the NiO/Co₃O₄ composite was investigated widely, their stabilities are sometimes unsatisfactory. Hence, researchers have attempted to support the bimetallic system with carbon and metal layers at different dimensions. In this regard, the 2D nonmetal support other than conventional graphene, carbon dot, and carbon nanotubes are yet to

be explored. On the other hand, it is difficult to control the content and states of the hetero-atoms carbon matrix during composite formation, and the connecting atom present in 2D carbon sometimes limits the overall catalyst activity [56, 57]. Here, 2D siloxene might act as an alternative support. Wöhler first synthesized siloxene in 1863. Zintl silicide, CaSi_2 was reacted with HCl, and the sandwiched Ca^{2+} ions between the silicon sheets were then deintercalated according to the following reaction [58]:



Weiss [59] and Kautsky [60] proposed two common structures of siloxene. The former siloxene structure has the silicon planar, while the latter has the incorporation of oxygen in the planar silicon. Siloxene is an exciting material because it has a high specific surface area, and its surface is functionalized with hydrogen and hydroxyl groups [61]. Furthermore, Si is the second most abundant element on Earth and is less expensive. Previously, siloxene was investigated for supercapacitor [62], photocatalyst [63], and Li-ion battery [64] applications. Regarding the electrocatalytic activity, Qi et al. examined a composite of iridium nanoparticles on a siloxene sheet that exhibited the great activity in the HER with an overpotential of 31 mV at 10 mA/cm² [65].

This study examined the role of siloxene as a support for NiO/Co₃O₄ composites. A hetero-structured NiO/Co₃O₄@Siloxene composite material was synthesized for the HER. Structural characterization revealed an ordered morphology and an increase in the electroactive surface area of the NiO/Co₃O₄ composite in the presence of siloxene. The presence of large numbers of active sites and the high velocity of electrons and mass transfer that facilitate the release of H₂ in an alkaline medium was assumed to contribute to its high efficiency towards the HER. NiO/Co₃O₄@Siloxene exhibited a low overpotential 110 mV at 10 mA/cm², Tafel slope of 102 mV/dec, and stability of more than 20 h in 1 M KOH.

2.2. Experimental details

2.2.1. Material

Calcium silicide (CaSi_2), Pt/C 20 % on carbon black, and Nafion 5 % were obtained from Sigma–Aldrich. Hydrochloric acid (HCl) 36.5 % was purchased from Alfa Aesar. Cobalt (II) nitrate hexahydrate ($\text{Co}(\text{NO}_3)_2 \cdot 6\text{H}_2\text{O}$), nickel (II) nitrate hexahydrate ($\text{Ni}(\text{NO}_3)_2 \cdot 6\text{H}_2\text{O}$),

isopropanol (C₃H₇OH), acetone ((CH₃)₂CO), and ethanol 99.9 % (C₂H₅OH) were supplied by Daejung Chemicals. De-ionized (DI) water was used for all syntheses.

2.2.2. Instrumental analysis

Raman measurements were carried out using a DXR Raman microscope (Thermo Scientific), the samples were put on the microscope glass and pretreated, then the spectra were collected from 100 to 1200 cm⁻¹ with a 532 nm monochromatic excitation source. The homogeneous mixture of 0.2 wt.% samples and KBr were pressed for making the pellets before doing Fourier transform infrared (FTIR) under the range of 4000-400 cm⁻¹ by using Thermo Scientific Nicolet 200 FTIR spectrometer (USA). A Rigaku X-ray diffractometer (D/MAZX 2500V/PC, Japan) with Cu K α radiation (0.154 nm) was used to measure the X-ray diffraction (XRD) pattern of all the powder samples with scan range 10-90 ° and scan rate was 2 degrees per minute. The powder form of material was taken in form of pallet to measure the X-ray photoelectron spectroscopy (XPS) in thermo ESCALAB 250 Xi, Thermo Fished Scientific of the USA, with Al K α X-ray radiation (1486.6 eV). The board range spectra were obtained to ensure the elements and the narrow range XPS spectra for each element over the permissible range was obtained to reduce the individual bonds. A field emission scanning electron microscopy (FESEM, JEOL JSM-6500 F, Japan) was employed to explore the morphology of samples which were coated with Pt. The samples were degassed for 24 h to remove the adsorbed species before doing nitrogen adsorption-desorption to determine the surface area of the samples by a Quantachrome Quadrasorb SI automated surface area and pore size analyzer.

2.2.3. Preparation of working electrode and electrochemical measurements

To prepare the working electrode (WE), 3 mg of sample was mixed with 0.5 mL propanol and 20 μ L of Nafion 5 %wt, followed by sonicating for 2h to form the homogenous slurry. The obtained slurry was coated on nickel form (1 cm x 1 cm) by

micropipette which was cleaned by HCl 1M, acetone and water. The WE was ready to use after drying at 60 °C for 2 h.

All electrochemical performances of catalysts were evaluated by using a three-electrode system (BioLogic, Science Instruments) taking the nickel foam coated with the as-prepared electrocatalyst, a graphite rod, and saturated calomel electrode (SCE) as the working, counter, and reference electrode, respectively. The electrolyte 1 M KOH was saturated N₂ to remove the dissolved O₂ before using. The catalytic performances by the materials were measured in terms of linear sweep voltammetry (LSV), cyclic voltammetry (CV) and electrochemical impedance spectroscopy (EIS). CV and LSV were performed within a potential range from -1.07 to -2.07 V vs SCE with the scan rate of 40 and 2 mV/s, respectively. The potential was converted to the potential versus the reversible hydrogen potential by the Nernst equation: $E_{RHE} = E_{SCE} + 0.059\text{pH} + 0.244$, where E_{SCE} is the potential versus SCE electrode, 0.244 is the standard potential of SCE versus standard hydrogen electrode at 25 °C, and pH is the pH value of electrolyte. The EIS tests were carried out within the frequency ranges 100 MHz to 1 Hz at an overpotential of 100 mV.

2.2.4. Synthesis of Siloxene

The procedure. 1 g of CaSi₂ was added slowly to 100 mL HCl 36.5 % in a round-bottomed flask. The mixture was stirred vigorously for 6 h at room temperature. The black color of CaSi₂ was turned gradually to yellow green color of siloxene. The solid product was collected by centrifugation and washed many times with acetone and DI water to remove the remaining HCl. Subsequently, the obtained sluggish was dispersed in 100 mL of C₂H₅OH and sonicated for 2 h. Finally, the siloxene was dried in a vacuum oven for 12 h at 60 °C.

2.2.5. Synthesis of NiO/Co₃O₄@Siloxene

0.08 g siloxene was dispersed and sonicated in 50 mL of DI water for 1 h. Subsequently, 0.04 g Ni(NO₃)₂·6H₂O and 0.04 g Co(NO₃)₂·6H₂O were added to the prepared siloxene (siloxene/Ni(NO₃)₂·6H₂O/Co(NO₃)₂·6H₂O in the weight ratio of 2:1:1), then stirred for 10 h at

room temperature. The solid product was collected by centrifuging and washing with DI water, followed by drying at 60 °C overnight. Next, the obtained powder was heated in air from room temperature to 500 °C with a heating rate of 10 °C/min and kept at this temperature for 3 h. NiO/Co₃O₄ was synthesized following the same procedure, in which urea/Ni(NO₃)₂·6H₂O/Co(NO₃)₂·6H₂O (the weight ratio of 2:1:1) was dissolved in 50 mL of DI water, then sonicated for 1 h. The material was then centrifuged and dried at 60 °C overnight after being stirred for 10 h at room temperature. Finally, the solid sample was calcined with the same heating procedure of NiO/Co₃O₄@Siloxene. The final product was used for catalytic application.

2.3. Results and discussion

2.3.1. Characterization of Siloxene, NiO/Co₃O₄, and NiO/Co₃O₄@Siloxene

In this work, NiO/Co₃O₄ was synthesized using siloxene as a support and a structure-directing agent. The structure and electronic state of the as-synthesized materials were examined by Fourier transform infrared (FT-IR) spectroscopy, Raman spectroscopy, X-ray diffraction (XRD), X-ray photoelectron spectroscopy (XPS), and field emission scanning electron microscopy (FESEM). **Figure 2.1(a)** presents the FT-IR spectra of siloxene, NiO/Co₃O₄, and NiO/Co₃O₄@Siloxene. Siloxene showed the following peaks: –OH stretching (3300 cm⁻¹); –OH bending vibration along the Si–OH bond (1636 cm⁻¹); Si₂O≡Si–H stretching (2128 cm⁻¹) and O₃≡Si–H stretching (2251 cm⁻¹); Si–O–Si stretching (1059 cm⁻¹); Si–H₂ scissor mode (879 cm⁻¹); Si–Si in planar (445 cm⁻¹) [61, 66]. This indicates that oxidation and hydroxylation occurred during the topochemical reaction, and a Kautsky-type siloxene sheet was formed [61]. In the case of NiO/Co₃O₄, the FT-IR spectrum exhibited the peaks at 552 cm⁻¹ and 661 cm⁻¹, which corresponded to Co–O and Ni–O vibrations [67]. Although the NiO/Co₃O₄@Siloxene showed a similar FTIR spectrum to siloxene, the peaks at 3300 cm⁻¹, 1636 cm⁻¹, 2128 cm⁻¹, and 2251 cm⁻¹, which were the specific peaks for –OH, Si–OH and Si–H vibrations in siloxene, were not presented in the FT-IR spectrum of NiO/Co₃O₄@Siloxene. This suggests that the NiO/Co₃O₄ was deposited on the siloxene surface with the aid of Si–OH and Si–H functional groups. This was further confirmed by Raman spectroscopy (**Figure 2.1(b)**). The peaks at 639 cm⁻¹ and 729 cm⁻¹, corresponded to the Si–H vibrations of siloxene, which vanished in the Raman spectrum of NiO/Co₃O₄@Siloxene. In addition, there were new peaks at wavenumbers

smaller than 300 cm^{-1} and 700 cm^{-1} , which correspond to the vibration of the metal–ligand bond [68] and Si–O–Si bond [69]. On the other hand, the Raman spectrum of NiO/Co₃O₄ without siloxene support showed the peaks of Co₃O₄ at 161 cm^{-1} , 443 cm^{-1} , and 641 cm^{-1} [70] and NiO at 500 cm^{-1} and 1033 cm^{-1} [71]. The crystallinity of siloxene, NiO/Co₃O₄, and NiO/Co₃O₄@Siloxene was examined by XRD in **Figure 2.1(c)**. XRD pattern of siloxene showed broad peaks at 14° and 23° , which were assigned to the (001) and (100) planes of the 2D siloxene sheet, respectively [61]. The peaks at 28.47° , 37.56° , 47.45° , and 56.10° were assigned to the crystalline Si (111), (210), (220), and (331) planes, respectively [72]. In addition to the peaks characteristic of siloxene, the XRD pattern of NiO/Co₃O₄@Siloxene had a few more peaks at 37.24° , 43.27° , 62.92° , 75.55° , and 79.35° , corresponding to the (111), (200), (220), (311), and (222) planes of the cubic NiO crystal structure (JCPDS no. 47-1049) [73] and 36.98° , 45.17° , 59.96° , and 74.67° matched well with (311), (400), (511), and (620) planes of Co₃O₄ (JCPDS no. 42-1467) [74]. For NiO/Co₃O₄, the peaks for NiO (36.65° , 43.37° , 62.96° , and 76.57°) and Co₃O₄ (18.82° , 31.08° , 36.65° , 44.49° , 55.39° , 59.03° , 64.80° , and 76.57°) were matched to JCPDS no. 00-044-1159 and JCPDS no. 00-080-1534, respectively. The results demonstrated that siloxene had a substantial effect on the crystallization of NiO/Co₃O₄. Brunauer–Emmett–Teller (BET) analysis [75] in **Figure 2.1(d)** shows that NiO/Co₃O₄@Siloxene and siloxene had the same isotherm. The inflection point of completing N₂ uptake of the monolayer was observed, and the adsorption also increased at high pressure, which corresponded to the type IV isotherm and hysteresis loop H3, according to the IUPAC classification [76]. The higher surface area of NiO/Co₃O₄@Siloxene ($185.42\text{ m}^2/\text{g}$) compared to NiO/Co₃O₄ ($51.68\text{ m}^2/\text{g}$) suggested that siloxene enhanced the surface area of the oxide composite. The $188.60\text{ m}^2/\text{g}$ surface area of individual siloxene implied a good dispersion of oxide particles without any pore-blocking on the siloxene surface in the NiO/Co₃O₄@Siloxene system [77]. **Table 2.1** lists the pore volume and pore size of the prepared materials.

Table 2.1: The pore volume and pore size of prepared materials calculated by using non-local density functional theory method (NLDFT)

Material	Pore volume (cc/g)	Pore size (nm)
Siloxene	0.138	4
NiO/Co ₃ O ₄	0.087	2
NiO/Co ₃ O ₄ @Siloxene	0.132	2

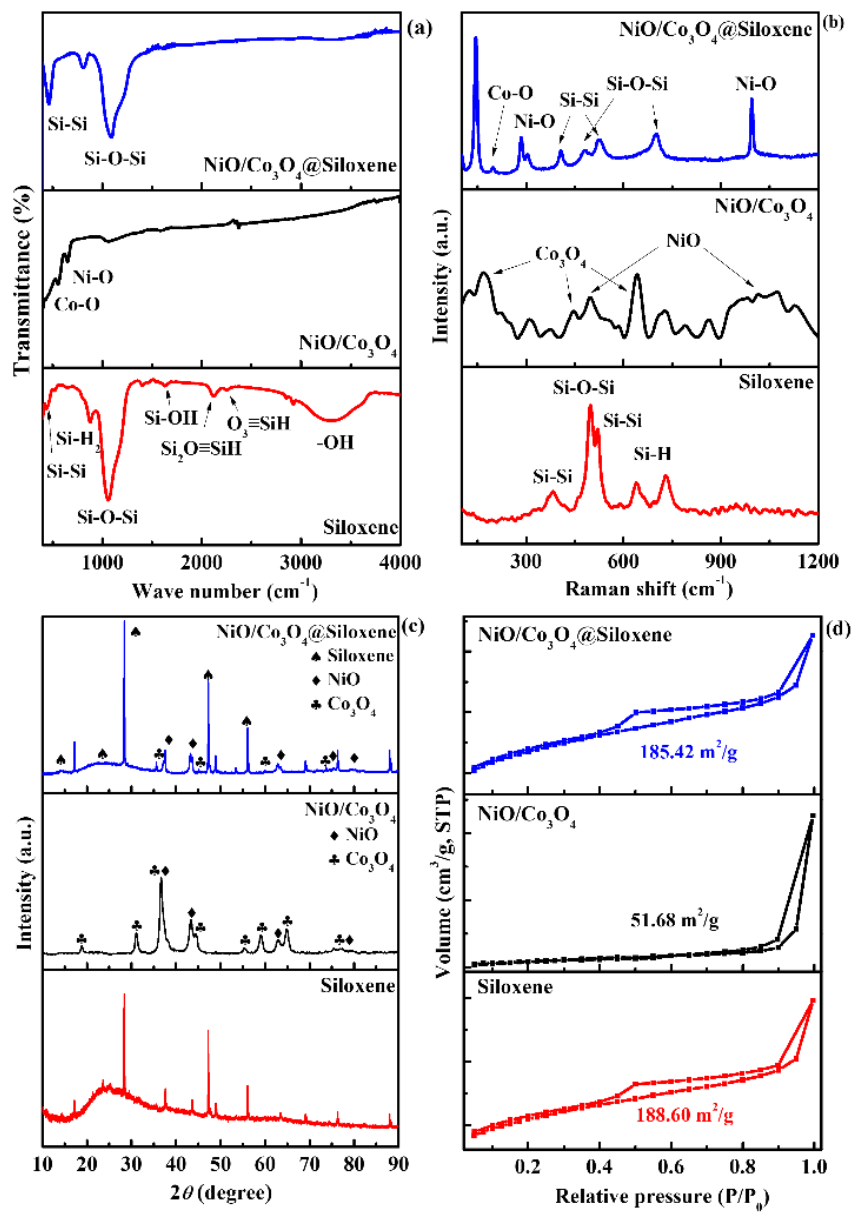


Figure 2.1: a) FT-IR spectra, (b) Raman spectra, (c) XRD pattern, and (d) N₂ adsorption–desorption isotherms of as-prepared samples

The morphology of the as-synthesized materials was examined by FESEM. The siloxene was crumbled and had a sheet-like structure (**Figure 2.2(a)**). In the case of NiO/Co₃O₄@Siloxene (**Figure 2.2(c)**), the flake-like structure of NiO/Co₃O₄ was deposited on the multi-sheet of siloxene. The heterostructure with multi-sheets helps prevent the active site of the catalyst from being confined within the limited interfaces, resulting in an improvement of the catalyst activity [78]. The HRTEM (**Figure 2.3**) of NiO/Co₃O₄@Siloxene reveals the incorporation of siloxene and NiO/Co₃O₄. The lattice fringes of 0.21 nm, 0.32 nm can be assigned to the NiO (200) [79], and Si (111) [80], respectively. According to XRD of NiO (JCPDS 47-1049) and Co₃O₄ (JCPDS 42-1467), NiO (111) and Co₃O₄ (311) have similar d-value [79, 81], making them difficult to distinguish from HRTEM. Thus, the lattice value of 0.25 nm can be assigned to the NiO (111) or Co₃O₄ (311) planes. Similarly, the d-value of 0.15 nm can be corresponded to NiO (220) or Co₃O₄ (511). On the other hand, when using urea as reducing agent instead of the as-synthesized siloxene, NiO/Co₃O₄ showed an aggregated flower-like structure (**Figure 2.2(b)**). Siloxene possessed a large number of functional groups on the surface which not only made the reductivity of siloxene but serve as the anchoring site to control the nucleation and growth of metal oxide [65, 82]. Thus, the smaller size of metal oxides was formed without aggregation as in SEM results. Moreover, the growing of metal oxide without additional capping agents which may limit their chemical activities [83]. Consequently, NiO/Co₃O₄@Siloxene had more active size than NiO/Co₃O₄. Element mapping showed that Co and Ni were distributed homogeneously over Si–O sheet in the NiO/Co₃O₄@Siloxene composite (**Figure 2.2(d-g)**).

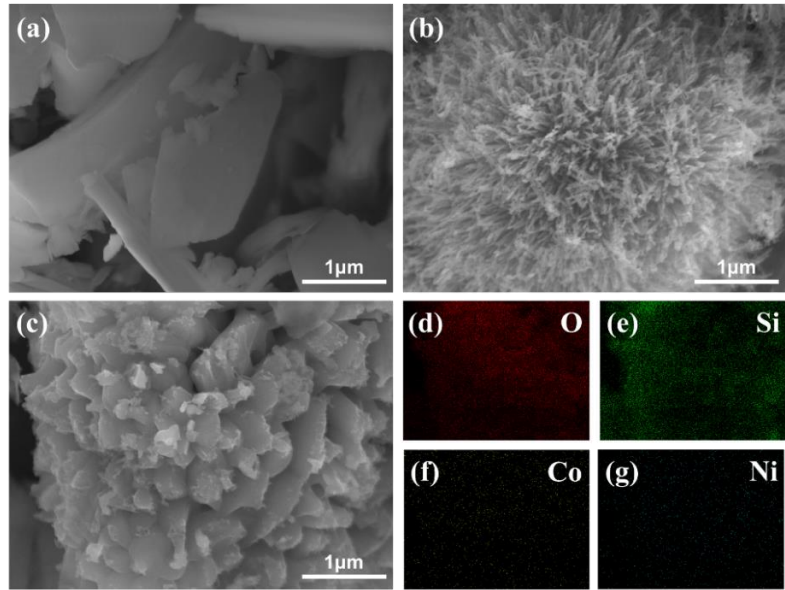


Figure 2.2: FESEM images of (a) Siloxene, (b) NiO/Co₃O₄, (c) NiO/Co₃O₄@Siloxene, and (d-g) element mapping of NiO/Co₃O₄@Siloxene

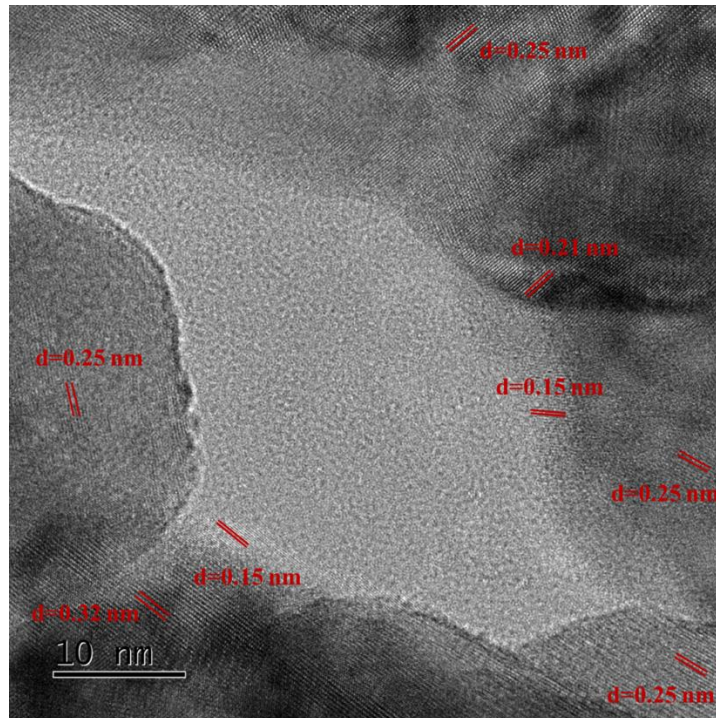


Figure 2.3: HRTEM lattice-fringe image of NiO/Co₃O₄@Siloxene

The oxidation states of the elements present in the composite were analyzed by XPS (**Figure 2.4**). As observed in **Figure 2.4(a)**, Si 2p in siloxene was composed of three peaks. The peak at 99.29 eV was assigned to the Si⁰ in the siloxene sheet, the dominant peak at 102.04 eV was from silicon suboxide SiO_x, and the last peak at 103.50 eV was characteristic of silicon dioxide (Si⁴⁺) [64]. The deconvolution of the O 1s peak of siloxene in **Figure 2.4(b)** shows two peaks at 531.12 and 532.46 eV, corresponding to the oxygen core level in SiO_x and silicon dioxide, respectively [84]. A decrease in the peak intensity of Si⁰ at 99.29 eV was observed, and a new peak appeared at 529.11 eV, corresponding to metal oxide in O 1s [85] in XPS of NiO/Co₃O₄@Siloxene. In particular, the peak for Si 2p and O 1s of NiO/Co₃O₄@Siloxene shifted to a lower binding energy (**Figure 2.5(a, b)**), which was attributed to the replacement of H in Si–OH and Si–H by metals that were less electronegative than H, increasing the outer electron density of O and Si, and resulting in a decrease in the binding energy of Si 2p and O 1s in NiO/Co₃O₄@Siloxene [86]. The broad range XPS spectra of NiO/Co₃O₄@Siloxene (**Figure 2.6**) revealed the presence of Ni 2p and Co 2p. The intensity of Ni 2p and Co 2p were weak owing to their low contents in the composite (**Table 2.2**). The deconvoluted spectra of Ni 2p (**Figure 2.4(c)**) exhibited two dominant peaks at 853.4 and 870.8 eV, corresponding to Ni 2p_{3/2} and Ni 2p_{1/2}, respectively [87]. **Figure 2.4(d)** shows two main peaks at 779.2 and 794.6 eV corresponding to Co 2p_{3/2} and Co 2p_{1/2}, respectively [88, 89]. On the other hand, for NiO/Co₃O₄, the dominant peaks of Ni 2p_{3/2} and Ni 2p_{1/2} were observed at 855.1 eV (the satellite peak of 860.7 eV) [90] and 872.6 eV (the satellite peak of 879.1 eV) [91], and the peaks of Co 2p_{3/2} and Co2p_{1/2} appeared at 779.4 eV and 795.0 eV, respectively [92, 93]. These results suggest that the interaction between NiO/Co₃O₄ and siloxene caused the inconsistency in the binding energy of Ni 2p and Co 2p in NiO/Co₃O₄ and that in NiO/Co₃O₄@Siloxene.

Table 2.2 ; composition of O, Si, Co, and Ni (At. %) elements present in NiO/Co₃O₄@Siloxene as recorded by XPS analysis

Element	At. %
O1s	60.40
Si2p	32.88
Co2p	0.64
Ni2p	1.19

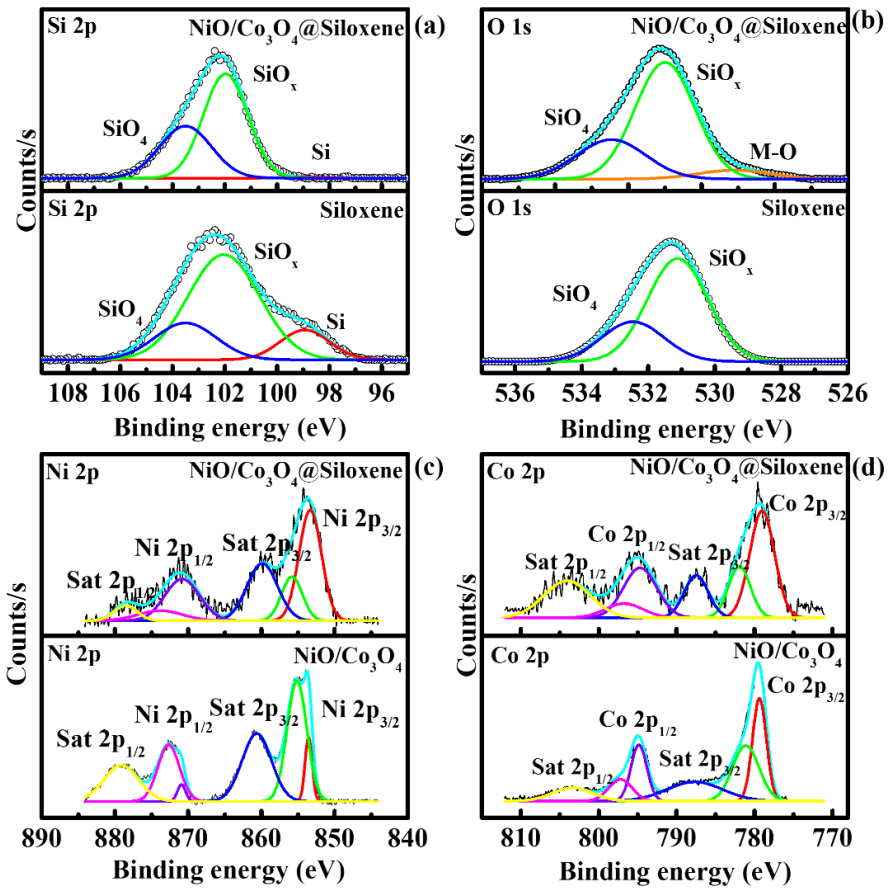


Figure 2.4: XPS spectra of (a) Si 2p, (b) O 1s, (c) Ni 2p, and (d) Co 2p of prepared materials

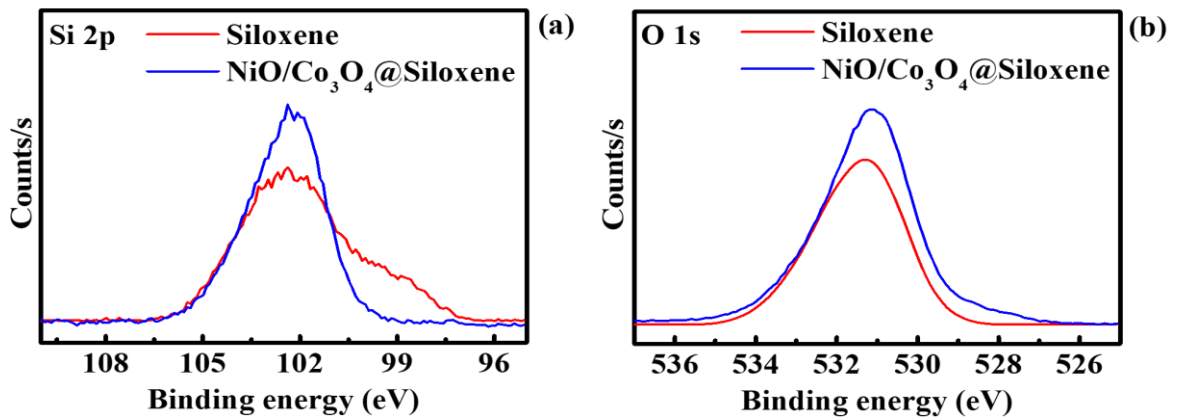


Figure 2.5: XPS spectra of (a) Si 2p, and (b) O 1s of NiO/Co₃O₄@Siloxene

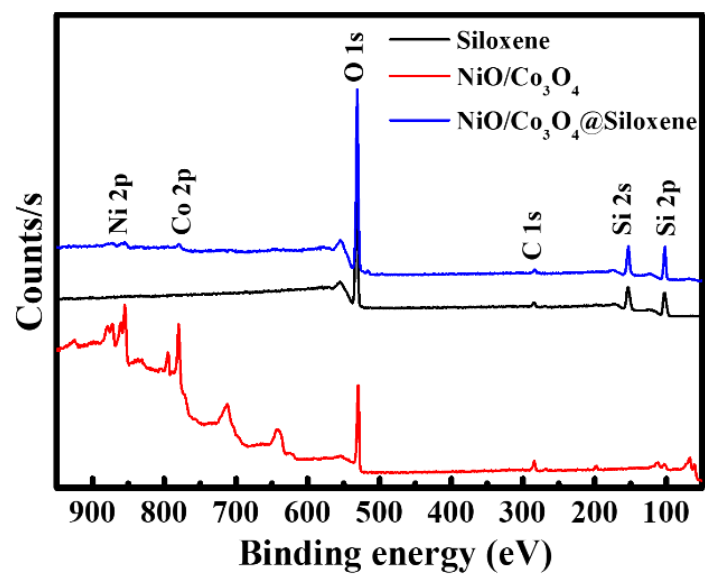
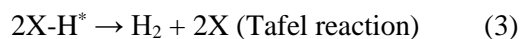
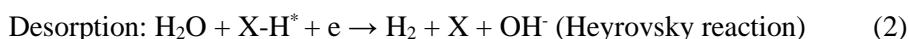
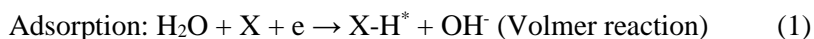


Figure 2.6: Broad range XPS spectra of prepared materials

2.3.2. Electrochemical activity of NiO/Co₃O₄@Siloxene towards hydrogen evolution reaction

The electrocatalytic activities of the as-synthesized materials were tested for the HER in an alkaline medium. For comparison, the activity of commercial Pt/C 20% was also measured under the same experimental conditions. **Figure 2.7(a)** shows the resulting polarization curves which was a plot of current density (per geometric surface area of 1 cm²) versus potential. NiO/Co₃O₄@Siloxene showed a lower overpotential to achieve higher current densities compared to other materials. The overpotential at the current density of 10 mA/cm² for NiO/Co₃O₄@Siloxene was 110 mV, which was lower than that of NiO/Co₃O₄ (247 mV) and siloxene (315 mV). As mentioned, the siloxene support had a profound effect on the size and morphology of the catalyst. The smaller size of NiO/Co₃O₄ on the siloxene with heterojunctions and the synergy of metal oxides enhanced the electrocatalyst performance. The kinetics of the electrochemical reaction can be understood further by the Tafel slope, which can be calculated from a linear fit of the potential against the logarithm of current density. The mechanism of the HER in an alkaline environment follows the reaction step [(1), (2), and (3)] as mentioned below, where X is the catalyst, and H* is adsorbed hydrogen atom [94]:



If the Tafel slope is ~120, ~40, and ~30 mV/dec, the rate-determining step (RDS) should be the Volmer reaction (1), Heyrovsky reaction (2), or Tafel reaction (3), respectively [95]. **Figure 2.7(b)** shows that the Tafel slopes of NiO/Co₃O₄@Siloxene, NiO/Co₃O₄, and siloxene were 102, 122, and 127 mV/dec, respectively. Hence, the adsorption of hydrogen would determine the rate of the overall reaction. NiO/Co₃O₄@Siloxene had the closest Tafel slope value to the benchmark material Pt/C 20 % (99 mV/dec), suggesting faster electron-transfer kinetics. The impedance studies provided additional information on the kinetic process on the electrode surface. As shown in **Figure 2.7(c)**, the Nyquist plot exhibited a semicircular

curve for siloxene, NiO/Co₃O₄, and NiO/Co₃O₄@Siloxene. An equivalent circuit was constructed with R_s (electrolyte resistance) and RC element (R_{CT}-interface charge-transfer resistance and C_{dl}-double layer capacitance) in a series. The R_{CT} value increased in the order of NiO/Co₃O₄@Siloxene (2.36 Ω) < NiO/Co₃O₄ (10.09 Ω) < siloxene (11.05 Ω), suggesting that NiO/Co₃O₄@Siloxene had the faster reaction rate, leading to a smaller overpotential. **Table 2.3** summarizes the results.

Table 2.3: Activities of the as-synthesized materials toward the HER

Material	Overpotential (η_{10}) (mV)	Tafel slope (b) (mV/dec)	Exchange current density (J_0) (mA/cm ²)	Interface charge-transfer resistance (R _{CT}) (Ω)
Siloxene	315	127	0.031	11.05
NiO/Co ₃ O ₄	245	122	0.113	10.09
NiO/Co ₃ O ₄ @Siloxene	110	102	0.995	2.36
Pt/C	3	99	10.438	0.40

These results were consistent with the electrochemically active surface area (ECSA). The ECSA of a catalyst can be estimated by cyclic voltammetry [20] according to the formula $ECSA = C_{dl}/C_s$, where, C_{dl} is the double layer capacitance and C_s is the specific capacitance. By plotting the difference in current density between the anode and cathode ($\Delta J/2$) at different scan rates, a straight line would be obtained whose slope would yield the C_{dl} value. As shown in **Figure 2.7(d)**, the C_{dl} of NiO/Co₃O₄@Siloxene was 21.02 μF/cm², which was higher than that of NiO/Co₃O₄ (2.43 μF/cm²) and siloxene (1.51 μF/cm²). It can be seen that the ECSA values did not comply with the BET surface area values and the experimental results suggest that the electrochemically active sites have a profound effect on the activities as shown in **Figure 2.8**. Furthermore, the 2D-siloxene facilitated charge and mass transfer and improved the dispersion of metal oxides, increasing the active site of catalyst, thereby enhancing the electrochemical performance of the catalyst. The high turnover frequency (TOF) value (**Figure 2.9**) of NiO/Co₃O₄@Siloxene also indicated efficient catalysis.

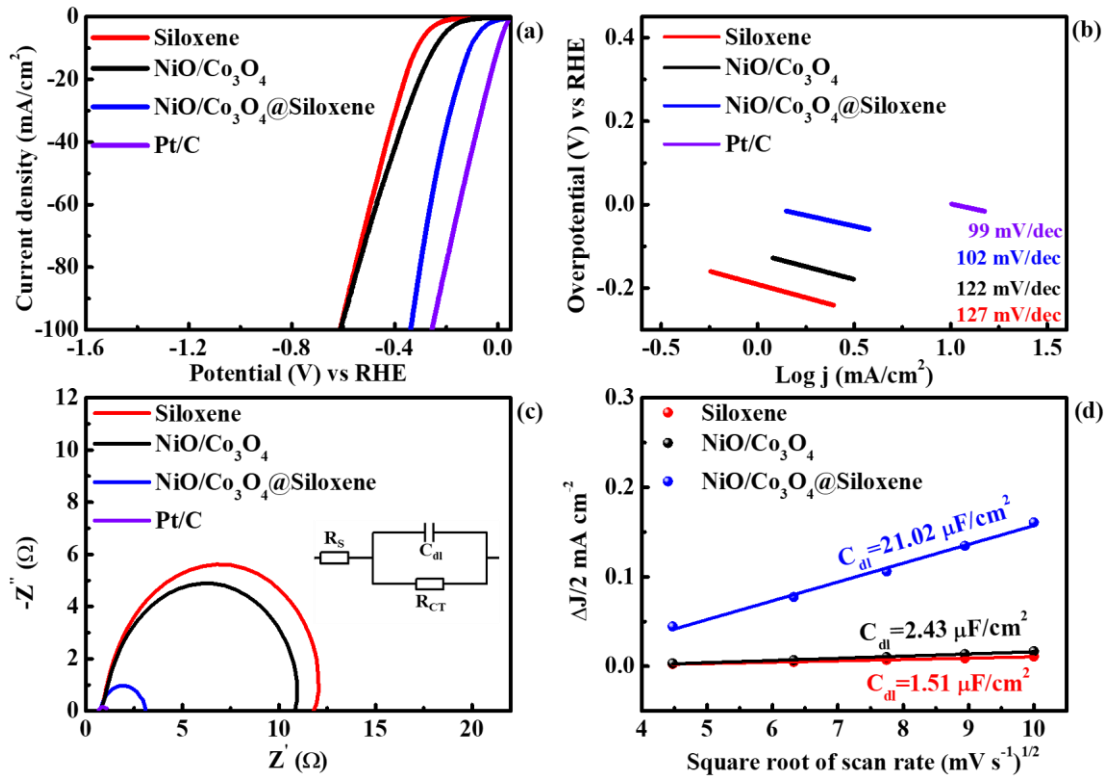


Figure 2.7: (a) LSV curves, (b) Tafel slopes, (c) Nyquist plots, and (d) Linear fit of the current density as a function of the scan rates

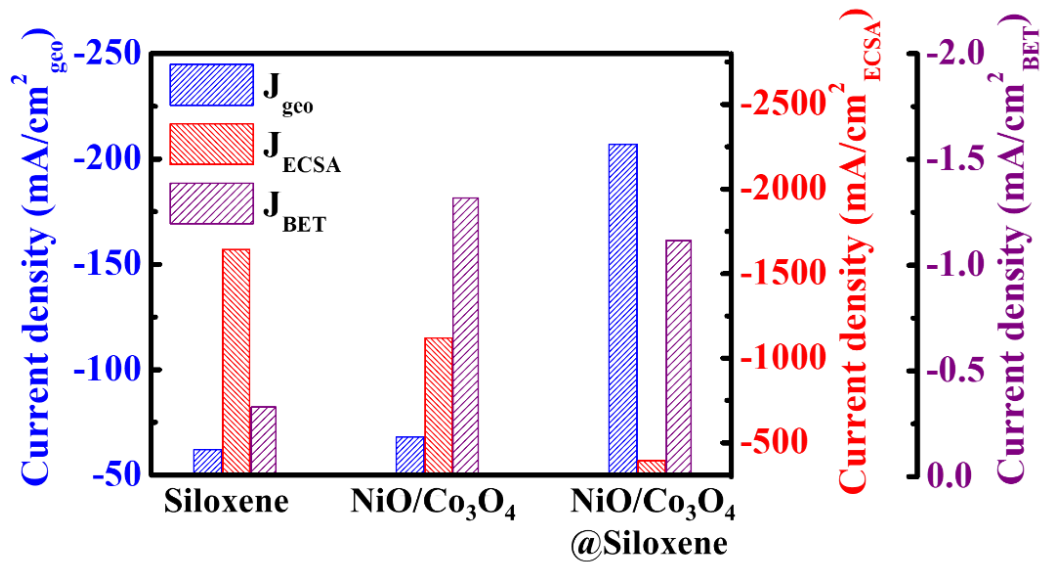


Figure 2.8: Corresponding J_{geo} , J_{ECSA} , and J_{BET} at -0.5 V vs. RHE of synthesized materials

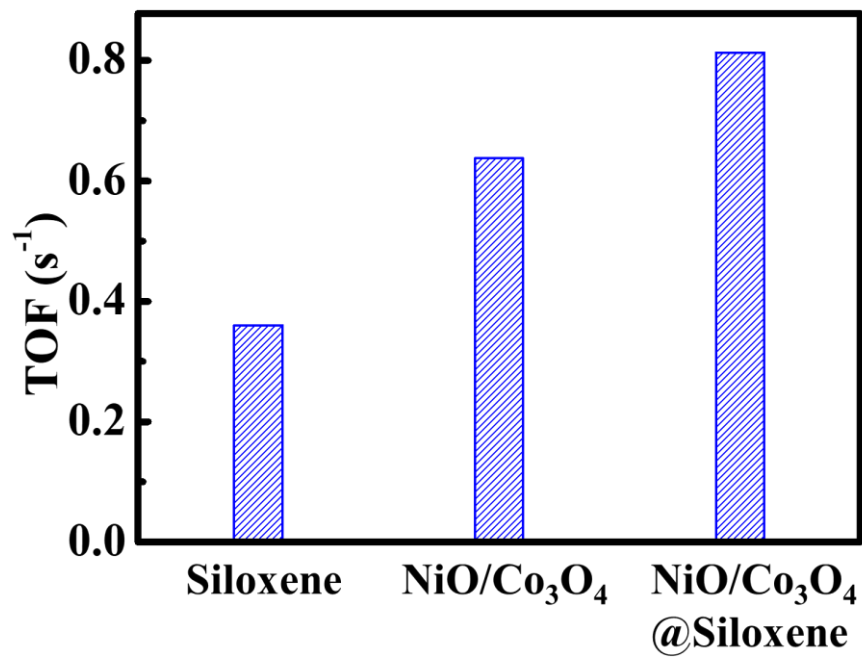


Figure 2.9: TOF values at the overpotential of -0.1 V, at scan rate 50 mV/s by using the methods reported previously [47]

It can be seen that neither siloxene nor NiO/Co₃O₄ showed good activity in HER, but the combination of NiO/Co₃O₄ with siloxene improved the activity toward to HER. Thus, the boosting HER performance of this composite can be attributed to the synergistic effect in NiO/Co₃O₄@Siloxene system. It was reported that for HER in the alkaline medium the reaction process involves adsorbing and reducing H₂O into OH⁻ and H⁺. Water dissociation is one of the sluggish steps of HER in the alkaline electrolyte [96]. Metal oxides are effective for the dissociation of water [97, 98]. Additionally, when NiO and Co₃O₄ were contacted closely as in HRTEM (**Figure 2.3**), the charge carrier at the interface will move until the Fermi level can be equal, then modify the charge accumulation on NiO and Co₃O₄, and may optimize the adsorption energy of reaction intermediates [51, 99, 100]. Besides, Zhu et al. proved that there was the migration of adsorbed hydrogen of active component to the Si support at their interface in the Si-based catalyst and owing to the weakly adsorbing surface of Si allowing faster hydrogen evolution [101], as was also observed by Sheng et al. [102]. Considering those phenomena, the mechanism can propose to explain the synergy of both metal oxides and siloxene as follow (i) reduction of H₂O at the active site Ni²⁺ and Co²⁺ to form adsorbed hydrogen; (ii) migration of the adsorbed H⁺ to siloxene surface; (iii) formation of hydrogen in gas phase.

Furthermore, the stability of NiO/Co₃O₄@Siloxene was monitored through the chronopotentiometry (CP) at a constant current density of 10 mA/cm² and was compared with that of NiO/Co₃O₄. **Figure 2.10(a)** presents the stability of NiO/Co₃O₄@Siloxene and NiO/Co₃O₄ after 20 h. There was a small increase in the potential of NiO/Co₃O₄@Siloxene ($V_0 = 110$ mV, $V_{20} = 141$ mV) over that of NiO/Co₃O₄ ($V_0 = 247$ mV, $V_{20} = 295$ mV) after 20 h, indicating that the presence of siloxene provided better stability to the NiO/Co₃O₄ composite (**Figure 2.10(b)**). The effects of long-term scanning were assessed by SEM, XRD, XPS and Raman. XRD (**Figure 2.10(c)**) indicated that the planes of NiO and Co₃O₄ in the composite were preserved. There were only slight changes in the peak intensity of NiO (at 43.27°, 62.92°, and 79.35°) and Co₃O₄ (at 59.36°). SEM (**Figure 2.10(d)**) showed that NiO/Co₃O₄@Siloxene retained its morphology even after the 20 h CP test. On the other hand, **Figure 2.11(a, b)** exhibited the XPS of Ni 2p and Co 2p after HER process. It was obvious that the peaks of Ni 2p and Co 2p after reaction were shifted to the higher binding energy. The peaks 855.0 eV, 872.7 eV of Ni 2p and 781.0 eV, 796.9 eV of Co 2p were characteristic of Ni(OH)₂ [103, 104] and Co(OH)₂ [105, 106]. This can be attributed to the interaction between Ni²⁺ and Co²⁺ and OH⁻ to

form these metal hydroxides during the reaction. This was consistent with Raman (**Figure 2.11(c)**) results in which was similar to that of the pre-stability test except for the decrease in peak intensity of NiO (at 280 cm^{-1} and 1000 cm^{-1} [107]) and Co_3O_4 (196 cm^{-1} [108]). **Table 2.4** compares the HER activity of NiO/ Co_3O_4 @Siloxene with other metal-oxide-based electrocatalysts to indicate the significance of the as-designed electrocatalyst. The results indicate that the NiO/ Co_3O_4 @Siloxene has significant activity towards the HER and can be used for further energy-related experiments.

Table 2.4: Comparison of HER activity in 1 M KOH of different electrocatalyst

Catalyst	Overpotential at 10 mA/cm ² (mV)	Tafel slope (mV/dec)	Reference
NiO	424	105	[109]
$\text{Co}_3\text{O}_4/\text{NiO}$	-0.65 vs RHE	61	[52]
$\text{Co}_3\text{O}_4\text{-NiO}$	378	90	[51]
$\text{Ni}_x\text{Co}_{3-x}\text{O}_4$	215	42	[110]
NiCo-NiCoO ₂ @Cu ₂ O@CF	133	119	[53]
Carbon-incorporated NiO/ Co_3O_4	165.9	119	[55]
NiO/MoS ₂	121	99	[111]
A-NiO NPs/rGO	201	100	[112]
$\text{Co}_3\text{O}_4\text{-NCTs}$	358	32.3	[113]
Fe-O-P/NF	166	-	[114]
Ni/Co-MOF@CoO/NF	139	96	[115]
MoS ₂ /Ni ₉ S ₈	122	-	[116]
NiO/ Co_3O_4 @Siloxene	110	102	This work

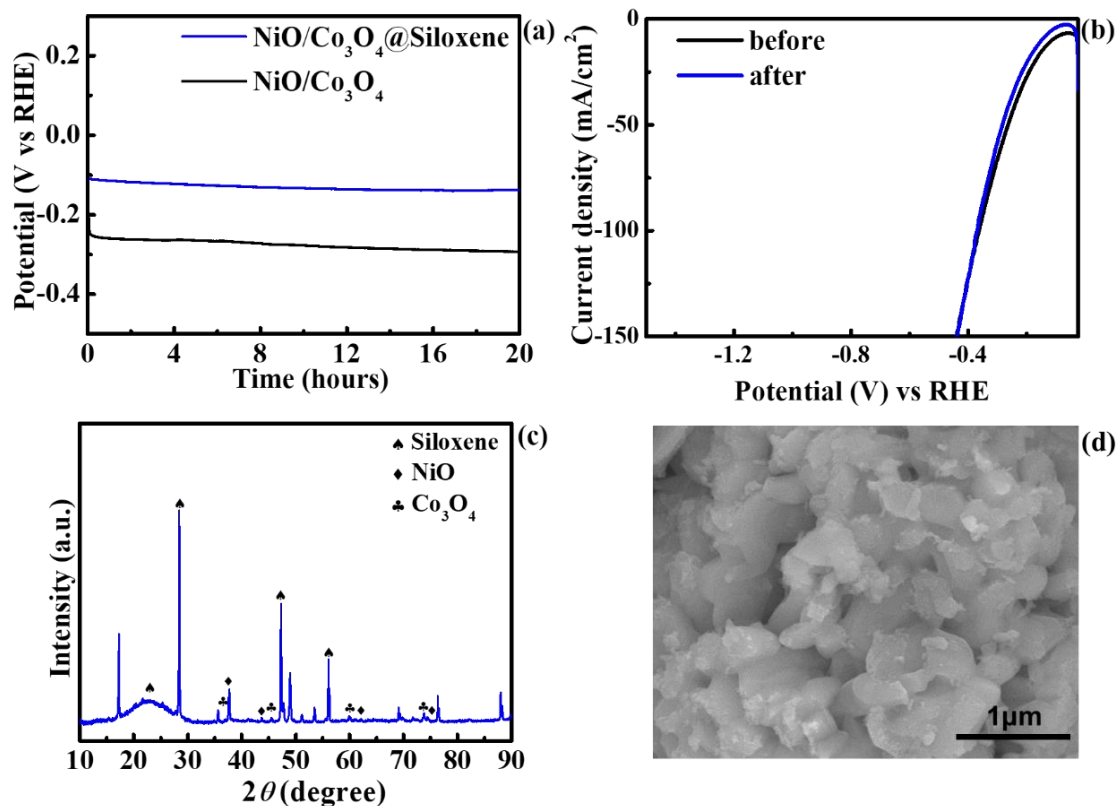


Figure 2.10: (a) Chronopotentiometry at 10 mA/cm², (b) LSV curve before and after the stability test (c) XRD pattern, and (d) FESEM image of NiO/Co₃O₄@Siloxene after stability test

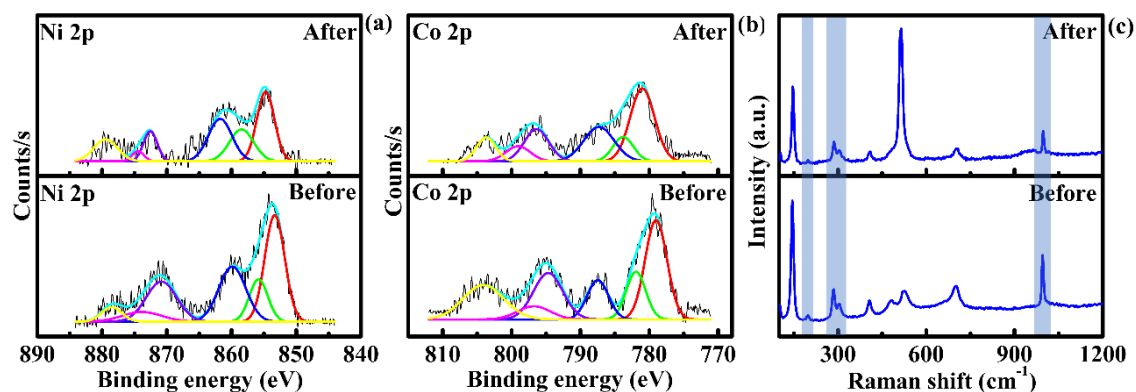


Figure 2.11: XPS spectra of (a) Ni 2p, (b) Co 2p, and (c) Raman spectra of NiO/Co₃O₄@Siloxene after stability test

2.4. Conclusion

A hetero-structured siloxene-supported transition metal oxide composite was synthesized by depositing NiO/Co₃O₄ on a 2D siloxene multi-sheet, and its catalytic activity was examined. The low overpotential of 110 mV at 10 mA/cm² and good stability for the HER of NiO/Co₃O₄@Siloxene was attributed to the 2D-siloxene facilitating charge and mass transfer and the synergy within metal oxides. Furthermore, the siloxene-directed smaller size of the metal oxides improved the surface area. The hierarchical structure, with multiple heterojunctions, allowed the maximal interaction with the electrolyte. Overall, NiO/Co₃O₄@Siloxene is a promising electrocatalyst for the HER in the future because of the simple synthesis procedure, low cost, and Earth earth-abundant material.

Chapter 3. Exploring the Effects of Various Two-Dimensional Supporting Materials on the Water Electrolysis of Co-Mo Sulfide /Oxide Heterostructure

3.1. Introduction

Hydrogen produced by electrolysis is one of the sustainable and promising energies to alter the energy from fossil fuels because of several factors, including the abundance of water as a feedstock, free of carbon dioxide emissions, and its wide range of applications [117]. However, the efficiency and utilization of water electrolysis are hindered by the low kinetics of the oxygen evolution reaction (OER) [118], which is the half-reaction of the water splitting reaction.

The heterostructure material, which is composed of two or more components, possesses the synergistic effect of all components to overcome the disadvantages of individual ones. Additionally, the contact of the crystal components might change the electronic structure and strain the material, rendering it appropriate for OER [45, 119, 120]. As a result, various transition metals have been integrated in heterogeneous manners [121-123] to replace the scarce and expensive benchmark precious metal-based electrocatalysts such as RuO_2 or IrO_2 in the OER process [124]. Among the transition metals, cobalt (Co) and molybdenum (Mo) are considered to be the most promising candidates because of their earth abundance and cost-effectiveness, as well as the excellent redox behavior of Co and high electrical conductivity of Mo [125-128].

Recently, several studies revealed that the introduction of a sulfur anion into Co is favorable for driving water oxidation. Wang et al. confirmed that the moderate replacement of oxygen with sulfur could modify the electronic structure of the composite to achieve optimal intrinsic OER activity [16]. Fei et al. reported that the co-substitution of Fe and S in CoMoO_4 increased the charge-transfer ability and decreased the energy barrier of the rate-determining step during OER [17]. Hu et al. confirmed that compared to a pure oxide surface, a lattice oxygen-sulfur co-existing shell surface of $(\text{NiCo})\text{O}_x\text{S}_{1.33-x}$ lowered the applied potential for surface reconstruction [129].

Employing a two-dimensional (2D) material as a supporting material for electrocatalysts can be an efficient strategy to increase the number of active sites and improve

long-term stability [130]. Reduced graphene oxide (rGO) has been widely used as a supporting material owing to its high specific surface area, high conductivity, and excellent mechanical strength [131]. As another carbon-based 2D material, graphitic carbon nitride (gC_3N_4) also can be used as a support because of its facile availability, simple production route, cost-effectiveness, and excellent chemical and thermal robustness [132, 133]. Additionally, as a hexagonal 2D material composed of six-membered rings of silicon separated from each other by Si–O–Si bridges, siloxene (SiSh) also exhibits excellent properties when used as a support [65, 134] owing to the high specific surface area and the presence of hydroxyl groups on the siloxene sheet [61].

Therefore, the heterogeneous structure of an oxide–sulfide composite of $CoMoO_4/CoS/MoS_2$ (CMSO) combined with the 2D material (CMSO@2D) is thought to be a good candidate of high-performance anode materials for the water splitting reaction. This study aimed to explore the potential of 2D materials, including rGO, gC_3N_4 , and SiSh, as supporting materials for CMSO to enhance the electrochemical activity and stability during the OER process. By conducting instrumental analysis and electrochemical characterization, rGO was found to be the best support for CMSO, and CMSO@rGO exhibited a low OER overpotential and a Tafel slope of 259 mV (10 mA/cm^2) and 85 mV/dec, respectively, which were comparable to those of RuO_2 . In addition, a clear current drop was not observed even after 40 h of continuous operation.

3.2. Experimental details

3.2.1. Material

Cobalt acetate ($Co(CH_3COO)_2 \cdot 4H_2O$), glycerol ($C_3H_8O_3$), isopropanol (C_3H_8O), ethanol (C_2H_6O), hydrazine monohydrate ($N_2H_4 \cdot H_2O$) were purchased from Daejung chemicals. Thioacetamide (TAA) (C_2H_5NS), Ammonium molybdate tetrahydrate ($(NH_4)_6Mo_7O_{24} \cdot 4H_2O$), melamine ($C_3H_6N_6$), Nafion 5%, ruthenium oxide (RuO_2), Pt/C 20%, and potassium hydroxide (KOH) were bought from Sigma-Aldrich. All of the chemicals were used without any purification after purchasing. Deionized water (DI) was used for all reactions.

3.2.2. Instrumental analysis

A DXR Raman microscope (Thermo Scientific) was employed to get the Raman spectra for all samples, the range collected from 100 to 1700 cm^{-1} with a 532 nm monochromatic excitation source. The X-ray diffraction (XRD) patterns were conducted by A Rigaku X-ray diffractometer (D/MAZX 2500V/PC, Japan) with Cu $K\alpha$ radiation (0.154 nm) and scan range of 10-90°. The X-ray photoelectron spectroscopy (XPS) was performed on thermo ESCALAB 250 Xi, Thermo Fisher Scientific of the USA, with Al $K\alpha$ X-ray radiation (1486.6 eV). The morphology of materials was observed by a field emission scanning electron microscopy (FESEM, Hitachi High-Tech Corporation, SU7000, Japan). The degas and nitrogen adsorption-desorption revealed the surface area and pore size of the samples, which was performed by a Quantachrome Quadrasorb SI automated surface area and pore size analyzer.

3.2.3. Preparation of working electrode and electrochemical measurements

All electrochemical experiments were performed in an alkaline medium (1 M KOH) using a three-electrode system (BioLogic, Science Instruments) at room temperature. The system included a reference electrode (RE), a counter electrode (CE), and a working electrode (WE). In there, RE was a Hg/HgO electrode, CE was a graphite rod, and carbon paper (CC) was WE which was washed with ethanol and DI before use. To prepare the WE, 3mg of catalyst was added in 490 μL of ethanol and 10 μL of Nafion 5%, then this mixture was sonicated for 30 minutes to get the homogeneous solution. Finally, 200 μL of prepared solution was dropped on CC (1x1 cm^2), the mass loading catalyst on CC was 1.2 mg/cm^2 . The RE was calibrated with respect to reversible hydrogen electrode (RHE) in the system of Pt as WE and 1 M KOH saturated hydrogen. The electrode potential of Hg/HgO was 0.92 V at current of 0 mA as shown in **Figure 3.1**. As a result, the formula to convert potential of RE (Hg/HgO) to RHE was given by $E_{\text{RHE}} = E_{\text{Hg/HgO}} + 0.92$ (V). The linear sweep voltammetry (LSV) was carried out at 5 mV/s in the potential range of 1-1.72 V versus RHE. The electrochemical impedance spectroscopy (EIS) was obtained over frequency range of 100 kHz to 0.1 Hz at 1.50 V vs RHE. The interface charge-transfer resistance (R_{ct}) is equal to the diameter of the semicircle in the Nyquist plot. The cyclic voltammetry (CV) was run at 20, 40, 60, 80, and 100 mV/s in the range of 1.07-1.17 V to acquire the electrochemical double layer capacitance (C_{dl}), which was the linear slope of the $\Delta j = (j_{\text{a}} - j_{\text{c}})/2$ at 1.12 V versus different scan rates. The electrochemical surface area (ECSA) of catalysts was determined by $\text{ECSA} = C_{\text{dl}}/C_{\text{s}}$, where specific capacitance C_{s} was 40 $\mu\text{F}/\text{cm}^2$ [20]. Chronoamperometric (CA) and Chronopotentiometry (CP) were conducted at 10 mA/cm^2 .

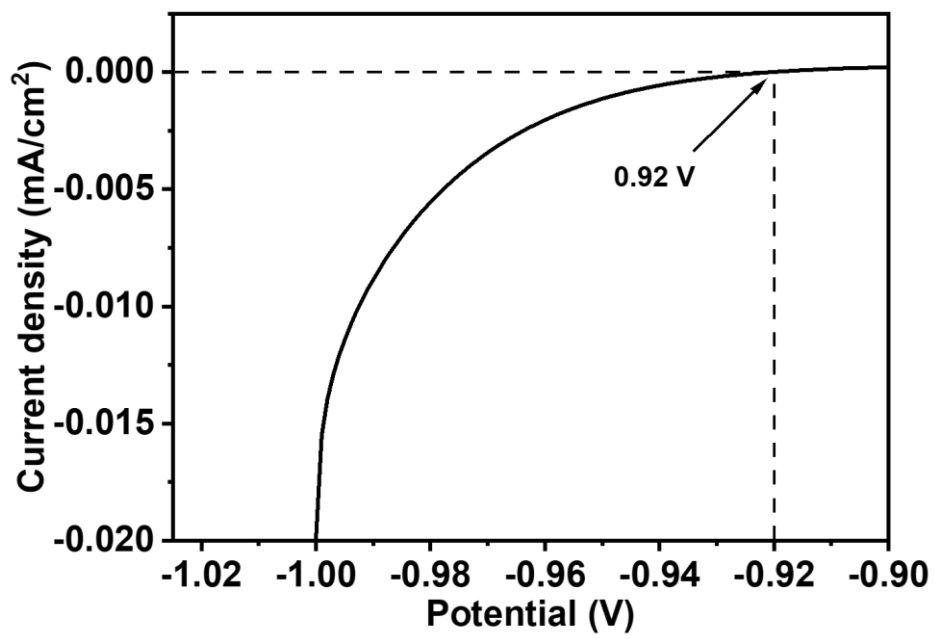


Figure 3.1: Calibration of Hg/HgO electrode

3.2.4. Synthesis of Co-glycerate precursor

Co-glycerate precursor: In a typical synthesis, 0.104 g of $\text{Co}(\text{CH}_3\text{COO})_2 \cdot 4\text{H}_2\text{O}$ and 8 ml of glycerol were dissolved into 40 mL of $\text{C}_3\text{H}_8\text{O}$ to form a transparent dark green solution. The solution was then transferred to a Teflon-lined stainless-steel autoclave and kept at 180 °C for 6 h. After cooling to room temperature naturally, the purple precipitate was separated by filtration, washed several times with ethanol, and dried in an oven at 70 °C

3.2.5. Synthesis of two-dimensional (2D) materials

Graphene oxide was prepared by the modified Hummer's method as reported previously [135] and subsequently reduced using hydrazine monohydrate ($\text{N}_2\text{H}_4 \cdot \text{H}_2\text{O}$) to obtain rGO nanosheets. SiSh was synthesized using the procedure described previously [134]. To prepare gC_3N_4 , 10 g of melamine was added into a porcelain crucible and heated at 600 °C for 4 h. Then, the resulting yellow powder was mixed with 100 mL of deionized (DI) water and subjected to sonication. The final product was obtained after centrifugation and subsequent drying overnight at 100 °C in air.

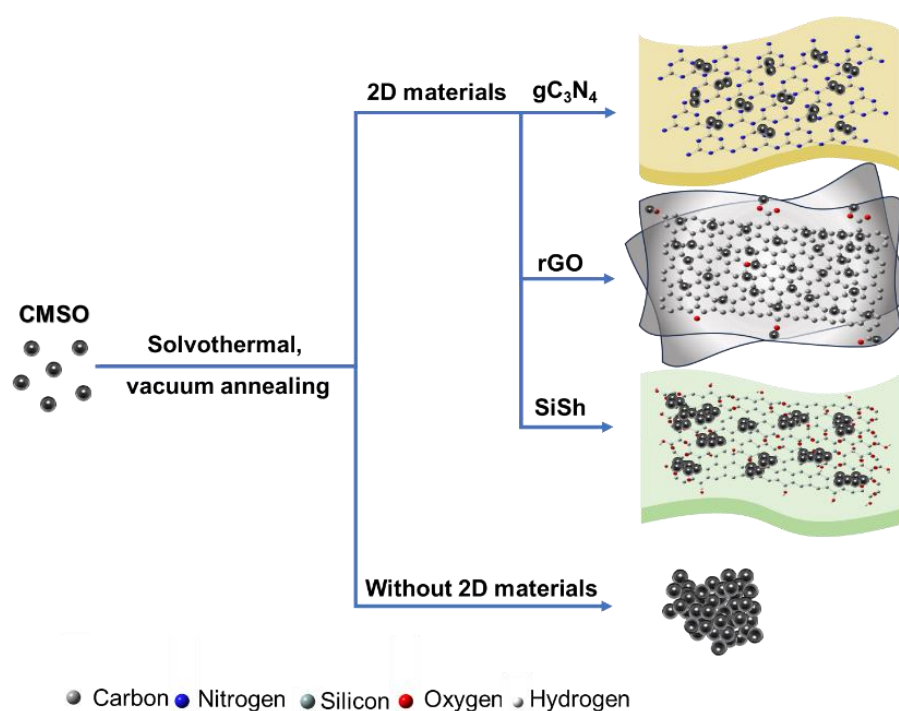
3.2.6. Synthesis of CMSO@2D

The CMSO@2D materials (viz. rGO, gC_3N_4 , and SiSh) were fabricated by a two-step method of solvothermal synthesis and vacuum annealing, respectively. In the solvothermal step, thioacetamide (TAA) was added as a sulfur source of CMSO. Co-glycerate and ammonium molybdate tetrahydrate ($(\text{NH}_4)_6\text{Mo}_7\text{O}_{24} \cdot 4\text{H}_2\text{O}$) were used as the precursors for Co^{2+} and Mo^{6+} , respectively, which reacted with TAA to form Co/Mo sulfide. The used 2D material served as a support and template for the anchoring sites of Co/Mo sulfide. During the vacuum annealing process, the materials were partially oxidized, resulting in the formation of $\text{CoMoO}_4/\text{CoS}/\text{MoS}_2@2\text{D}$ (CMSO@2D, **Scheme 3.1**).

Typically, mixture A was prepared by dissolving 20 mg of the Co-glycerate precursor, 10 mg of $(\text{NH}_4)_6\text{Mo}_7\text{O}_{24} \cdot 4\text{H}_2\text{O}$, and 50 mg of TAA in 20 mL of ethanol. Simultaneously, mixture B was formed by sonicating 20 mg of gC_3N_4 in 20 mL of ethanol. Then, mixture A was

slowly added to mixture B and stirred for 1 h. The resulting mixture was transferred into a Teflon-lined autoclave and heated, and the temperature was maintained at 200 °C for 6 h. After centrifugation and washing with ethanol and DI water, the product was dried in a vacuum oven at 60 °C for 12 h. Subsequently, the product was annealed at 500 °C under vacuum for 2 h. A similar procedure was followed for the reactions of the other 2D materials, with gC_3N_4 substituted by SiSh and rGO. In the case of rGO, 0.1 mL of $\text{N}_2\text{H}_4 \cdot \text{H}_2\text{O}$ was added to mixture B.

CMSO spheres were synthesized using a process similar to that of CMSO@2D except for the addition of the 2D materials.



Scheme 3.1: Schematic of CMSO and various CMSO@2D materials (2D materials: rGO, gC_3N_4 , and SiSh)

3.3. Results and discussion

3.3.1. Characterization of prepared materials

The crystal structure and phase composition of all materials were analyzed by XRD, as shown in **Figure 3.2(a)**. The XRD patterns of CMSO@rGO, CMSO@gC₃N₄, and CMSO@SiSh were similar to that of CMSO, indicating that a structural change did not occur during the deposition of CMSO on 2D materials and that all samples exhibited distinct MoS₂, CoMoO₄, and CoS phases. The diffraction peaks at 14.4° and 29.2° corresponded to the (002) and (004) planes of MoS₂, respectively (JCPDS No. 037-1492) [136]. The diffraction peaks at 26.5°, 36.5°, 42.4°, 53.5°, 61.5°, 73.7°, and 77.5° were characteristic of the (220), (400), (123), (333), (061), (622), and (350) planes of CoMoO₄ (JCPDS No. 04-017-6377), respectively [137]. The peaks observed at 34.4° and 47.1° were ascribed to the (101) and (102) planes of hexagonal CoS, respectively (JCPDS No. 65-3418) [138].

Additionally, in the XRD pattern of CMSO@SiSh, the characteristic peaks of SiSh were observed at 14.1°, 28.5°, and 56.1°, corresponding to the (001), (111), and (311) planes of siloxene, respectively. The peak located at 27.5° in the XRD pattern of CMSO@gC₃N₄ was attributed to gC₃N₄ (JCPDS No. 87-1526). Because the specific peak of rGO at 26.8° (JCPDS No. 89-8487) was overlapped with those of MoS₂ at 28.5° and CoMoO₄ at 26.5°, distinguishing the rGO-related peaks in the XRD pattern of CMSO@rGO was difficult. The Raman spectra of the prepared materials are shown in **Figure 3.2(b)**. In the Raman spectrum of CMSO, characteristic peaks for the bonding vibrations of Co–O–Mo at 808, 865, and 925 cm⁻¹; MoO₄ at 328 and 352 cm⁻¹ [139]; CoS at 511 and 676 cm⁻¹ [138], and MoS₂ at 280 cm⁻¹ were observed [140]. In the Raman spectrum of CMSO@rGO, two additional peaks were observed at 1351 cm⁻¹ and 1596 cm⁻¹. These peaks were assigned to the D band and G band of rGO, respectively. The integrated area ratio of the D and G bands of pristine rGO (**Figure 3.3(a)**) was 1.27, while that of CMSO@rGO increased to 1.46, indicating that after the anchoring of CMSO, the defect density of the rGO surface increased. In the Raman spectrum of CMSO@gC₃N₄, a broad peak was observed at approximately 1600 cm⁻¹, which was similar to that of bulk gC₃N₄ (**Figure 3.3(b)**). In the Raman spectrum of CMSO@SiSh, an intense peak at 513 cm⁻¹ corresponding to the Si–Si vibration of SiSh was observed, which was same as that of SiSh shown in **Figure 3.3(c)**.

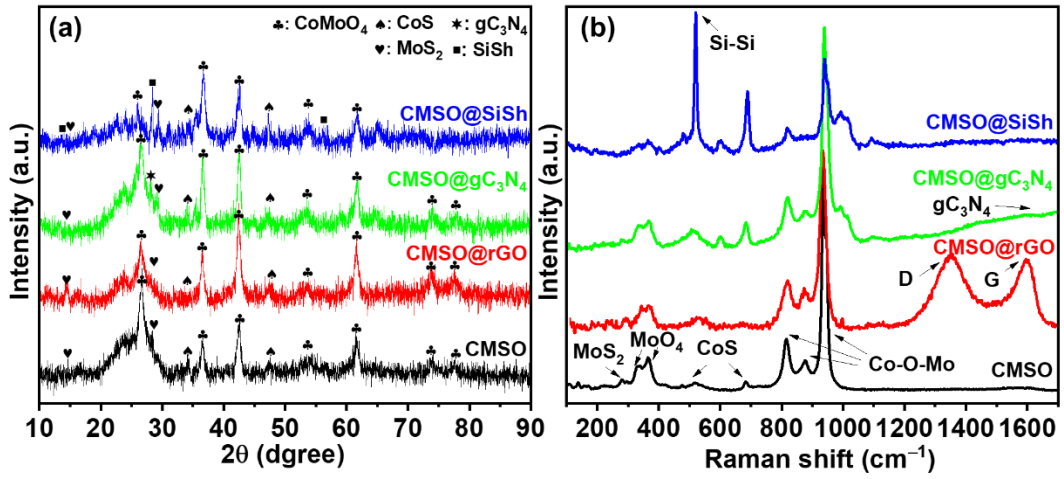


Figure 3.2: (a) XRD patterns and (b) Raman spectra of various materials

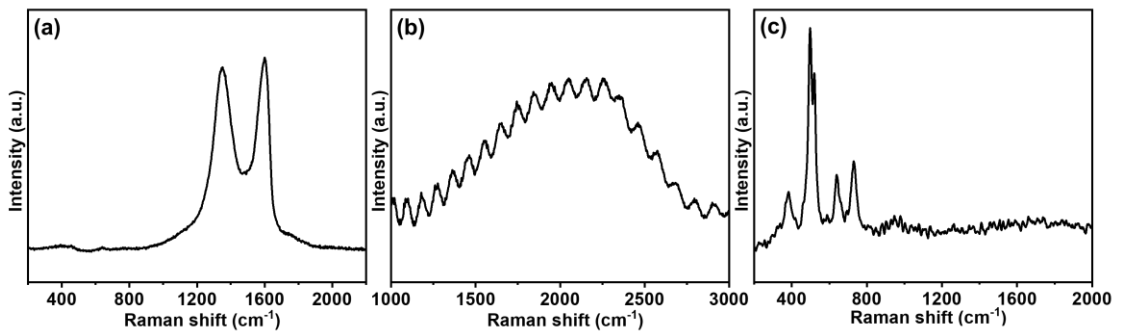


Figure 3.3: Raman spectrum of (a) rGO, (b) gC₃N₄, and (c) SiSh

Figure 3.4(a) shows the Brunauer–Emmett–Teller (BET) analysis of all materials. This result revealed that the material exhibited a type IV isotherm according to the IUPAC classification [75], indicative of the presence of a mesoporous structure with a pore size ranging from 2 to 50 nm. Notably, CMSO@rGO exhibited a significantly higher nitrogen adsorption amount, leading to the highest surface area among all of the materials. According to **Figure 3.4(b)** and **Table 3.1** the average pore radii of CMSO, CMSO@rGO, CMSO@gC₃N₄, and CMSO@SiSh were approximately distributed at 3.9, 1.6, 1.6, and 2.0 nm, respectively, which corresponding to the pore volume of 0.320, 1.154, 0.463, and 0.398 cm³/g. The specific surface area increased in the order of CMSO (116 m²/g) < CMSO@gC₃N₄ (156 m²/g) < CMSO@SiSh (201 m²/g) < CMSO@rGO (1392 m²/g), indicating that the modification of CMSO with 2D materials led to an increase in the specific surface area. Notably, the introduction of rGO substantially increased the specific surface area of the composite.

Table 3.1: Specific surface area, pore volume, and pore radius of various materials

Materials	Specific surface area (m ² /g)	Pore volume (cm ³ /g)	Pore radius (nm)
CMSO	116	0.320	3.9
CMSO@rGO	1392	1.154	1.6
CMSO@gC ₃ N ₄	156	0.463	1.6
CMSO@SiSh	201	0.398	2.0

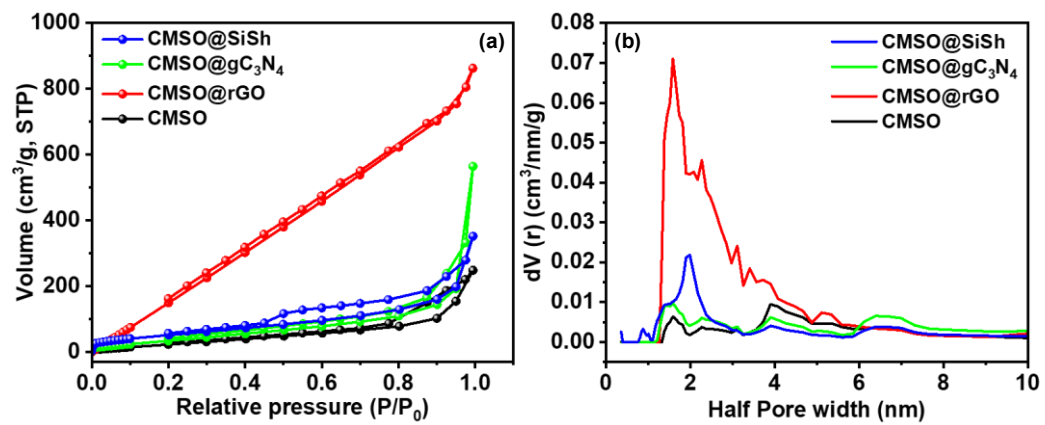


Figure 3.4: (a) N₂ adsorption–desorption isotherms of various materials, and (b) Pore size distribution by density functional theory method of various materials

To investigate the morphology of the as-prepared materials, field-emission scanning electron microscopy (FESEM) was conducted. The FESEM images are shown in **Figure 3.5**. CMSO exhibited highly agglomerated nanosphere particles, resulting in the formation of large clusters (**Figure 3.5(a)**). In contrast, when CMSO was supported on 2D materials, especially rGO (**Figure 3.5(b)**) and gC_3N_4 (**Figure 3.5(c)**), the interparticle voids were increased, which could provide additional pathways and spaces for the electrolytic ions to access the active sites. CMSO on SiSh (**Figure 3.5(d)**) exhibited a non-uniform morphology and a high degree of agglomeration, which could be attributed to a low number of functional groups that could anchor CMSO nanoparticles.

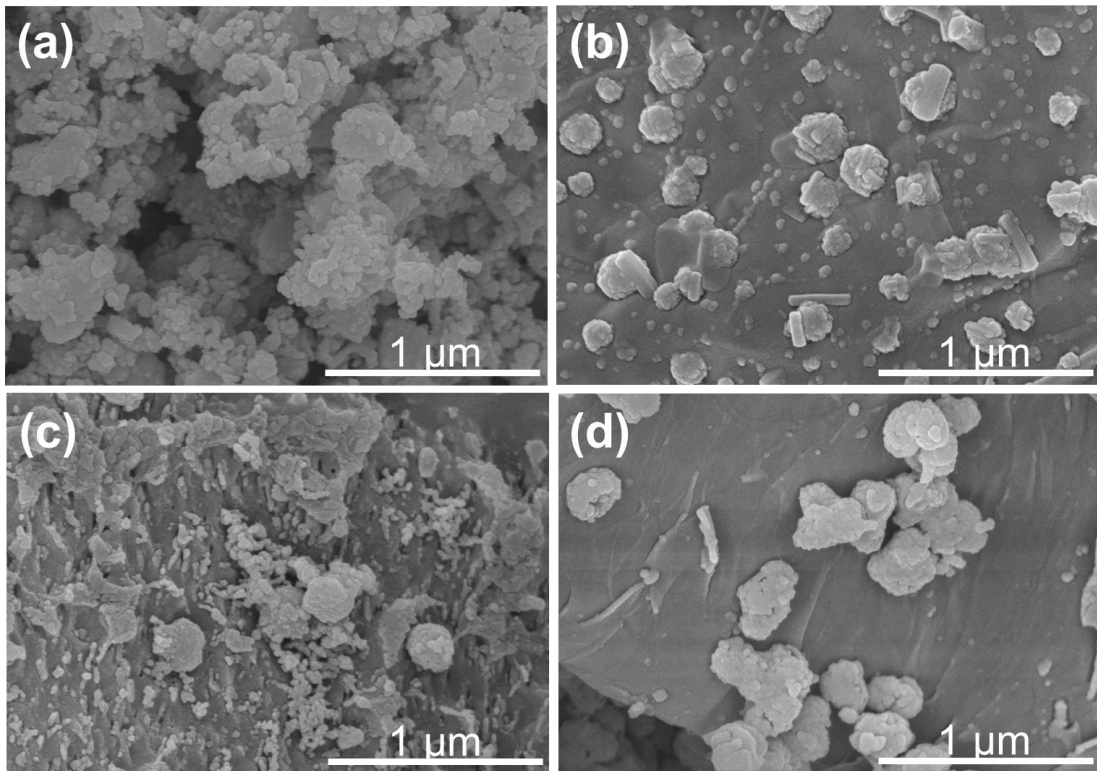


Figure 3.5: FESEM images of (a) CMSO, (b) CMSO@rGO, (c) CMSO@ gC_3N_4 , and (d) CMSO@SiSh

The elemental electronic states were investigated by X-ray photoelectron spectroscopy (XPS). In the deconvoluted Mo 3d spectra of CMSO (**Figure 3.6(a)**), dominant peaks observed at 235.4 and 232.3 eV corresponded to $3d_{3/2}$ and $3d_{5/2}$ of Mo^{6+} , respectively, and those at 234.7 and 231.2 eV corresponded to $3d_{3/2}$ and $3d_{5/2}$ of Mo^{4+} , respectively [141]. The weak peak located at approximately 228 eV associated with S 2s [142]. After the addition of 2D materials, these peaks were positively shifted relative to bare CMSO. In the deconvoluted Co 2p spectrum of CMSO (**Figure 3.6(b)**), two peaks located at 780.9 and 796.3 eV, accompanied by two satellite peaks indicated by asterisks, attributed to Co $2p_{3/2}$ and Co $2p_{1/2}$ of Co^{2+} , respectively [143]. An additional peak at 779.8 eV was attributed to Co–S bonding [138]. Interestingly, the position of Co 2p peaks in CMSO@rGO, CMSO@gC₃N₄, and CMSO@SiSh shifted to higher binding energies compared with that of pristine CMSO, indicative of the loss of electrons in Co [97]. The deconvoluted S 2p spectrum (**Figure 3.6(c)**) revealed four peaks. The peaks observed at 162.6 and 161.3 eV corresponded to S^{2-} of Co–S and Mo–S, respectively [144, 145]. Two additional peaks at 169 and 167.7 eV corresponded to oxidized sulfur [142]. The high-resolution O 1s XPS spectra (**Figure 3.6(d)**) showed a major peak at 530.2 eV, corresponding to O in CoMoO₄ [146]. After modification with 2D materials, the S 2p peaks exhibited a negative shift, and the O 1s peaks exhibited a positive shift, indicative of the electronic interaction between CMSO and 2D materials [97]. Such charge transfer between CMSO and supporting materials could induce adjustments in the energy-band alignment, which might thermodynamically facilitate the OER process [147].

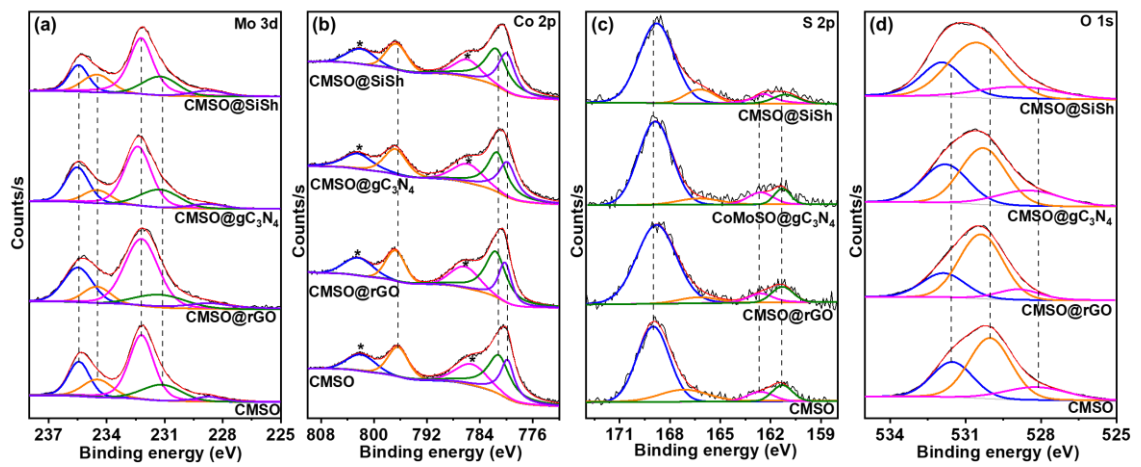


Figure 3.6: Deconvoluted high-resolution XPS spectra of (a) Mo 3d, (b) Co 2p, (c) S 2p, and (d) O 1s of various materials

3.3.2. Electrochemical activity of CMSO@2D towards oxygen evolution reaction

To evaluate the effect of 2D supporting materials on the activity of CMSO in the OER process, the electrocatalytic properties of CMSO, CMSO@rGO, CMSO@gC₃N₄, and CMSO@SiSh were investigated and compared with those of RuO₂, which was widely recognized as a benchmark material for OER. The OER overpotentials of 2D material-supported CMSO such as CMSO@rGO (259 mV 10 mA/cm²), CMSO@gC₃N₄ (270 mV), CMSO@SiSh (287 mV) were less than that of CMSO (384 mV), which indicated the improved OER properties of CMSO by the 2D supporting materials (**Figure 3.7(a, b)**). In addition, the overpotential of CMSO@rGO was less than that of RuO₂ (315 mV). To gain insights into the OER kinetics, the Tafel slope was calculated based on overpotential and the logarithm of current density data (**Figure 3.7(c)**). Same as the OER overpotential, the Tafel slopes of CMSO@rGO (85 mV/dec), CMSO@gC₃N₄ (109 mV/dec), and CMSO@SiSh (86 mV/dec) were lower than that of CMSO (141 mV/dec), which indicated the faster OER kinetics of 2D material-supported CMSO. Among the other material-supported CMSO, CMSO@rGO exhibited the lowest Tafel slope, which was less than that of RuO₂ (136 mV/dec).

The electrochemically active surface area (ECSA) and electrochemical impedance spectroscopy (EIS) were measured to obtain better understanding of the improved OER activity of CMSO rendered by the 2D supporting materials. The double layer capacitance (C_{dl}), which was directly proportional to the ECSA value, of each material was measured from the cyclic voltammetry curves shown in **Figure 3.8**. The C_{dl} of CMSO was 2.9 mF/cm², and it was increased to 11.0 mF/cm² (CMSO@SiSh), 16.2 mF/cm² (CMSO@gC₃N₄), and 35.2 mF/cm² (CMSO@rGO) (**Figure 3.7(d)**), which clearly indicated the effects of 2D materials on the C_{dl} value. The highest C_{dl} of CMSO@rGO could be strongly related to its highest BET surface area as shown in **Figure 3.9**.

The Nyquist plots obtained from the EIS of all materials exhibited a semicircle (**Figure 3.7(e)**). Notably, the charge transfer resistance (R_{ct}) of CMSO@rGO was measured to be 3.9 Ω , which was significantly lower than those obtained from other materials as summarized in **Table 3.2**. This result implied that CMSO@rGO exhibited a higher electron and charge transfer velocity than those of the other samples. The lower R_{ct} value of CMSO@rGO was consistent with its superior electrocatalytic activity, including lower overpotential, smaller Tafel slope, and higher ECSA. The electrochemical performances of the investigated materials are summarized in **Table 3.2**.

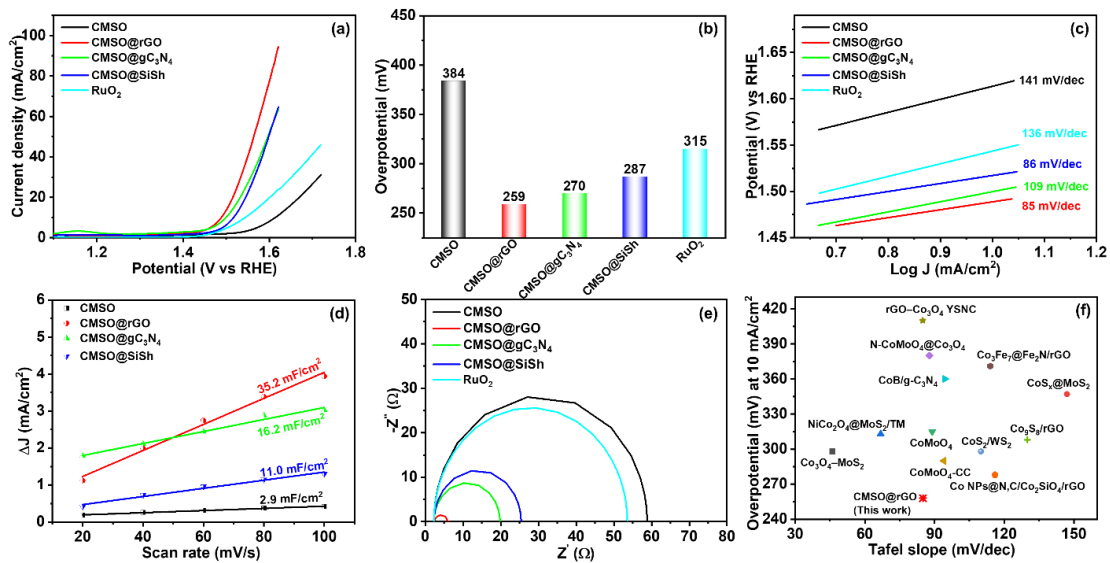


Figure 3.7: (a) LSV curves, (b) Comparison of the overpotential at 10 mA/cm², (c) Tafel slope, (d) Linear fitting of the current density against scan rates, (e) Nyquist plots of various materials. (f) Comparison of the overpotential and Tafel slope of CMSO@rGO with [148-159] in OER.

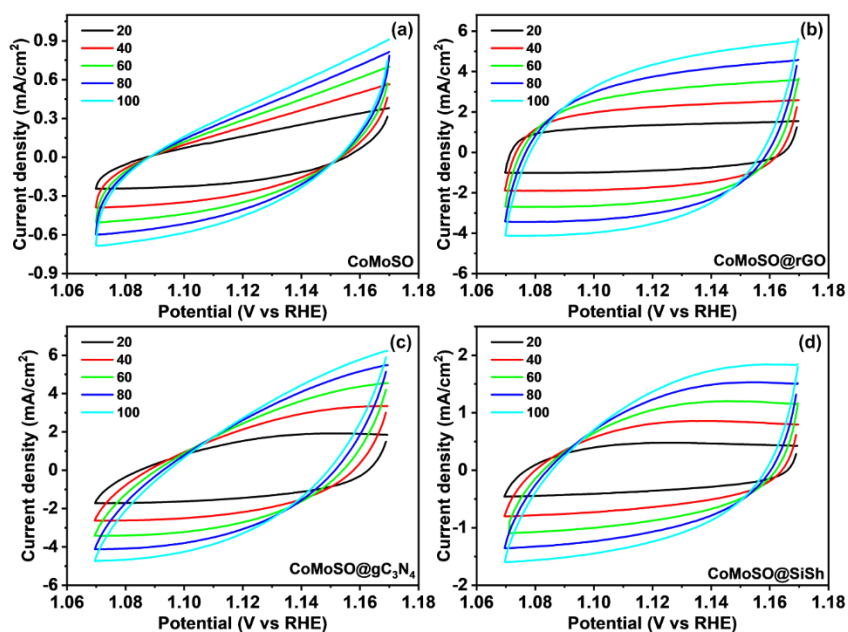


Figure 3.8: Cyclic voltammetry curves at scan rates from 20 to 100 mV/s of prepared materials

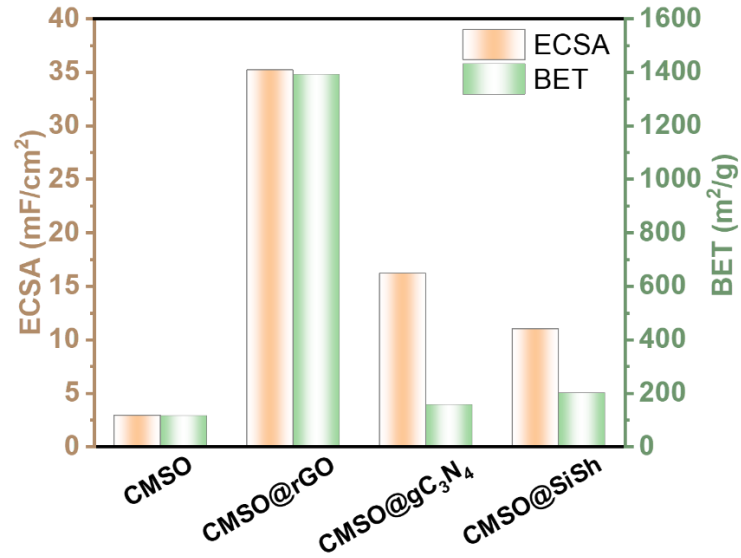


Figure 3.9: Comparison of BET and ECSA of synthesized materials

Table 3.2: OER properties and interfacial charge transfer resistance of various materials

Material	Overpotential at 10 mA/cm ² (mV)	Tafel slope (mV/dec)	Interface charge-transfer resistance (R_{ct}) (Ω)
CMSO	384	141	56.5
CMSO@rGO	259	85	3.9
CMSO@gC ₃ N ₄	270	109	17.5
CMSO@SiSh	287	86	23.1
RuO ₂	315	136	51.3

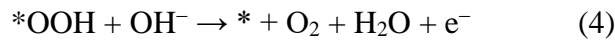
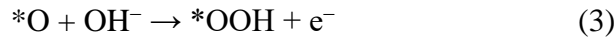
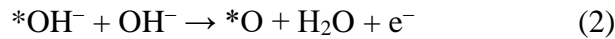
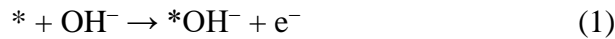
The role of 2D materials as templates for anchoring CMSO not only exposed more active sites to the electrolyte but also facilitated electron and charge transfer processes. The combination of the high surface area and superior conductivity of rGO might enable CMSO@rGO to achieve the fastest reaction rate compared to the other materials [160]. The observed overpotential and kinetics of CMSO@rGO fabricated herein were comparable to those of previously reported cobalt-based electrocatalysts (**Table 3.3** and **Figure 3.7(f)**), revealing the high potential of CMSO@rGO as a promising electrocatalyst for OER in water electrolysis.

Table 3.3: Comparison of OER activity in 1 M KOH of different electrocatalyst

Materials	Overpotential At 10 mA/cm ² (mV)	Tafel slope (mV/dec)	Stability (hour)	Reference
CoS ₂ -MoS ₂ hollow spheres	288	62.1	10	[161]
CoS ₂ -MoS ₂ nanosheet	266	-	24	[162]
Cobalt Covalent Doping in MoS ₂	260	85	11	[163]
Co-Mo-S-2/NF	294	65.85	120	[164]
MoS ₂ -CoS ₂ @PCMT	215	93	20	[165]
N-CoS ₂ /Graphene	260	56.3	8	[166]
MoS ₂ /NiCo ₂ O ₄	322	113	12	[167]
CMSO@rGO	259	85	40	This work

Stability is another key parameter to evaluate electrochemical catalysts. Chronoamperometry (CA) measurements at a constant current density were conducted to evaluate the stability of the investigated materials. The results are shown in **Figure 3.10(a)**. For CMSO, CMSO@rGO, CMSO@gC₃N₄, and CMSO@SiSh, the potentials applied to achieve a current density of ~10 mA/cm² were 1.60 V, 1.49 V, 1.50 V, and 1.52 V, respectively. The current density of CMSO, CMSO@gC₃N₄, and CMSO@SiSh started to decrease after 10 h of continuous operation. However, the current density of CMSO@rGO decreased negligibly, almost similar to that observed for the OER LSV curves (**Figure 3.10(b)**) and the unchanged morphology (**Figure 3.11**) even after 40 h of continuous operation, indicative of the superior long-term stability of as-prepared CMSO@rGO. The strong interaction between rGO sheets and CMSO might prevent the change in the morphology. Instead, a new peak was observed at 504 cm⁻¹ in the Raman spectrum of CMSO@rGO after 40 h of the OER process (**Figure 3.12(a)**), which could be attributed to the presence of CoOOH [168]. Similarly, in the XRD pattern of

CMSO@rGO after the stability test (**Figure 3.12(b)**), a new peak was observed at 20.2°, corresponding to the (003) plane of CoOOH (JCPDS No. 01-073-0497). The XPS deconvoluted spectrum of Co 2p after the stability test (**Figure 3.12(c)**) exhibited a positive shift, and two new peaks appeared at 780 and 795 eV, respectively, originating from the Co³⁺ species in CoOOH [169]. These results revealed that the active site CMSO on the rGO sheet was partially converted into CoOOH, corresponding to the reconstruction phenomenon that occurred typically on the surface of transition metal-based electrocatalysts in the water oxidation process [168, 170]. This result suggested that the Co sites in CMSO@rGO served as favorable catalytic reaction sites for OER. The presence of a highly active CoOOH surface possibly impeded the further oxidation of the core electrocatalyst, and the interaction between the in situ oxyhydroxide and the original catalyst might be favorable in driving water oxidation. Thus, the stability of the electrocatalyst was maintained during the OER process [17, 170]. The mechanism was described in the following reaction steps (* corresponds to an active site):



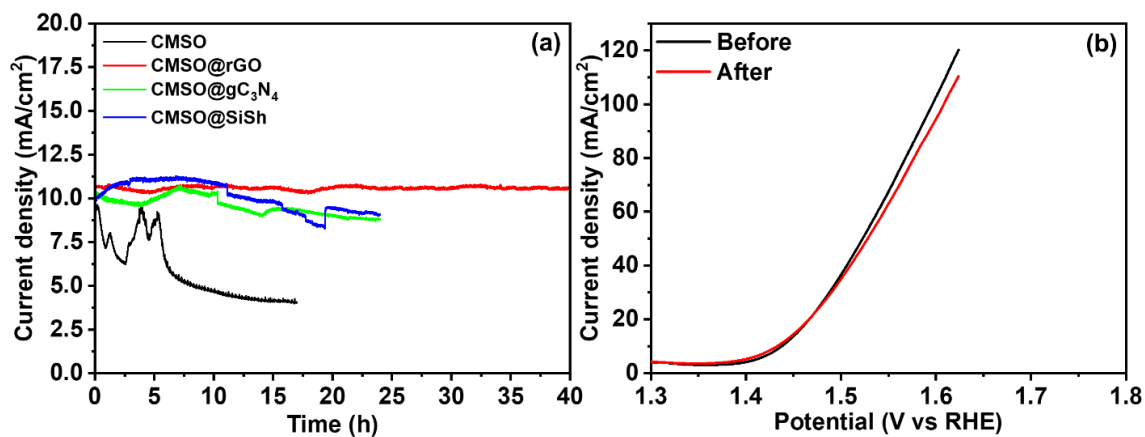


Figure 3.10: (a) Chronoamperometry curves of CMSO (at 1.60 V), CMSO@rGO (at 1.49 V), CMSO@ gC₃N₄ (at 1.50 V), and CMSO@SiSh (at 1.52 V). (b) LSV curves of CMSO@rGO before and after a 40-h stability test.

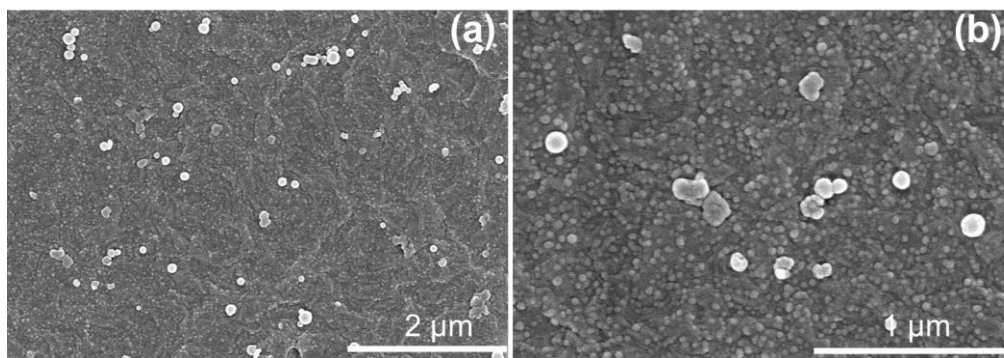


Figure 3.11: FESEM of CMSO@rGO at different magnification after OER

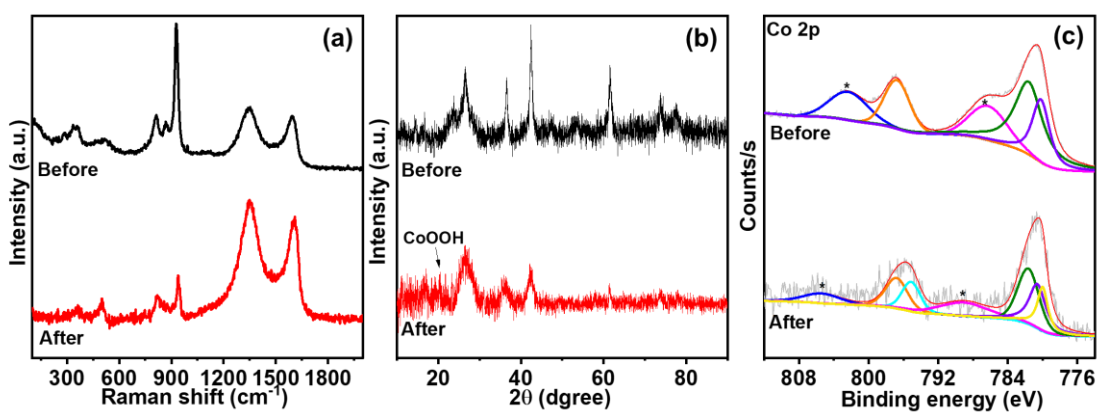


Figure 3.12: Comparison of (a) Raman spectrum, (b) XRD pattern, and (c) XPS of Co 2p of CMSO@rGO before and after OER

A two-electrode system with CMSO@rGO as the anode and Pt/C (20%) as the cathode was designed for overall water splitting to ensure stability and scalability in large-scale industrial applications. The LSV curve (**Figure 3.13(a)**) of this system indicated that the potential of the cell was reached 10 mA/cm² at 1.54 V, while that of the RuO₂//Pt/C system was greater by 60 mV. Even after a 40-h stability test, the chronopotentiometry curve of CMSO@rGO//Pt/C in **Figure 3.13(b)** exhibited excellent activity retention of 94.8%. Particularly, the potential slightly increased from 1.54 V to 1.62 V. This result indicated that CMSO@rGO demonstrated excellent long-term stability even for the overall water splitting reaction.

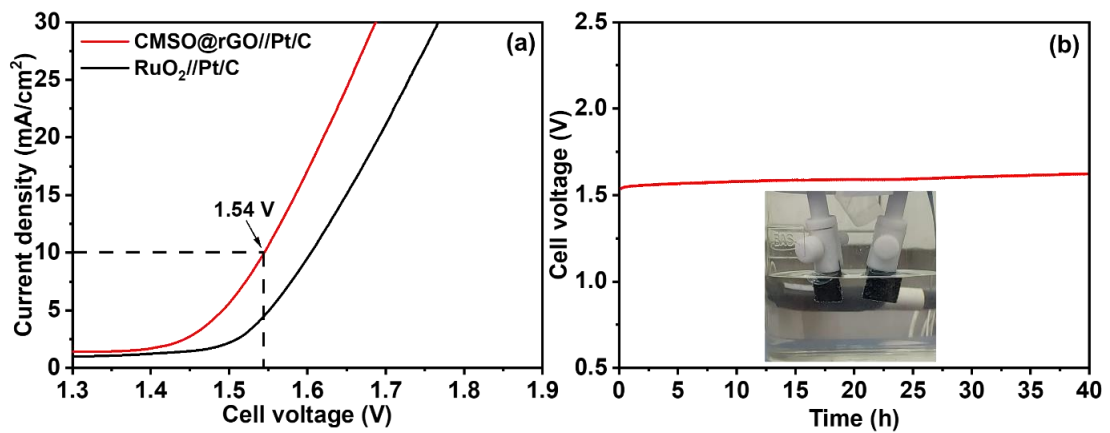


Figure 3.13: (a) LSV curves of two-electrode systems, (b) Chronopotentiometry curve for the overall water splitting reaction at 10 mA/ cm² (inset photograph: CMSO@rGO(anode)//Pt/C(cathode); the overall water splitting system)

3.4. Conclusion

In this study, Co and Mo bimetallic oxide/sulfide hybrid structures supported on various 2D materials such as rGO, gC₃N₄, and SiSh were successfully synthesized. Among these materials, CMSO@rGO exhibited the highest electrochemical activity, with a low overpotential and a Tafel slope of 259 mV at 10 mA/cm² and 85 mV/dec, respectively. Owing to the strong interaction between rGO and CMSO, the electronic structure of the composite system was modulated, promoting the formation of oxyhydroxide surfaces and optimizing the performance of the electrocatalyst in driving water oxidation. Furthermore, the current density of CMSO@rGO changed negligibly even after a 40 h long-term stability test with no clear physical and electronic deformation, which was attributed to the high number of functional groups and high surface area of rGO.

Part 3. Modulating the electronic structure

Chapter 4. Influence of Er_2O_3 on Transition Metal Oxides in Water oxidation application

4.1. Introduction

The generation of green hydrogen via water electrolysis is hindered by the oxygen evolution reaction (OER) half-reaction. Unlike its counterpart, the hydrogen evolution reaction (HER), which involves only two electron transfer steps, the OER process is more complicated, comprising four electron transfer steps [171]. Consequently, identifying an effective electrocatalyst for this process is paramount. Noble materials such as RuO_2 and IrO_2 serve as benchmarks for OER electrocatalysts. However, their widespread adoption is hindered by scarcity, high cost, and low stability [172]. Thus, a concerted effort exists to explore efficient nonmetal or non-noble metal electrocatalysts as substitutes for noble counterparts.

Among non-noble metal electrocatalysts, transition metal oxides (TMOs) like NiO , Co_3O_4 , and Fe_2O_3 have garnered attention for their notable attributes, including high stability in alkaline environments, abundance in the Earth's crust, cost-effectiveness, nontoxicity and high redox potential [134, 173-177]. However, pristine TMOs are hindered by low electrical conductivity [178]. To overcome this drawback, various strategies such as doping, support modification, defect engineering, and hybridization with other materials have been explored to tailor the chemical and physical properties of TMOs, rendering them more suitable for water electrolysis applications [39, 179]. Notably, defect engineering, particularly oxygen vacancy, stands out owing to its low formation energy in TMOs and its significant benefits for the OER [180].

Besides, the hybridization of TMOs with rare earth-based materials to form heterostructure electrocatalysts has proven effective. The large spatial population of the electronic wave function of 4f orbital can facilitate the strong coupling between d and f orbital, forming the d-f electronic ladder, thereby modifying the electronic structure of the electrocatalysts [181, 182]. Furthermore, rare earth-oxide materials exhibit favorable protective behaviors, exceptional thermal stabilities, and robust mechanical strengths, contributing to the overall stability enhancement of the electrocatalyst [182].

Based on the abovementioned information, incorporating rare earth oxide into TMOs holds promise for enhancing TMOs' OER performance. Thus, in this study, we hybridize Er_2O_3 with M_xO_y ($\text{M} = \text{Ni}, \text{Co}, \text{Fe}$) to form ErNiO , ErCoO , and ErFeO , respectively, to examine the influence of Er_2O_3 on the physicochemical properties of commonly utilized TMOs in water oxidation applications.

4.2. Experimental details

4.2.1. Material

Cobalt (II) nitrate hexahydrate ($\text{Co}(\text{NO}_3)_2 \cdot 6\text{H}_2\text{O}$), Nickel (II) nitrate hexahydrate ($\text{Ni}(\text{NO}_3)_2 \cdot 6\text{H}_2\text{O}$), ethanol ($\text{C}_2\text{H}_6\text{O}$), were purchased from Daejung chemicals. Erbium (III) nitrate pentahydrate ($\text{Er}(\text{NO}_3)_3 \cdot 6\text{H}_2\text{O}$), Iron (III) nitrate nonahydrate ($\text{Fe}(\text{NO}_3)_3 \cdot 9\text{H}_2\text{O}$), Urea ($\text{CO}(\text{NH}_2)_2$), Nafion 5%, ruthenium oxide (RuO_2), Pt/C 20%, and potassium hydroxide (KOH) were bought from Sigma-Aldrich. All of the chemicals were used without any purification after purchasing. Deionized water (DI) was used for all reactions.

4.2.2. Instrumental analysis

A DXR Raman microscope (Thermo Scientific) was employed to obtain the Raman spectra for all samples within the range collected from 100 to 2000 cm^{-1} using a 532 nm monochromatic excitation source. A homogeneous mixture of 1 wt.% sample and KBr was pressed to form a pellet, and the Fourier transform infrared (FTIR) analysis was obtained using Thermo Scientific Nicolet 200 FTIR spectrometer (USA) in the range of 4000-400 cm^{-1} . High resolution XRD patterns were conducted by A Bruker D8 Discover X-ray diffractometer employing Cu $K\alpha$ radiation (1.540593 Å) and scan range of 10-90°. The X-ray photoelectron spectroscopy (XPS) was carried out on thermo ESCALAB 250 Xi, Thermo Fisher Scientific of the USA, with Al $K\alpha$ X-ray radiation (1486.6 eV). Field emission scanning electron microscopy (FESEM) using a Hitachi High-Tech Corporation SU8200 instrument from Japan was utilized to observe the morphology of the materials. High resolution transmission electron microscopy (HR-TEM) was conducted by JEOL JEM 2100F. The degas and nitrogen adsorption-desorption isotherms were measured by a Quantachrome Quadrasorb SI automated surface area/pore size analyzer to reveal the surface area and pore size of the samples. The electron paramagnetic

resonance (EPR) was conducted by Bruker (EMXplus-9.5/2.7) instrument at frequency of 9.430 GHz.

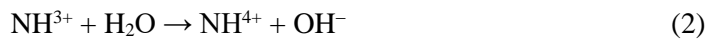
4.2.3. Preparation of working electrode and electrochemical measurements

All electrochemical experiments were performed at room temperature in an alkaline medium (1 M KOH) using a three-electrode system (BioLogic, Science Instruments). The setup comprised a reference electrode (RE), a counter electrode (CE), and a working electrode (WE). Specifically, the RE was a Hg/HgO electrode, the CE was a graphite rod, and nickel foam (NF) served as the WE. To prepare the WE, 3 mg of catalyst was combined with 300 μ L of DI, 190 μ L of ethanol, and 10 μ L of Nafion 5%, followed by 30 min of sonication to produce a homogeneous solution. Subsequently, 200 μ L of the resulting solution was dropped on NF substrate, resulting in a catalyst mass loading of 1.2 mg/cm². Before utilization, NF was cut into 1 \times 1 cm² pieces and then sequentially treated with 1 M hydrochloric acid (HCl), ethanol, and DI water for 30 min at each step, followed by 12 h of drying in an oven at 60 °C. The commercial RuO₂ underwent the same preparation procedure.

The RE was calibrated according to previously established procedures [15]. The potential obtained from the RE (Hg/HgO) was then converted to the standard reversible hydrogen electrode (RHE) using the Nernst equation: $E_{\text{RHE}} = E_{\text{Hg/HgO}} + 0.92$ (V). Linear sweep voltammetry (LSV) was performed at a scan rate of 5 mV/s in the potential range of 1–1.72 V versus RHE. Overpotential (η) was calculated using the formula $\eta = E_{\text{RHE}} - 1.23$ (V). Tafel slope (b) was determined as the slope of the linear fitting of the potential vs. RHE against $\log(j)$, utilizing the Tafel equation $\eta = b \times \log(j/j_0)$, where j represents the current density and j_0 denotes the exchange current density. Electrochemical impedance spectroscopy (EIS) was recorded over a frequency range of 10⁵ to 10⁻² Hz at 1.54 V vs. RHE. The electrochemical active surface area (ECSA) of the catalysts was calculated as $\text{ECSA} = C_{\text{dl}}/C_s$, where the specific capacitance C_s is 40 μ F/cm² [20] and the electrochemical double layer capacitance C_{dl} is determined as the slope of a straight line obtained from a plot of double layer charging current (i) as a function of scan rate (v), expressed by $i = v \times C_{\text{dl}}$ [20]. Chronopotentiometry (CP) experiments were conducted at a specific potential, resulting in a 10 mA/cm² current density.

4.2.4. Synthesis of ErMO (M=Ni, Co, Fe)

ErNiO, ErCoO, and ErFeO were synthesized using a combination of hydrothermal and vacuum annealing processes. In the hydrothermal step, the reaction between Er^{3+} and M^{n+} (M representing Ni, Co, or Fe) with urea led to the formation of $\text{Er}(\text{OH})_3$ and $\text{M}(\text{OH})_n$, as illustrated in reactions (1–4) [183]. Following this, the precursor $\text{M}(\text{OH})_n/\text{Er}(\text{OH})_3$ was converted into the respective oxide phase during the vacuum annealing process.



The procedure is outlined in Scheme 4.1. Initially, 0.125 mL of 1 M $\text{Er}(\text{NO}_3)_3$ and 1 mL of 1 M $\text{Fe}(\text{NO}_3)_3$ were dissolved in 5 mL of deionized water (DI) and stirred for 10 min to form solution A. Concurrently, solution B was prepared by dissolving 0.3 g of urea in 10 mL of DI water under magnetic stirring for 10 min. The mole ratio of reactants (Er^{3+} : Fe^{3+} : urea) was maintained at 1:8:30. Subsequently, solution A was slowly added dropwise to solution B. The resulting mixture was stirred for 30 min and then transferred to a 100-mL Teflon-lined stainless-steel autoclave, where it was maintained at 140 °C for 12 h. The powder was collected after centrifugation with DI water and ethanol, followed by vacuum drying at 70 °C for 12 h. Finally, the product, denoted as ErFeO, was annealed at 550 °C for 4 h under vacuum.

The same procedure was employed to synthesize ErCoO and ErNiO, with the substitution of 1 M $\text{Fe}(\text{NO}_3)_3$ with 1 M $\text{Co}(\text{NO}_3)_2$ and 1 M $\text{Ni}(\text{NO}_3)_2$, respectively.

TMOs (Co_3O_4 , Fe_2O_3 , NiO) were prepared using a similar method, excluding adding erbium nitrate to solution A.

4.3. Results and discussion

4.3.1. Characterization of ErMO (M=Ni, Co, Fe)

The composition and crystalline phases of the materials are depicted in **Figure 4.1(a)**. The X-ray diffraction (XRD) pattern of NiO exhibited five distinct peaks at 37.23°, 43.25°, 62.82°, 75.35°, and 79.34°, corresponding to the planes (003), (012), (104), (021), and (006) of the trigonal crystal NiO (JCPDS No. 01-078-4359). The diffraction peaks of Co₃O₄ confirmed the formation of a cubic phase consistent with JCPDS No. 00-043-1003. For Fe₂O₃, the XRD pattern closely matched the trigonal crystal structure as per JCPDS No. 00-033-0664. Notably, the XRD patterns of NiO, Co₃O₄, and Fe₂O₃ exhibited well-defined sharp peaks, indicating their high crystallinity. Upon modification by Er₂O₃, new peaks emerged at around 29° and 48° in the XRD patterns of ErNiO, ErCoO, and ErFeO, distinctly attributable to the presence of planes (222) and (440) of the cubic crystal Er₂O₃ (JCPDS No. 01-077-0461). These additional peaks highlighted the existence of Er₂O₃ and its influence on modifying the crystalline structure of the pristine oxides.

Figure 4.1(b) shows the Raman spectra of the synthesized materials. The spectrum of Er₂O₃ exhibited dominant peaks at 259, 749, and 1069 cm⁻¹, consistent with previous studies [184]. The Raman spectrum of NiO revealed broad peaks at 1550 and 1059 cm⁻¹ and a prominent peak at 510 cm⁻¹, attributed to the two-magnon (2M), two-phonon (2LO), and one-phonon longitudinal optical (LO) modes, respectively. The presence of the intense LO peak indicated surface defects or the presence of Ni³⁺ in the material [185]. In the case of Co₃O₄, the Raman spectrum displayed peaks at 187, 466, 508, 604, and 672 cm⁻¹, corresponding to F_{12g}, E_g, F_{22g}, F_{32g}, and A_{1g} modes, respectively. The F_{12g} and A_{1g} peaks were associated with the vibration modes of tetrahedral (CoO₄) and octahedral (CoO₆) configurations, characteristic of Co²⁺ and Co³⁺ in the material [186]. Meanwhile, the Raman spectrum of Fe₂O₃ exhibited a peak at 217 cm⁻¹ (A_{1g}), along with peaks at 270, 378, and 571 cm⁻¹ (E_g), and a broad peak around 1300 cm⁻¹, indicative of the pure hematite (α -Fe₂O₃) phase [187]. Comparatively, the Raman spectra of ErNiO, ErCoO, and ErFeO displayed shifts and additional peaks attributed to Er₂O₃ compared to the pristine oxides' spectra. These shifts may arise from interfacial strain or lattice distortion induced by strong interactions at the interface of oxides and Er₂O₃ [186].

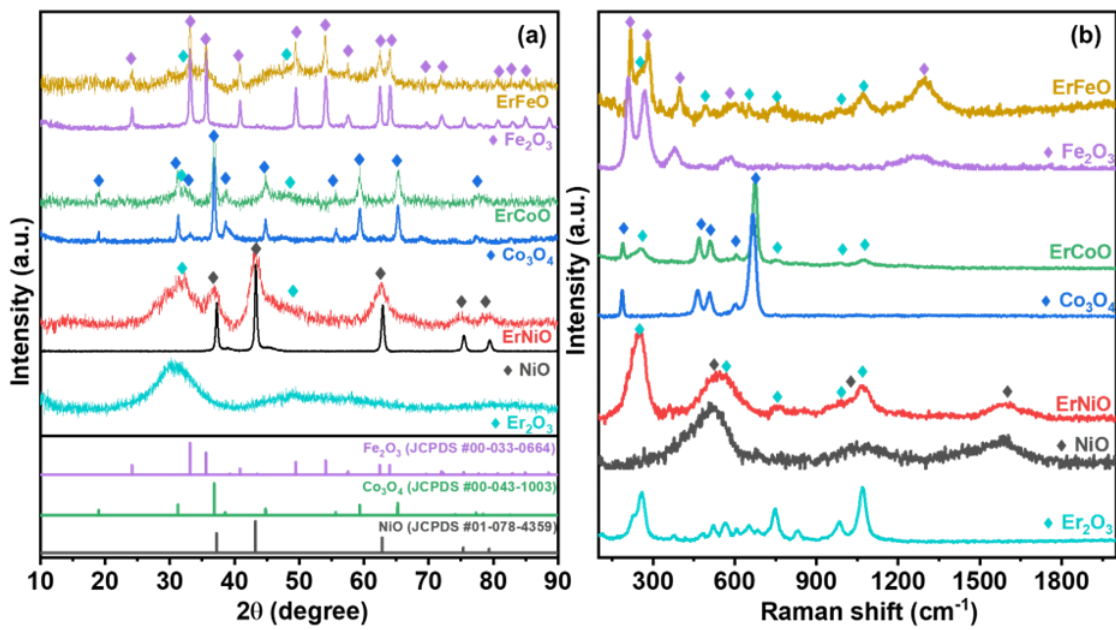


Figure 4.1: (a) XRD patterns and (b) Raman spectra of the synthesized materials

Additional structural information and chemical composition details of the prepared materials were obtained from the Fourier transform infrared spectra (FTIR), presented in **Figure 4.2(a)**. The FTIR spectrum of Er_2O_3 displayed peaks at 1407 and 1532 cm^{-1} , corresponding to the stretching vibration of the Er–O bond [188]. In the FTIR spectrum of ErNiO , along with the stretching vibration of Er_2O_3 , peaks at 450 and 3445 cm^{-1} were attributed to the bending of Ni–O and stretching of O–H, respectively [189]. For ErCoO , prominent vibrational modes were observed, including stretching of Co–O at 561 cm^{-1} , bridging of O–Co–O at 664 cm^{-1} [190], stretching of Er–O at 1394 and 1526 cm^{-1} , and stretching of O–H at 3389 cm^{-1} . In the case of ErFeO , adsorption bands at 483 and 576 cm^{-1} were assigned to the Fe–O vibration [191], while peaks at 1384 and 1528 cm^{-1} were attributed to the Er–O vibration band. The FTIR spectra of ErNiO , ErCoO , and ErFeO displayed shifts in the peaks associated with the Er–O vibration mode compared to the pristine Er_2O_3 FTIR spectrum. These shifts emphasized the interactions between the respective oxides and Er_2O_3 .

The nitrogen adsorption–desorption isotherm curves, obtained through Brunauer–Emmett–Teller (BET) measurements, are depicted in **Figure 4.2(b)**. All materials exhibited a type IV isotherm with a hysteresis loop type H3, in accordance with the IUPAC classification [75]. The specific surface areas of ErNiO , NiO , ErCoO , Co_3O_4 , ErFeO , and Fe_2O_3 were determined to be 70.92, 65.71, 27.88, 2.59, 84.21, and 31.58 m^2/g , respectively. Notably, the modification with Er_2O_3 positively influenced the specific surface areas of the oxides. The pore size distribution plot in **Figure 4.3** revealed a mesoporous structure in the materials, rendering them promising candidates for electrochemical reactions. Such a structure allows for more exposed sites for electrocatalytic reactions and facilitates the easy transportation of intermediates [192]. A summary of the specific surface area, pore size, and pore volume is provided in **Table 4.1**.

Table 4.1: Specific surface area, pore volume, and pore radius of the synthesized materials

Materials	Specific surface area (m^2/g)	Pore volume (cc/g)	Pore radius (nm)
NiO	65.71	0.17	4.46
ErNiO	70.92	0.18	2.38
Co_3O_4	2.59	0.10	10.03
ErCoO	27.88	0.16	6.39
Fe_2O_3	31.58	0.07	5.59
ErFeO	84.21	0.16	5.59

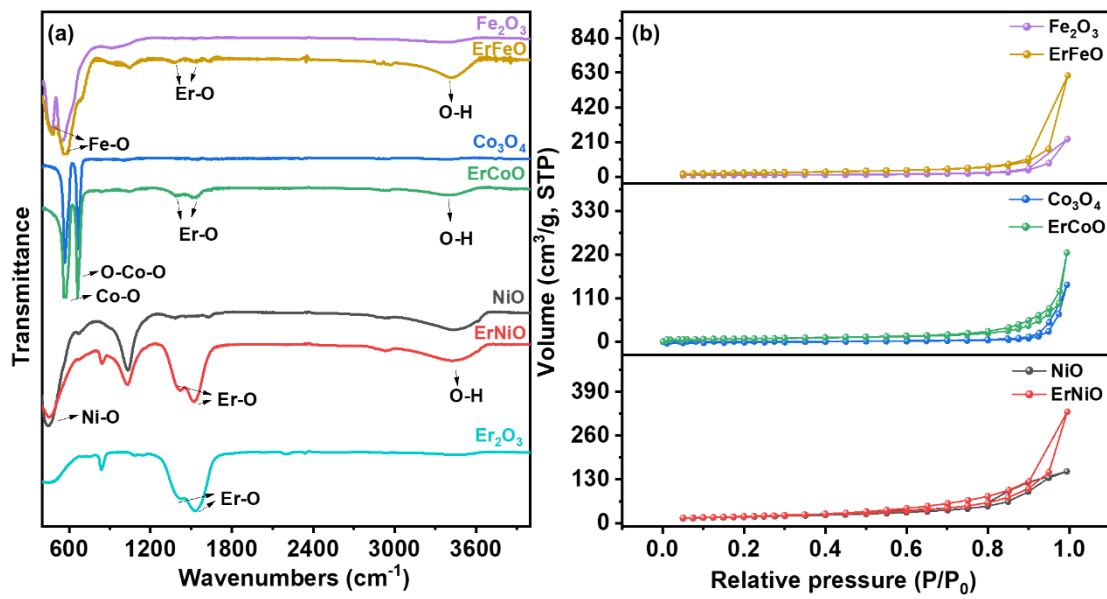


Figure 4.2: (a) FTIR spectra and (b) N₂ adsorption–desorption isotherms of the as-prepared samples

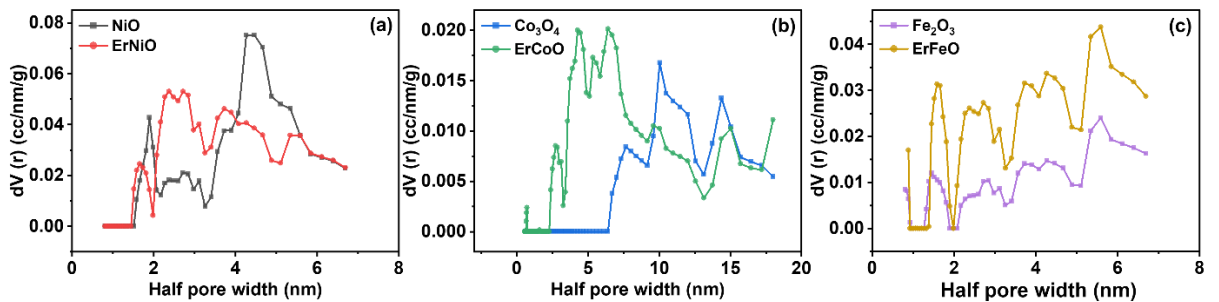


Figure 4.3: Pore size distribution by density functional theory method of (a) NiO, ErNiO, (b) Co₃O₄, ErCoO, and (c) Fe₂O₃, ErFeO

The morphology of the prepared samples was examined using field emission scanning electron microscopy (FESEM). Er_2O_3 exhibited a nanoparticle cluster forming a quasi-spherical morphology (**Figure 4.4**). NiO displayed a nanosheet structure (**Figure 4.5(a)**). After the introduction of Er_2O_3 , the shapes of NiO and Er_2O_3 remained, resulting in the distribution of Er_2O_3 quasi-sphere clusters on NiO nanosheets (**Figure 4.5(b)**). Similarly, the quasi-sphere cluster of Er_2O_3 nanoparticles and the nanorods of Co_3O_4 maintained their morphology in ErCoO (**Figure 4.5(c,d)**). However, in the case of ErCoO, the cluster of Er_2O_3 nanoparticles exhibited a smaller size than pristine Er_2O_3 . Conversely, Fe_2O_3 exhibited nanoparticle morphology (**Figure 4.4(e)**). In ErFeO, the iron oxide nanoparticles were interwoven into the quasi-spherical cluster of Er_2O_3 (**Figure 4.5(f)**). This interweaving phenomenon suggests that Er_2O_3 may serve as the anchor site for Fe_2O_3 , enhancing stability in the electrochemical process. The elemental mapping of ErNiO, ErCoO, and ErFeO in **Figure 4.6** revealed the distribution of constituent elements.

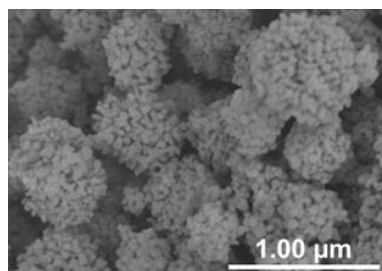


Figure 4.4: FESEM of Er_2O_3

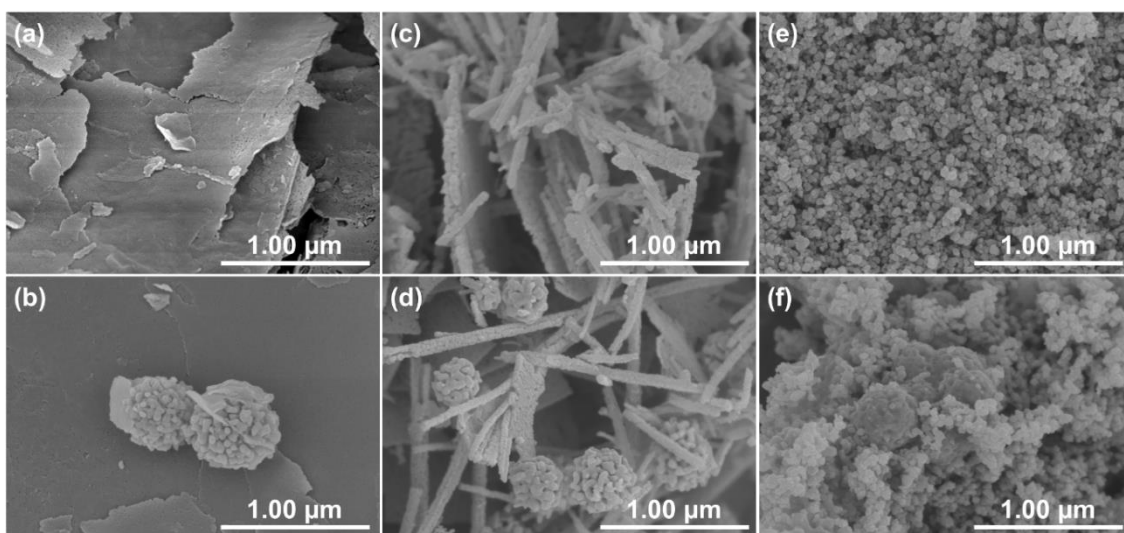


Figure 4.5: FESEM of (a) NiO, (b) ErNiO; (c) Co_3O_4 , (d) ErCoO; (e) Fe_2O_3 , and (f) ErFeO

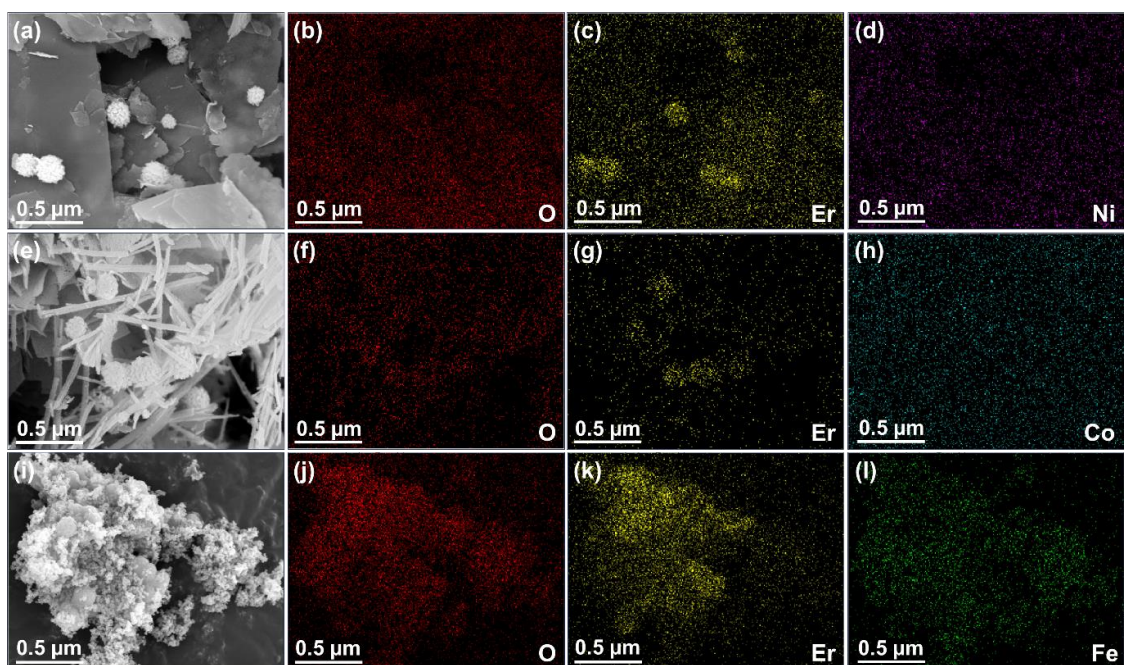


Figure 4.6: Elemental mapping of (a-d) ErNiO, (e-h) ErCoO, and (i-l) ErFeO

The heterojunctions in the prepared materials were further revealed using high-resolution transmission electron microscopy (HR-TEM), as shown in **Figure 4.7**. In the case of ErNiO (**Figure 4.7(a,b)**), distinct d-spacings of 0.305 and 0.240 nm were observed, corresponding to the lattice fringes of Er₂O₃ (222) (JCPDS No. 01-077-0461) and NiO (003) (JCPDS No. 01-078-4359), respectively. ErCoO (**Figure 4.7(c,d)**) exhibited heterojunctions at the interfaces of Co₃O₄ (222) (JCPDS No. 00-043-1003) and Er₂O₃ (222), (400) (JCPDS No. 01-077-0461). Notably, in the case of ErFeO (**Figure 4.7(e,f)**), numerous heterojunctions between Er₂O₃ (JCPDS No. 01-077-0461) and Fe₂O₃ (JCPDS No. 01-077-0461) were observed, including Er₂O₃ (222) and Fe₂O₃ (134), Er₂O₃ (222) with Fe₂O₃ (113), Er₂O₃ (420) with Fe₂O₃ (113), and Er₂O₃ (420) and Fe₂O₃ (024). Furthermore, in **Figure 4.7(f)**, the d-spacings of Fe₂O₃ (113), (024), and (134) were found to be smaller than those observed in pristine Fe₂O₃ (JCPDS No. 01-077-0461), measuring 0.219, 0.182, and 0.112 nm, respectively, compared to 0.221, 0.184, and 0.114 nm. Similarly, the d-spacings of NiO and Co₃O₄ in ErNiO and ErCoO were also smaller than their counterparts in the JCPDS of pristine TMOs. This reduction can be attributed to the compressive strain caused by introducing Er₂O₃ into the TMOs. This aligns with the observed blue shift phenomenon in the Raman spectra of ErNiO, ErCoO, and ErFeO. The abundance of heterojunctions in ErFeO can facilitate the charge/electron transfer rate in electrochemical reactions, suggesting that ErFeO may serve as a promising electrocatalyst among the prepared electrocatalysts.

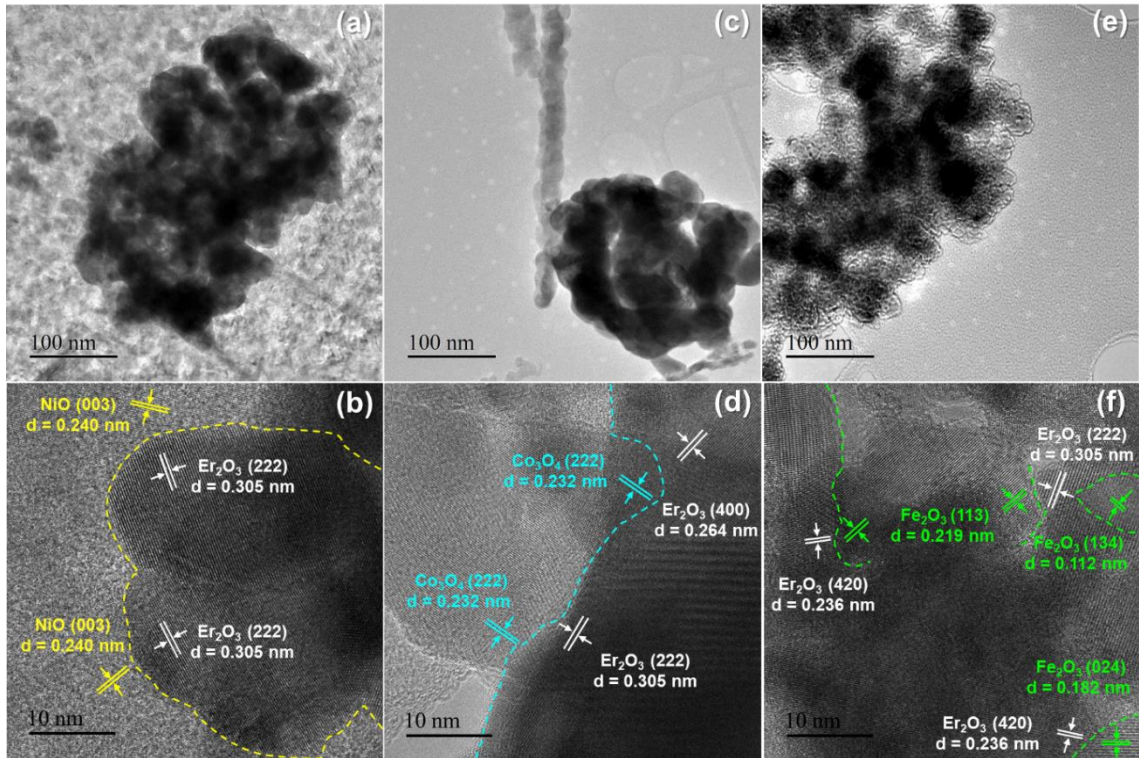


Figure 4.7: HRTEM of (a,b) ErNiO, (c,d) ErCoO, and (e,f) ErFeO

X-ray photoelectron spectroscopy (XPS) was employed to investigate the synthesized materials' elemental composition and oxidation states. The survey XPS spectra of all materials, depicted in **Figure 4.8**, utilized carbon (C) as a reference for binding energy calibration. The survey XPS spectrum of ErNiO confirmed the presence of Er, Ni, and O elements in the material. In **Figure 4.9(a)**, Ni 2p was deconvoluted into eight peaks with binding energies at 853.8 eV ($2p_{3/2}$) and 871.3 eV ($2p_{1/2}$), assigned to Ni^{2+} , while 855.5 eV ($2p_{3/2}$) and 872.9 eV ($2p_{1/2}$) corresponded to Ni^{3+} [193]. The remaining four peaks were attributed to shake-up satellite peaks of two different oxidation states of Ni. The coexistence of Ni^{2+} and Ni^{3+} was consistent with the Raman results. High-resolution O 1s XPS of ErNiO (**Figure 4.9(b)**) revealed three peaks at 529.3, 531.3, and 532.4 eV, representing lattice oxygen (O^1), non-stoichiometric oxygen (O^2), and adsorbed surface water molecules (O^3), respectively [194].

In the XPS survey spectrum of ErCoO, Er, Co, and O elements were identified. The deconvoluted spectrum of Co 2p displayed four strong peaks corresponding to spin-orbit splitting of Co $2p_{3/2}$ at 779.4 eV (Co^{3+}) and 780.5 eV (Co^{2+}), and Co $2p_{1/2}$ at 794.5 eV (Co^{3+}) and 796.1 eV (Co^{2+}) [195] (**Figure 4.9(c)**). The deconvoluted spectrum of O 1s (**Figure 4.9(d)**) exhibited the prominent peak of lattice oxygen belonging to Co–O at 529.9 eV [195].

The survey spectrum of ErFeO revealed the presence of Er, Fe, and O elements. In **Figure 4.9(e)**, the peaks at 709.5 and 722.9 eV were attributed to Fe^{2+} , while those at 711.1 and 724.5 eV corresponded to Fe^{3+} [196]. Similarly, the peak of O 1s in ErFeO was deconvoluted into three oxygen types, O^1 , O^2 , and O^3 (**Figure 4.9 (f)**).

Compared to their pristine oxide counterparts, ErNiO, ErCoO, and ErFeO displayed higher ratios of Ni^{2+}/Ni^{3+} , Co^{2+}/Co^{3+} , and Fe^{2+}/Fe^{3+} , along with increased O^2/O values (**Table 4.2**). Furthermore, the peaks observed in the Ni 2p, Co 2p, and Fe 2p spectra exhibited shifts toward lower binding energies, while the Er 4d peak shifted toward higher binding energies (**Figure 4.10**). These shifts were attributed to electron transfer from the Er 4d orbitals to the transition metal 3d orbitals, facilitated by Er's relatively lower electronegativity (1.24) compared to Ni (1.91), Co (1.88), and Fe (1.83) [197]. Consequently, the electron densities of Fe, Ni, and Co increased, leading to changes in the local coordination of oxygen atoms and the electronic structure of ErNiO, ErCoO, and ErFeO. These electronic reconstructions can impact

the energy barrier and intrinsic activity of the electrocatalyst, resulting in different adsorption energies of intermediates and thereby accelerating the whole reaction in the OER process.

Table 4.2: XPS results of all the materials

Materials	Ni ²⁺ /Ni ³⁺	Co ²⁺ /Co ³⁺	Fe ²⁺ /Fe ³⁺	O ² /O
NiO	0.51	-	-	0.28
ErNiO	0.59	-	-	0.47
Co ₃ O ₄	-	0.95	-	0.27
ErCoO	-	1.01	-	0.31
Fe ₂ O ₃	-	-	0.95	0.24
ErFeO	-	-	1.21	0.45

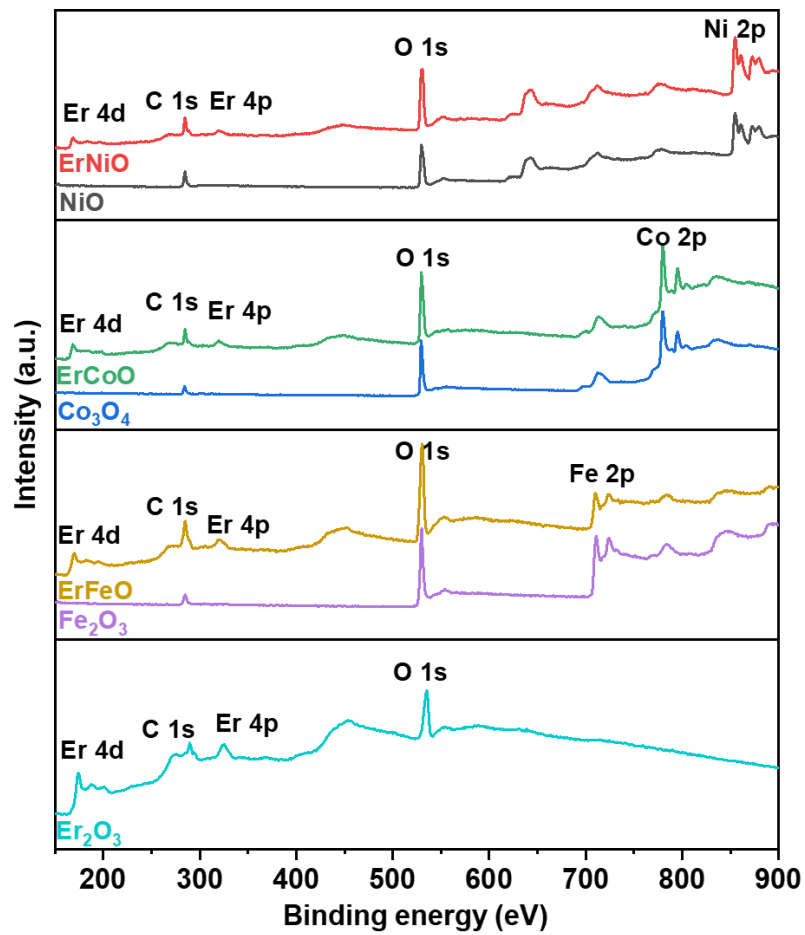


Figure 4.8: XPS survey spectra of prepared materials

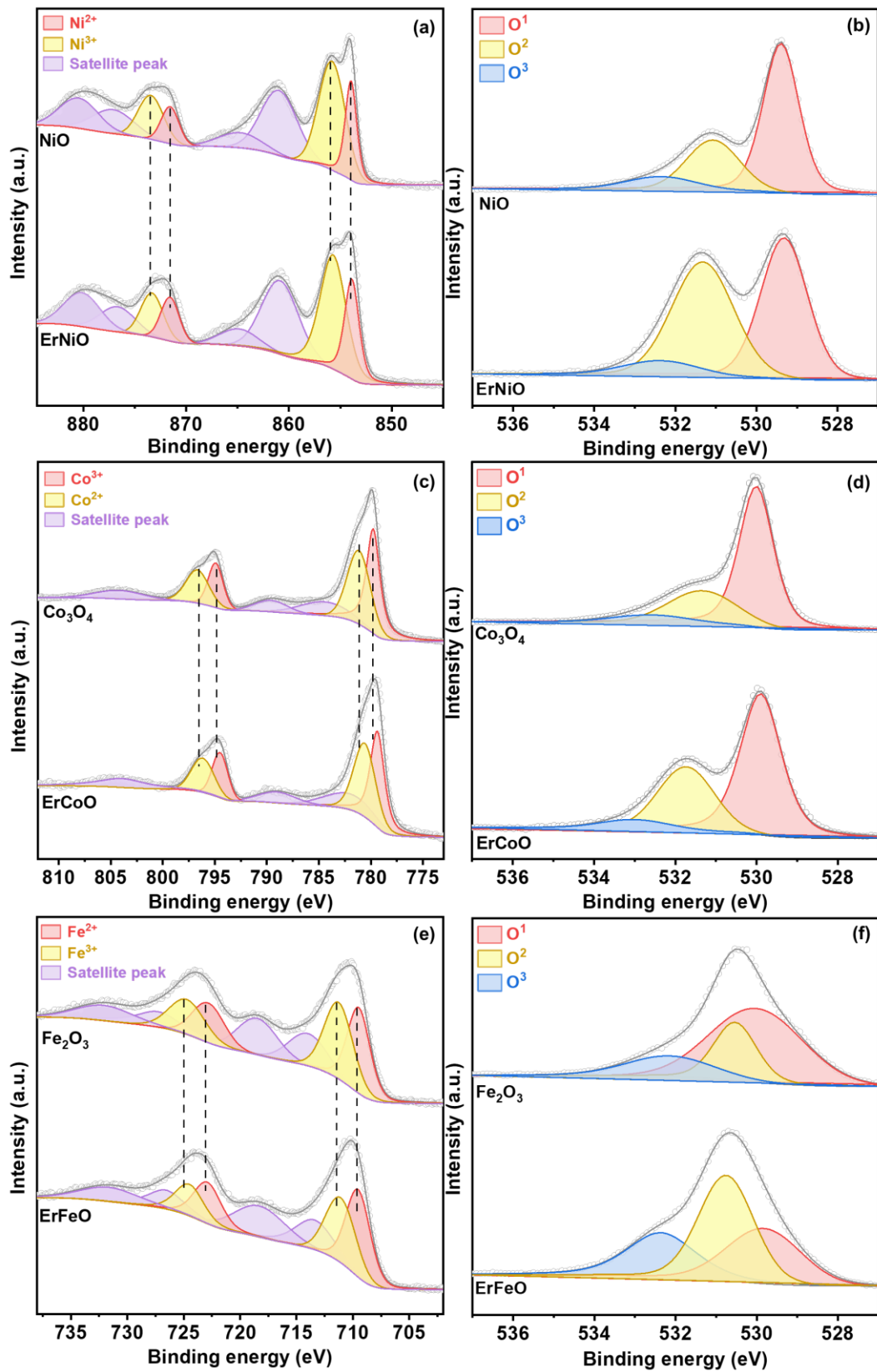


Figure 4.9: XPS spectra of (a) Ni 2p, (b) O 1s of NiO and ErNiO; (c) Co 2p; (d) O 1s of Co₃O₄ and ErCoO; and (e) Fe 2p, (f) O 1s of Fe₂O₃ and ErFeO

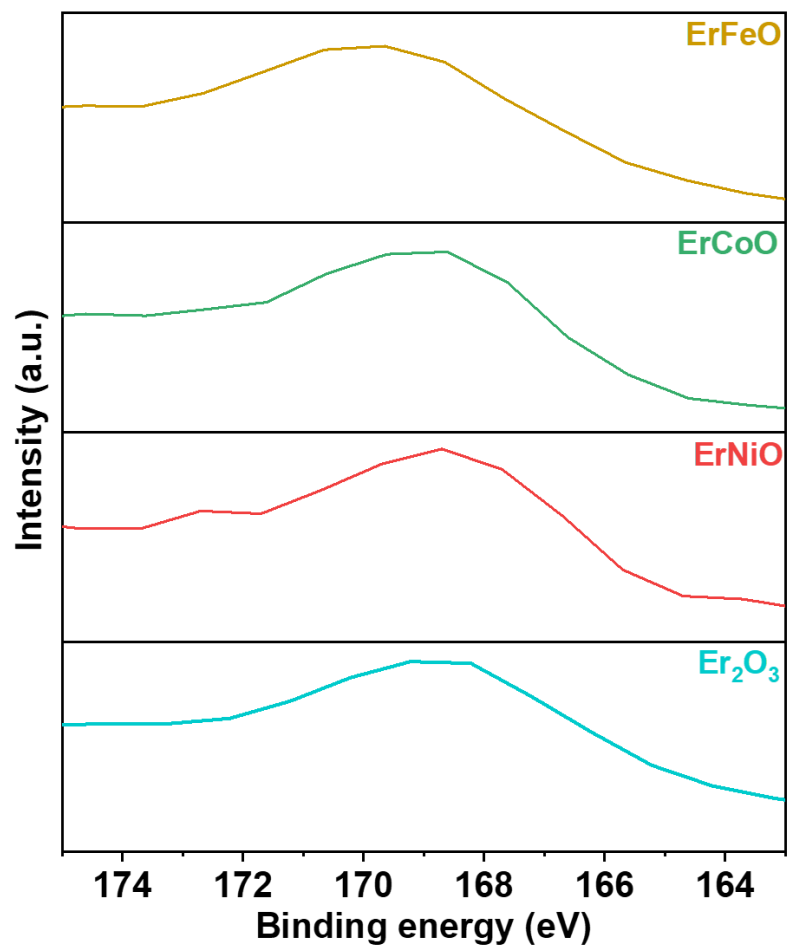


Figure 4.10: XPS spectra of Er 4d of prepared materials

The presence of the O^2 peak in all materials prompted further investigation into the potential presence of oxygen vacancies using electron paramagnetic resonance (EPR). As illustrated in **Figure 4.11(a,b)**, the EPR spectrum of Fe_2O_3 exhibited a weak signal at $g = 2.003$, attributed to the existence of oxygen vacancies [198]. Remarkably, this signal was significantly enhanced in the EPR spectrum of $ErFeO$, attributed to a substantial increase in the Fe^{2+}/Fe^{3+} ratio following the introduction of Er_2O_3 . This rise in ratio can be attributed to the interweaved morphology of Fe_2O_3 and Er_2O_3 , resulting in abundant interfaces between them, thereby enhancing electron transfer efficiency, as evidenced by the notable positive shift observed in the Er 4d signal in XPS analysis of $ErFeO$. Consequently, an abundance of oxygen vacancies was observed in $ErFeO$.

The preceding discussion and analysis confirmed that Er_2O_3 successfully modified NiO , Co_3O_4 , and Fe_2O_3 to yield $ErNiO$, $ErCoO$, and $ErFeO$. Among these synthesized materials, mesoporous $ErFeO$ exhibited the highest specific surface area, abundant oxygen vacancies, and the strong interaction at the heterojunction interface, owing to its interwoven structure. Consequently, it is anticipated that $ErFeO$ may demonstrate superior electrocatalytic performance compared to the other synthesized materials.

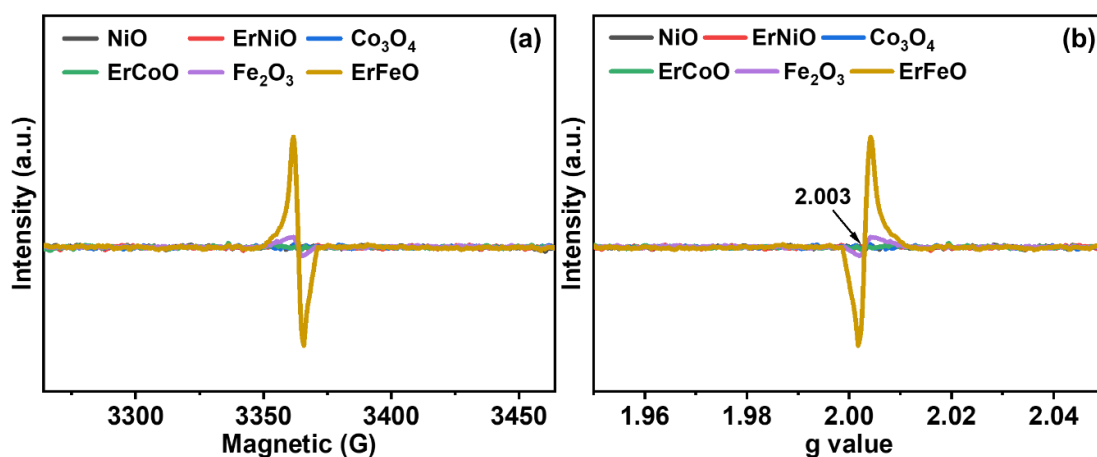


Figure 4.11: (a) EPR spectra and (b) g-factor of the synthesized materials

4.3.2. Electrochemical activity of ErMO (M=Ni, Co, Fe) towards oxygen evolution reaction

The electrochemical activity of the materials was evaluated through LSV measurements, as depicted in **Figure 4.12(a)**. Before LSV, cyclic voltammetry (CV) was performed to ensure the stability of the electrocatalyst. The electrocatalyst's performance was assessed based on the η required to achieve a current density of 10 mA/cm² (η_{10}), corresponding to a 10% solar energy conversion efficiency [20]. The η_{10} values followed the order of NiO < ErNiO < Co₃O₄ < ErCoO < Fe₂O₃ < RuO₂ < ErFeO. The enhanced activity of ErNiO, ErCoO, and ErFeO compared to their pristine oxide counterparts indicated a positive influence of Er₂O₃ on the electrochemical activity during the OER. In **Figure 4.12(b)**, a comparison of the onset potential and η_{10} is presented, revealing slight differences in the onset potential and η_{10} between ErNiO and ErCoO compared to NiO and Co₃O₄, respectively, whereas notable differences were observed between ErFeO and Fe₂O₃, underscoring the significant impact of Er₂O₃ on the activity of ErFeO in the water oxidation process. Despite RuO₂ displaying a lower onset potential, ErFeO exhibited a smaller η , particularly at 100 mA/cm². Specifically, the overpotential at 100 mA/cm² (η_{100}) for ErFeO was 360 mV, compared to 430 mV for RuO₂. The Tafel slope, an essential parameter for evaluating the kinetic properties of an electrocatalyst [25], is presented in **Figure 4.12(c)**. The smallest Tafel slope of ErFeO (80 mV/dec) indicates the fastest kinetic rates in the OER reactions, attributed to the abundance of oxygen vacancies, optimizing the absorption/desorption intermediates ability of ErFeO in the OER reaction [180].

EIS was conducted to better understand the material's kinetic reactions, as depicted in **Figure 4.12(d)**. The Nyquist plot revealed that the ErFeO electrode exhibited the smallest semicircle diameter, indicating the lowest charge transfer resistance (R_{ct}) and the highest electron transfer rate conductivity. This suggests a significant enhancement in reaction kinetics, highlighting the role of Er₂O₃ as a modulator of the electronic structure of TMOs, thereby enhancing their conductivity. Furthermore, the heterojunctions formed at the interfaces of the materials contributed to enhancing charge/electron transfer, ultimately improving the electrocatalytic performance of the OER. ECSA analysis was conducted to evaluate the intrinsic activity of the electrocatalyst. The C_{dl} results were calculated and depicted in **Figure 4.12(e)**, derived from CV data recorded in the nonfaradaic range between 1.06 and 1.18 V at various scan rates, as illustrated in **Figure 4.13(a-f)**. Because ECSA is directly proportional to C_{dl} , an

increased C_{dl} indicated an increment in the ECSA value in the order of NiO < ErNiO < Co₃O₄ < ErCoO < Fe₂O₃ < ErFeO. This suggests that Er₂O₃ contributes to the increase in active sites. **Table 4.3** summarizes the electrocatalytic performance of various materials, while **Table 4.4** compares ErFeO in this study with recently reported iron-based electrocatalysts used for OER applications.

Table 4.3: The summarized activities of the synthesized materials toward the OER

Material	Overpotential (η_{10}) (mV)	Tafel slope (b) (mV/dec)	Interface charge transfer resistance (R_{ct}) (Ω)
NiO	389	220	20.12
ErNiO	378	183	20.08
Co ₃ O ₄	366	145	9.93
ErCoO	344	165	9.76
Fe ₂ O ₃	304	110	1.46
ErFeO	250	80	0.42
RuO ₂	258	130	1.33

Table 4.4: Comparison of OER activity in 1 M KOH of different electrocatalyst

Materials	η_{10} (mV)	b (mA/dec)	Stability (hour)	Reference
Fe _{0.7} Co _{0.3} CeO _y	320	98.4	24	[199]
Fe ₂ O ₃ /Fe _{0.64} Ni _{0.36} @C-800	274	82.98	15	[200]
NiFe ₂ O ₄ /rGO	327	103	8.33	[201]
Fe ₃ C/Fe-N-C	349	85.3	-	[202]
m-Fe/N-C@CNT	338	104.9	-	[203]
Fe ₃ Ni ₇ N@C	290	40	12	[204]
NiCo ₂ O ₄ @NiFe-LDH	270	74	25	[205]
ErFeO	250	80	30	This work

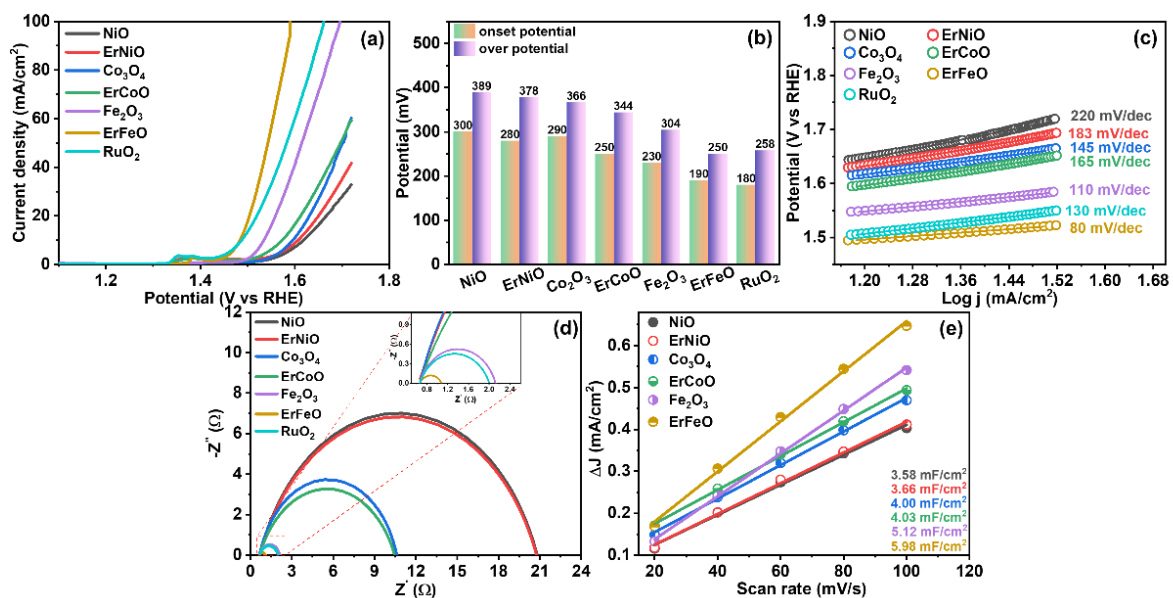


Figure 4.12: (a) LSV curves, (b) Comparison of overpotential, (c) Tafel slope, (d) Nyquist plots, and (e) Linear fitting of current density against scan rates of the synthesized materials

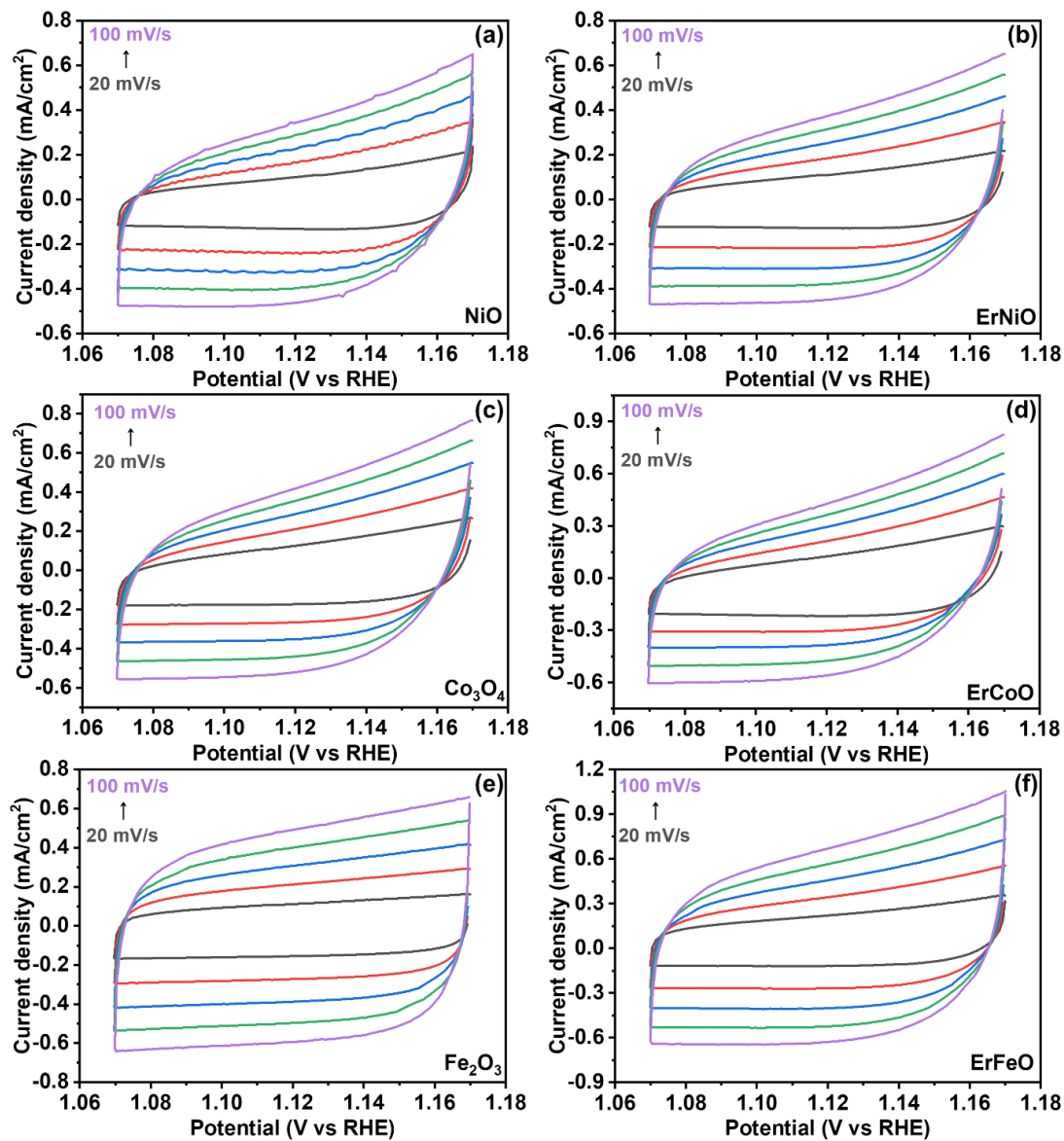


Figure 4.13: the cyclic voltammetry in the non-faradaic region of OER of synthesized materials

CP was employed to evaluate the stability of the electrocatalyst materials. Following a 30-h OER operation, the CP curve of ErFeO exhibited a consistent straight line with a minor shift in potential. In contrast, the CP curves of other materials displayed fluctuating lines and significant potential variations (**Figure 4.14(a)**). The LSV polarization curves of ErFeO before and after the durability test showed minimal differences (**Figure 4.14(b)**), indicating the long-term stability of ErFeO during the OER process attributed to the introduction of Er₂O₃ into Fe₂O₃. The inherently low negative enthalpy formation of Er₂O₃ imparted anticorrosive properties [182], suggesting its potential role as a protective layer, enhancing the stability of ErFeO during the water oxidation process. Following stability testing, ErFeO exhibited a morphology comparable to its initial state, as depicted in **Figure 4.15(a)**. The XRD pattern in **Figure 4.15(b)** of ErFeO after the 30-h long-term durability test showed consistent peaks with those observed before the OER reaction, albeit with slight intensity variations. Notably, a new peak at 17.2° emerged, attributed to the (020) plane of FeOOH (JCPDS No. 29-0173), suggesting that Fe₂O₃ acted as the active component in the ErFeO electrocatalyst, with its surface partially reconstructed to form the oxyhydroxide. This finding was consistent with the high-resolution XPS spectrum of Fe 2p after OER, as shown in **Figure 4.15(c)**, where the ratio of Fe²⁺/Fe³⁺ decreased compared to that before the OER process. The O 1s spectrum of ErFeO post-OER in **Figure 4.15(d)** was deconvoluted into three peaks, maintaining consistency with the pre-OER spectrum. However, analysis of the ratios in **Table 4.5** revealed an increase in the O³/O ratio and a decrease in the O²/O ratio, suggesting a decrease in partial oxygen vacancies, likely attributed to the adsorption of OH⁻ species [199].

Table 4.5: XPS results of ErFeO before-after OER process

Materials	Fe ²⁺ /Fe ³⁺	O ² /O	O ³ /O
Pre OER	1.21	0.45	0.24
Post OER	1.17	0.43	0.26

Based on the abovementioned analysis, the outstanding OER performance of ErFeO can be attributed to synergistic effects stemming from the combination of Fe₂O₃ and Er₂O₃. The OER primarily occurred at the active sites of Fe₂O₃, with Er₂O₃ acting as a promoter, modulating the electronic structure and enhancing the conductivity of ErFeO. The introduction of Er₂O₃ increased the number of electrochemically active sites and the oxygen vacancies in ErFeO, optimizing the binding energies of adsorption/desorption intermediates during the OER

process. This optimization likely contributed to increased reactivity of the electrocatalyst, thereby enhancing its OER performance. The heterointerface formed between Er_2O_3 and the active component Fe_2O_3 facilitated charge transfer from Er_2O_3 to Fe_2O_3 , promoting efficient electron transport during the OER. Additionally, Er_2O_3 served dual roles as an anchoring site and a protective layer for the active sites during the OER reaction, thereby enhancing the long-term stability of ErFeO by preventing degradation and maintaining the integrity of the electrocatalyst over extended operational periods.

Considering the remarkable OER activity and stability, an overall water splitting experiment was conducted with Pt/C as the cathode and ErFeO as the anode (ErFeO || Pt/C). The polarization curves of overall water splitting, depicted in **Figure 4.16(a)**, revealed that ErFeO || Pt/C achieved a cell voltage of 1.54 V at 10 mA/cm², which was lower than that of RuO₂ || Pt/C (1.56 V). The ErFeO || Pt/C cell demonstrated stability over 30 h of continuous OER operation, as evidenced by the CP result in **Figure 4.16(b)**.

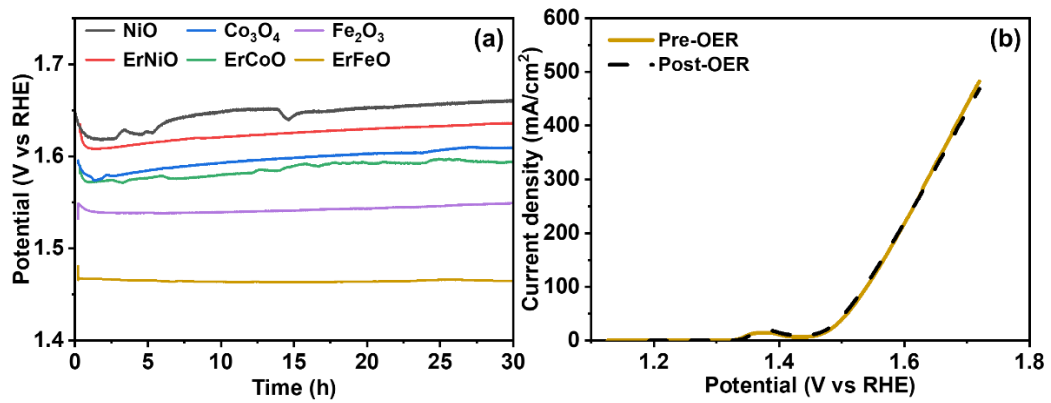


Figure 4.14: (a) Chronopotentiometry of various materials at 10 mA/cm², and (b) LSV curve of ErFeO before and after 30 h of stability testing

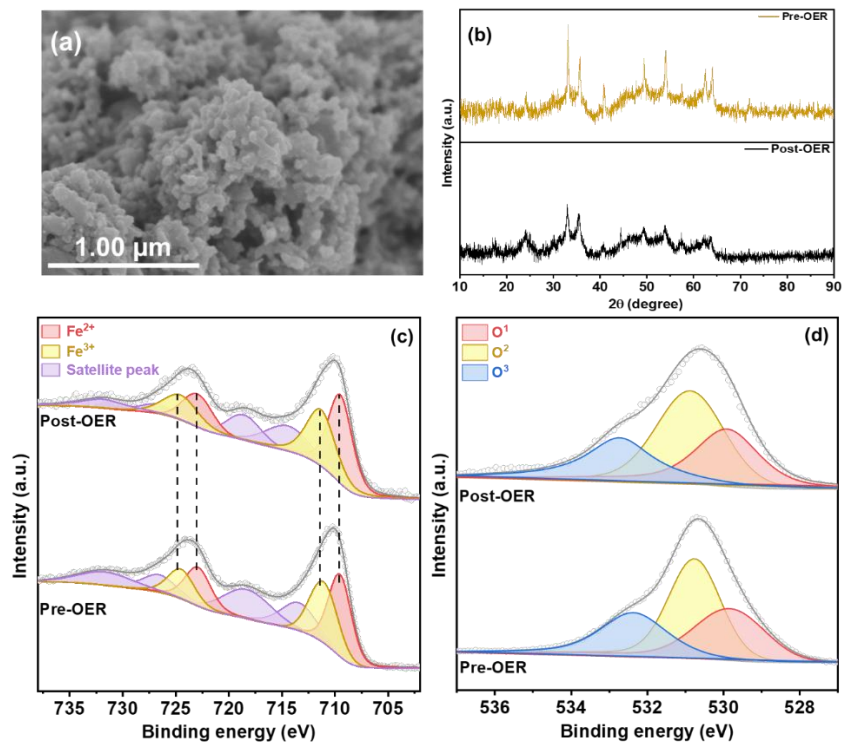


Figure 4.15: (a) FESEM, (b) XRD pattern, and (c) XPS of Fe 2p, and (d) XPS of O 1s of ErFeO before and after OER

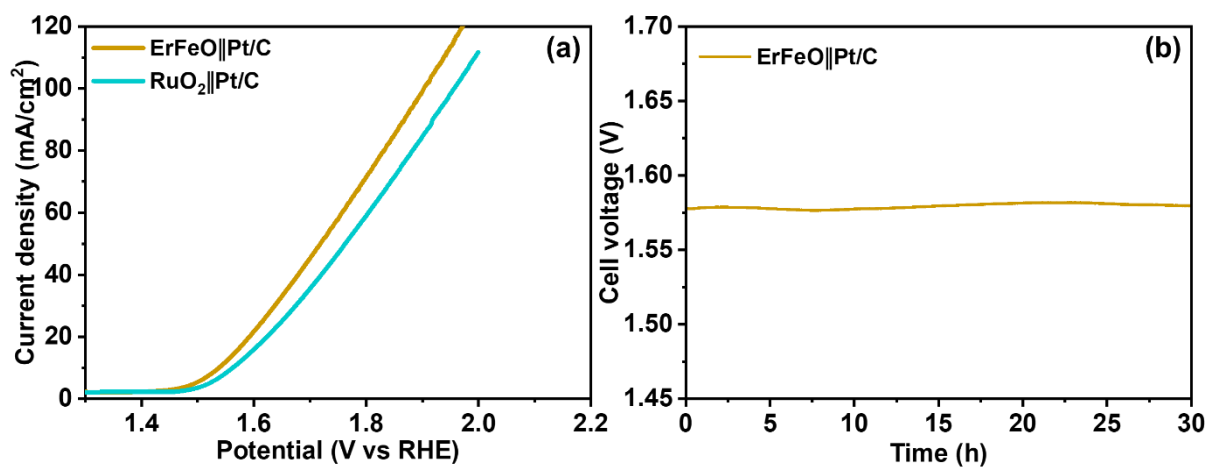


Figure 4.16: (a) LSV curve of two-electrode systems, and (b) CP for overall water splitting at 10 mA/cm² of the ErFeO || Pt/C system

The OER activities of ErFeO were investigated with varying concentrations of Er^{3+} reactant, denoted by ErFeO (x), where $x = 1/1, 1/4, 1/8, 1/12,$ and $1/16$. The η_{10} reached its minimum at ErFeO (1/8), as illustrated in **Figure 4.17(a)**. Furthermore, a higher concentration of Er^{3+} reactant resulted in increased stability during 30 h of OER operation (**Figure 4.17(b)**). As shown in **Figure 4.17(c)**, ErFeO (1/8) displayed only slightly lower activity retention of 99.92% compared to ErFeO (1/1) (99.97%) and ErFeO (1/4) (99.94%). However, the decreased activity of ErFeO (1/12) and (1/16) compared to (1/8) can be attributed to the higher proportion of Fe_2O_3 , leading to the agglomeration of active sites, as indicated by their lower values of C_{dl} (**Figure 4.18(a–c)**). Despite this, their lower R_{ct} enabled them to exhibit higher activity than pristine Fe_2O_3 (**Figure 4.18(d)**). Considering the compromise between overpotential, stability, and the concentration of Er^{3+} reactant, ErFeO (1/8) is a promising electrocatalyst for OER applications.

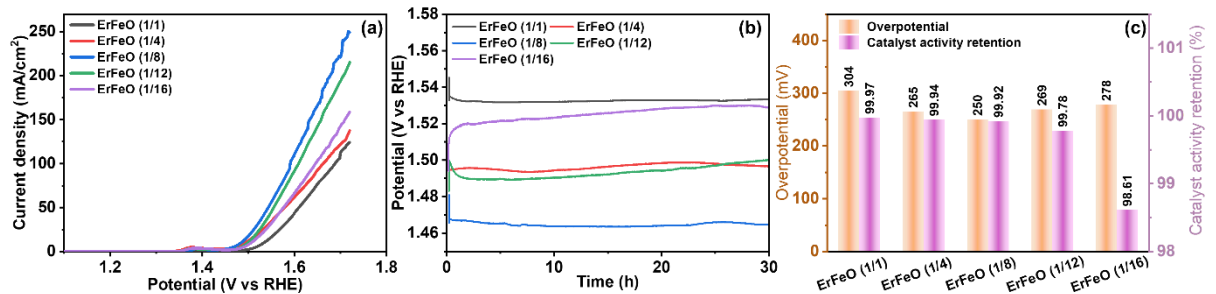


Figure 4.17: (a) LSV curves, (b) Chronopotentiometry at 10 mA/cm², and (c) comparison of activity retention after 30h OER operation and overpotential at 10 mA/cm² of ErFeO (x) (x=1/1, 1/4, 1/8, 1/12, and 1/16)

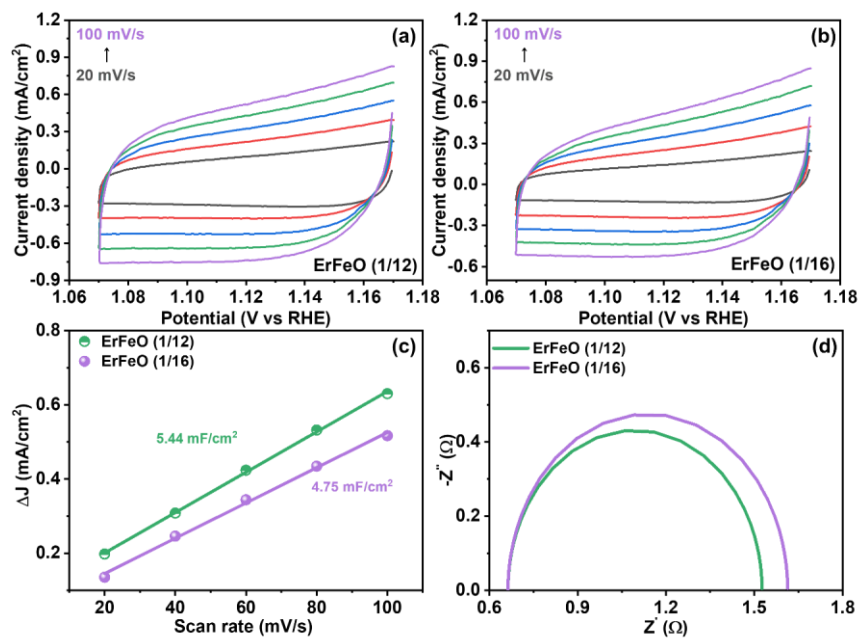


Figure 4.18: (a,b) the cyclic voltammetry in the non-faradaic region of OER, (b) Linear fitting of current density against scan rates, and (d) Nyquist plots of ErFeO (1/12) and (1/16)

4.4. Conclusion

In summary, we successfully introduced Er_2O_3 into various TMOs, including NiO, Co_3O_4 , and Fe_2O_3 , resulting in heterostructure catalysts ErNiO, ErCoO, and ErFeO, respectively. Er_2O_3 acted as an electronic modulator, modifying the electronic structure and creating the heterointerfaces within the heterostructure electrocatalysts. These heterointerfaces functioned as efficient charge transfer pathways, leading to increased reaction rates and enhanced OER performance compared to pristine TMOs. In the case of ErFeO, Er_2O_3 served as a promoter and anchoring site for Fe_2O_3 . This dual functionality yielded an electrocatalyst with the highest specific surface area, characterized by mesoporous structures and abundant oxygen vacancies. The interweaving phenomenon in the structure also contributed to a strong interaction at the heterojunction interface. Consequently, ErFeO exhibited superior activity in the OER process, featuring a low overpotential, a small Tafel slope, a high ECSA, a low R_{ct} , and excellent long-term stability among the synthesized materials.

Part 4. Modifying atomic geometries by phosphate group

Chapter 5. Iron-Tin phosphate electrocatalyst applied for bifunctional water splitting

5.1. Introduction

Investigating an effective electrocatalyst based on transition metal-based material for bifunctional application in water splitting including HER and OER is essential. Because water splitting is an efficient method to produce hydrogen, which is an important energy carrier that can drive energy demand to sustainable and non-emission gas resources [200]. Transition metal-based electrocatalysts offer a promising alternative to noble metal-based materials owing to their low cost and earth abundant elements [178].

Transition metal phosphates material has been investigated as a new group material for electrocatalyst in water splitting [201]. The phosphate group possesses the diversity of atomic geometries enabling the distortion and stabilization of the metal's active oxidation state [201]. Moreover, the phosphate group acts as a proton acceptor which helps in the self-repair of the catalyst and assists in the proton-electron transfer process during metal oxidation [202]. The PO_4^{3-} also can stabilize the local pH environment, which is important for OER process [203]. Furthermore, transition metal phosphates are more likely to exhibit great HER catalytic activity due to their enhanced electrophilicity and can serve as a more powerful electron acceptor during electron transfer process [204].

The compound of tin (Sn) is likely to display an enhanced electrocatalytic activity for water splitting due to its morphological diversity [205] and excellent corrosion resistance in strong alkaline environments [206]. Notably, the covalent bonds between transition metal and Sn result in high electrical conductivity [207].

An iron-tin phosphate electrocatalyst is expected to exhibit an enhanced activity, stability, and cost-effectiveness for bifunctional water splitting. The synthesized materials will be characterized by their features, and their activity for HER and OER will be investigated. The results of this research will contribute to the development of sustainable and efficient hydrogen production systems.

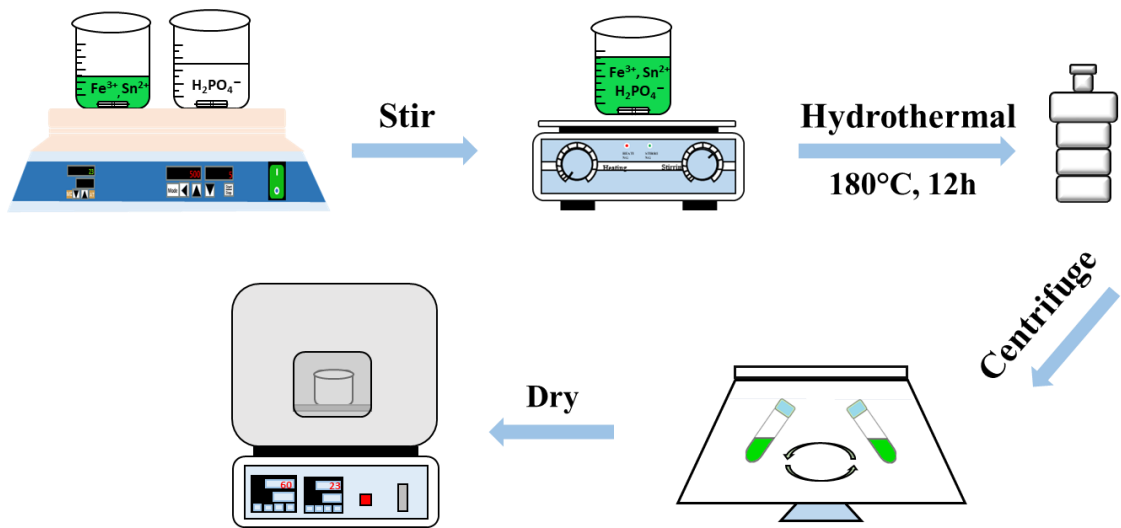
5.2. Objectives

The primary objective of this research is to develop an electrocatalyst using iron-tin phosphate material for bifunctional water splitting with elevated activity, cost-effectiveness, abundant resources, and stability. The proposed electrocatalyst will be designed for a simple synthesis procedure that can be easily scaled up for industrial applications. The study aims to fabricate the electrocatalyst, characterize its features, and investigate its activity for both HER and OER.

5.3. Methodology

5.3.1. Synthesis of Iron-tin Phosphate-Based Electrocatalyst

Iron-tin phosphate electrocatalysts will be synthesized using a simple procedure of hydrothermal method as described in **Scheme 5.1**.



Scheme 5.1: synthesis procedure of iron-tin phosphate

5.3.2. Characterization

X-ray diffraction (XRD), X-ray photoelectron spectroscopy (XPS), Fourier-transform infrared spectroscopy (FTIR), Raman, thermogravimetric analysis (TGA), high-resolution transmission electron microscopy (HRTEM), and field-emission scanning electron microscopy (FESEM) will be employed to elucidate the physicochemical properties of the synthesized materials.

5.3.3. Electrocatalytic Performance Evaluation

The electrocatalytic activity of the synthesized materials for both HER and OER will be assessed through cyclic voltammetry (CV), linear sweep voltammetry (LSV), electrochemical impedance spectroscopy (EIS), determination of Tafel slopes, turnover frequency (TOF) calculations, and chronoamperometry (CA) in a three-electrode electrochemical cell setup. Additionally, a solar flat plate collector integrated with a two-electrode system of iron-tin phosphate will be employed to assess the practical application of this electrocatalyst in water splitting.

5.4. Expected Outcomes

This research is expected to yield valuable insights into the development of iron-Sn phosphate-based electrocatalysts for bifunctional water splitting. The findings will contribute to the development of sustainable and efficient hydrogen production systems.

Part V: Summary

In summary, this dissertation aims to enhance transition metal-based electrocatalysts for water splitting applications based on the key of:

- Minimize overpotential for water splitting reactions.
- Ensure long-term durability of the electrocatalyst.

The approach involves designing heterostructure catalysts that combine two or more components to leverage synergistic effects and overcome individual disadvantages. Thanks to interfaces interaction of the components, electronic structures and strain materials can be modified to enhance suitability for water splitting applications.

Depositing the active component catalyst onto supported two-dimensional (2D) materials proves to be an effective strategy for improving activity and stability. While siloxene has been predominantly investigated for applications such as supercapacitors, photocatalysts, and Li-ion batteries, its application in water splitting is relatively new. When employed as the support for NiO/Co₃O₄, siloxene served as a reducing agent, a surfactant for controlling the size of bimetallic oxides, and a support for HER. Notably, there was a migration phenomenon observed, wherein absorbed hydrogen from active sites (bimetallic oxides) migrates to the support (siloxene), facilitating the easy release of hydrogen gas. Additionally, among three of 2D support of reduced graphene oxide (rGO), graphitic carbon nitride (gC₃N₄), and siloxene (SiSh), rGO was an effective support for CoMoO₄/CoS/MoS₂ (CMSO) in OER process. The high specific surface area and the abundance functional group of rGO facilitated more active sites to expose, increasing electrochemically active surface area of CMSO@rGO. Consequently, it exhibited the highest performance in OER among synthesized materials, even the benchmark material RuO₂.

Furthermore, the electronic structure of transition metal oxides is significantly influenced by the introduction of rare earth element oxides. Incorporating Er₂O₃ into NiO, Co₃O₄, and Fe₂O₃ enhances their conductivity and specific surface area, resulting in improved OER performance. Particularly, ErFeO exhibits superior activity and stability compared to benchmark materials like RuO₂.

Finally, the dissertation proposes an approach to enhance the activity of transition metal-based electrocatalysts by modifying atomic geometries. Compounds containing phosphates offer various atomic geometries, allowing for flexible coordination that stabilizes the active oxidation state of transition metals and facilitates favorable adsorption and oxidation of water molecules.

This research provides valuable enlightenment for the development of a cost-effective, abundant resource, reducing dependence on noble metal-based electrocatalysts, contributes to advancing the feasibility and scalability of green hydrogen technologies.

Part VI: Recommendations for future work

Transition metal-based electrocatalyst exhibited the high activity, low cost, earth-abundance materials in water splitting application. Thus, improving and developing these materials to alter noble metal-based materials for water splitting, as well as the hydrogen production is necessary in the future. Based on the findings of this dissertation, several recommendations for future research can be proposed:

First, transition metal-based electrocatalysts have demonstrated promising activity in basic conditions, but their stability under practical conditions needs improvement. Future research should focus on developing strategies to enhance the stability of these materials when exposed to acidic or alkaline electrolytes, high temperatures, and high current densities.

Second, exploring the new support materials beyond those investigated in this dissertation. Novel materials with unique properties, such as high surface area, tunable pore structure, and enhanced conductivity, could further enhance the performance of transition metal-based electrocatalysts..

Third, utilizing in-situ instrument characterization techniques can provide valuable insights into the mechanisms of HER and OER. By elucidating the reaction pathways and surface interactions, researchers can identify key factors influencing catalytic activity and develop strategies to optimize performance. Integrating advanced characterization techniques into future studies will enhance our understanding of transition metal-based electrocatalysts..

Fourth, investigating alternative synthesis methods offer opportunities to tailor the properties of transition metal-based electrocatalysts, particularly, the atomic layer deposition is one of the promising technique for synthesizing catalyst materials with precise control over composition, morphology, and surface structure.

Finally, integrating water splitting systems with renewable energy sources such as solar or wind power. By leveraging renewable energies, hydrogen production processes can become more environmentally friendly and economically viable. Investigating novel integration strategies and optimizing system design will be essential for advancing the development of sustainable hydrogen production technologies.

References

1. IEA (2011), W.E.O., IEA, Paris <https://www.iea.org/reports/world-energy-outlook-2011>, Licence: CC BY 4.0.
2. Bauer, N., et al., *Shared Socio-Economic Pathways of the Energy Sector – Quantifying the Narratives*. Global Environmental Change, 2017. **42**: p. 316-330.
3. Ang, T.-Z., et al., *A comprehensive study of renewable energy sources: Classifications, challenges and suggestions*. Energy Strategy Reviews, 2022. **43**: p. 100939.
4. energy, O.o.e.e.r. *Hydrogen storage*. Available from: <https://www.energy.gov/eere/fuelcells/hydrogen-storage#:~:text=On%20a%20volume%20basis%2C%20however,based%20on%20lower%20heating%20values>.
5. Niaz, S., T. Manzoor, and A.H. Pandith, *Hydrogen storage: Materials, methods and perspectives*. Renewable and Sustainable Energy Reviews, 2015. **50**: p. 457-469.
6. Dincer, I. and M.A. Rosen, *Exergy as a Driver for Achieving Sustainability*. International Journal of Green Energy, 2004. **1**(1): p. 1-19.
7. energy, O.o.e.e.r.; Available from: <https://www.energy.gov/eere/fuelcells/h2scale>.
8. Pathak, P.K., A.K. Yadav, and S. Padmanaban, *Transition toward emission-free energy systems by 2050: Potential role of hydrogen*. International Journal of Hydrogen Energy, 2023. **48**(26): p. 9921-9927.
9. "What is hydrogen and how is it made?" *The World of Hydrogen*. Available from: <https://www.theworldofhydrogen.com/gasunie/what-is-hydrogen/>.
10. Xu, Y., et al., *Recent advances in electrocatalysts for neutral and large-current-density water electrolysis*. Nano Energy, 2021. **80**: p. 105545.
11. Zhu, J., et al., *Recent Advances in Electrocatalytic Hydrogen Evolution Using Nanoparticles*. Chemical Reviews, 2020. **120**(2): p. 851-918.
12. Parsons, R., *The rate of electrolytic hydrogen evolution and the heat of adsorption of hydrogen*. Transactions of the Faraday Society, 1958. **54**(0): p. 1053-1063.
13. Cao, X., et al., *Research progress on MOFs and their derivatives as promising and efficient electrode materials for electrocatalytic hydrogen production from water*. RSC Advances, 2023. **13**(35): p. 24393-24411.
14. Wang, S., A. Lu, and C.-J. Zhong, *Hydrogen production from water electrolysis: role of catalysts*. Nano Convergence, 2021. **8**(1): p. 4.
15. Huynh, N.-D., W.M. Choi, and S.H. Hur, *Exploring the Effects of Various Two-Dimensional Supporting Materials on the Water Electrolysis of Co-Mo Sulfide/Oxide Heterostructure*. Nanomaterials, 2023. **13**(17).
16. Wang, B., et al., *A Nanosized CoNi Hydroxide@Hydroxysulfide Core-Shell Heterostructure for Enhanced Oxygen Evolution*. Advanced Materials, 2019. **31**(4): p. 1805658.
17. Fei, B., et al., *Anion-cation co-substitution activation of spinel CoMoO₄ for efficient oxygen evolution reaction*. Chemical Engineering Journal, 2020. **394**: p. 124926.

18. Liu, X., et al., *Recent Advances in the Comprehension and Regulation of Lattice Oxygen Oxidation Mechanism in Oxygen Evolution Reaction*. Transactions of Tianjin University, 2023. **29**(4): p. 247-253.
19. Man, I.C., et al., *Universality in Oxygen Evolution Electrocatalysis on Oxide Surfaces*. ChemCatChem, 2011. **3**(7): p. 1159-1165.
20. McCrory, C.C.L., et al., *Benchmarking Heterogeneous Electrocatalysts for the Oxygen Evolution Reaction*. Journal of the American Chemical Society, 2013. **135**(45): p. 16977-16987.
21. Yu, J., et al., *Recent Advances and Prospective in Ruthenium-Based Materials for Electrochemical Water Splitting*. ACS Catalysis, 2019. **9**(11): p. 9973-10011.
22. Langhus, D.L., *Fundamentals of Electroanalytical Chemistry (Monk, Paul M. S.)*. Journal of Chemical Education, 2002. **79**(10): p. 1207.
23. Lazanas, A.C. and M.I. Prodromidis, *Electrochemical Impedance Spectroscopy—A Tutorial*. ACS Measurement Science Au, 2023. **3**(3): p. 162-193.
24. Anantharaj, S., P.E. Karthik, and S. Noda, *The Significance of Properly Reporting Turnover Frequency in Electrocatalysis Research*. Angewandte Chemie International Edition, 2021. **60**(43): p. 23051-23067.
25. Vazhayil, A., et al., *A comprehensive review on the recent developments in transition metal-based electrocatalysts for oxygen evolution reaction*. Applied Surface Science Advances, 2021. **6**: p. 100184.
26. Sekar, S., et al., *One-step facile hydrothermal synthesis of rGO-CoS₂ nanocomposites for high performance HER electrocatalysts*. International Journal of Hydrogen Energy, 2022. **47**(95): p. 40359-40367.
27. Yang, J., et al., *Fe₃O₄-Decorated Co₉S₈ Nanoparticles In Situ Grown on Reduced Graphene Oxide: A New and Efficient Electrocatalyst for Oxygen Evolution Reaction*. Advanced Functional Materials, 2016. **26**(26): p. 4712-4721.
28. He, X., et al., *Tuning Electronic Structure of CuCo₂O₄ Spinel via Mn-Doping for Enhancing Oxygen Evolution Reaction*. ChemElectroChem, 2023. **10**(2): p. e202200933.
29. Cui, B., et al., *Core–Ring Structured NiCo₂O₄ Nanoplatelets: Synthesis, Characterization, and Electrocatalytic Applications*. Advanced Functional Materials, 2008. **18**(9): p. 1440-1447.
30. Chen, J., et al., *Shape-controlled synthesis of platinum nanocrystals for catalytic and electrocatalytic applications*. Nano Today, 2009. **4**(1): p. 81-95.
31. Paoli, E.A., et al., *Oxygen evolution on well-characterized mass-selected Ru and RuO₂ nanoparticles*. Chemical Science, 2015. **6**(1): p. 190-196.
32. Zhang, Z., et al., *An overview of metal oxide materials as electrocatalysts and supports for polymer electrolyte fuel cells*. Energy & Environmental Science, 2014. **7**(8): p. 2535-2558.
33. Han, X., et al., *Engineering Catalytic Active Sites on Cobalt Oxide Surface for Enhanced Oxygen Electrocatalysis*. Advanced Energy Materials, 2018. **8**(10): p. 1702222.

34. Li, R., et al., *The urchin-like sphere arrays Co₃O₄ as a bifunctional catalyst for hydrogen evolution reaction and oxygen evolution reaction*. Journal of Power Sources, 2017. **341**: p. 250-256.
35. Yan, D., et al., *Engineering the electronic structure of Co₃O₄ by carbon-doping for efficient overall water splitting*. Electrochimica Acta, 2019. **303**: p. 316-322.
36. Du, J., C. Li, and Q. Tang, *Oxygen vacancies enriched Co₃O₄ nanoflowers with single layer porous structures for water splitting*. Electrochimica Acta, 2020. **331**: p. 135456.
37. Manjunath, V., et al., *Experimental investigations on morphology controlled bifunctional NiO nano-electrocatalysts for oxygen and hydrogen evolution*. International Journal of Hydrogen Energy, 2022. **47**(92): p. 39018-39029.
38. Fominykh, K., et al., *Iron-Doped Nickel Oxide Nanocrystals as Highly Efficient Electrocatalysts for Alkaline Water Splitting*. ACS Nano, 2015. **9**(5): p. 5180-5188.
39. Samanta, A. and S. Jana, *Ni-, Co-, and Mn-Doped Fe₂O₃ Nano-Parallelepipedes for Oxygen Evolution*. ACS Applied Nano Materials, 2021. **4**(5): p. 5131-5140.
40. Xu, Q.-Q., et al., *Crystal phase determined Fe active sites on Fe₂O₃ (γ - and α -Fe₂O₃) yolk-shell microspheres and their phase dependent electrocatalytic oxygen evolution reaction*. Applied Surface Science, 2020. **533**: p. 147368.
41. Mahmood, N., et al., *Electrocatalysts for Hydrogen Evolution in Alkaline Electrolytes: Mechanisms, Challenges, and Prospective Solutions*. Advanced Science, 2018. **5**(2): p. 1700464.
42. Hu, C., L. Zhang, and J. Gong, *Recent progress made in the mechanism comprehension and design of electrocatalysts for alkaline water splitting*. Energy & Environmental Science, 2019. **12**(9): p. 2620-2645.
43. Deiman, P.v.T.a., J. R. *Sur une manière de décomposer l'Eau en Air inflammable et en Air vital*. Obs Phys, 1789. **35**, **369–378**.
44. McCrory, C.C.L., et al., *Benchmarking Hydrogen Evolving Reaction and Oxygen Evolving Reaction Electrocatalysts for Solar Water Splitting Devices*. Journal of the American Chemical Society, 2015. **137**(13): p. 4347-4357.
45. Shifa, T.A., et al., *Heterostructures Based on 2D Materials: A Versatile Platform for Efficient Catalysis*. Advanced Materials, 2019. **31**(45): p. 1804828.
46. Xu, W., et al., *Heterogeneous Synergetic Effect of Metal–Oxide Interfaces for Efficient Hydrogen Evolution in Alkaline Solutions*. ACS Applied Materials & Interfaces, 2021. **13**(11): p. 13838-13847.
47. Zhai, P., et al., *Engineering active sites on hierarchical transition bimetal oxides/sulfides heterostructure array enabling robust overall water splitting*. Nature Communications, 2020. **11**(1): p. 5462.
48. Wu, H., et al., *Non-noble Metal Electrocatalysts for the Hydrogen Evolution Reaction in Water Electrolysis*. Electrochemical Energy Reviews, 2021. **4**(3): p. 473-507.
49. Paul, R., et al., *Ten years of carbon-based metal-free electrocatalysts*. Carbon Energy, 2019. **1**(1): p. 19-31.
50. Knani, S., et al., *2 - Metal oxide-based electrocatalysts for low-temperature electrochemical production and oxidation of hydrogen (HER and HOR)*, in *Metal Oxide-Based Nanostructured Electrocatalysts for Fuel Cells, Electrolyzers, and Metal-air Batteries*, T.W. Napporn and Y. Holade, Editors. 2021, Elsevier. p. 9-35.

51. Mohan Kumar, G., et al., *Co-Ni based hybrid transition metal oxide nanostructures for cost-effective bi-functional electrocatalytic oxygen and hydrogen evolution reactions*. International Journal of Hydrogen Energy, 2020. **45**(1): p. 391-400.
52. QayoomMugheri, A., et al., *Co₃O₄/ NiO bifunctional electrocatalyst for water splitting*. Electrochimica Acta, 2019. **306**: p. 9-17.
53. Qazi, U.Y., et al., *Bimetallic NiCo–NiCoO₂ nano-heterostructures embedded on copper foam as a self-supported bifunctional electrode for water oxidation and hydrogen production in alkaline media*. International Journal of Hydrogen Energy, 2021. **46**(36): p. 18936-18948.
54. Elakkiya, R., R. Ramkumar, and G. Maduraiveeran, *Flower-like nickel-cobalt oxide nanomaterials as bi-functional catalyst for electrochemical water splitting*. Materials Research Bulletin, 2019. **116**: p. 98-105.
55. Wei, X., et al., *Carbon-incorporated NiO/Co₃O₄ concave surface microcubes derived from a MOF precursor for overall water splitting*. Chemical Communications, 2019. **55**(46): p. 6515-6518.
56. Gong, S., et al., *O species-decorated graphene shell encapsulating iridium–nickel alloy as an efficient electrocatalyst towards hydrogen evolution reaction*. Journal of Materials Chemistry A, 2019. **7**(25): p. 15079-15088.
57. Zitolo, A., et al., *Identification of catalytic sites for oxygen reduction in iron- and nitrogen-doped graphene materials*. Nature Materials, 2015. **14**(9): p. 937-942.
58. Wöhler, F., *Ueber Verbindungen des Siliciums mit Sauerstoff und Wasserstoff*. Justus Liebigs Annalen der Chemie, 1863. **127**(3): p. 257-274.
59. Weiss, A., G. Beil, and H. Meyer, *The Topochemical Reaction of CaSi₂ to a Two-Dimensional Subsiliceous Acid Si₆H₃(OH)₃ (= Kautsky's Siloxene)*. Zeitschrift für Naturforschung B, 1980. **35**(1): p. 25-30.
60. Kautsky, H., W. Vogell, and F. Oeters, *Notizen: Die Bedeutung elektronenmikroskopischer Untersuchungen für die Konstitutions- und Strukturaufklärung des Siloxens*. Zeitschrift für Naturforschung B, 1955. **10**(10): p. 597-598.
61. Yamanaka, S., H. Matsu-ura, and M. Ishikawa, *New deintercalation reaction of calcium from calcium disilicide. Synthesis of layered polysilane*. Materials Research Bulletin, 1996. **31**(3): p. 307-316.
62. Meng, Q., et al., *Siloxene-reduced graphene oxide composite hydrogel for supercapacitors*. Chemical Engineering Journal, 2020. **393**: p. 124684.
63. Kang, H.J., et al., *A visible-light-sensitive siloxene-based composite material with enhanced photocatalytic activity*. Journal of Photochemistry and Photobiology A: Chemistry, 2018. **365**: p. 32-38.
64. Fu, R., et al., *Two-dimensional silicon suboxides nanostructures with Si nanodomains confined in amorphous SiO₂ derived from siloxene as high performance anode for Li-ion batteries*. Nano Energy, 2017. **39**: p. 546-553.
65. Dai, Q., et al., *Spontaneous deposition of Ir nanoparticles on 2D siloxene as a high-performance HER electrocatalyst with ultra-low Ir loading*. Chemical Communications, 2020. **56**(35): p. 4824-4827.

66. Ryan, B.J., et al., *Silicene, Siloxene, or Silicane? Revealing the Structure and Optical Properties of Silicon Nanosheets Derived from Calcium Disilicide*. *Chemistry of Materials*, 2020. **32**(2): p. 795-804.
67. Raja, V., S.K. Puvaneswaran, and K. Swaminathan, *Unique and hierarchically structured novel Co₃O₄/NiO nanosponges with superior photocatalytic activity against organic contaminants*. *Frontiers of Materials Science*, 2017. **11**(4): p. 375-384.
68. Douglas A. Skoog, F.J.H., Stanley R., *Principles of Instrumental Analysis*. 2007. **Chapter 18** p. 492.
69. Huang, Y., Z. Jiang, and W. Schwieger, *Vibrational Spectroscopic Studies of Layered Silicates*. *Chemistry of Materials*, 1999. **11**(5): p. 1210-1217.
70. Diallo, A., et al., *Green synthesis of Co₃O₄ nanoparticles via *Aspalathus linearis*: Physical properties*. *Green Chemistry Letters and Reviews*, 2015. **8**(3-4): p. 30-36.
71. Zhao, B., et al., *Monolayer graphene/NiO nanosheets with two-dimension structure for supercapacitors*. *Journal of Materials Chemistry*, 2011. **21**(46): p. 18792-18798.
72. Deepak, N., et al., *Siloxene: A novel 2D photocatalyst for degradation of dye molecules*. *Nano-Structures & Nano-Objects*, 2021. **26**: p. 100721.
73. Suresh, S. and J. Podder, *Investigations on structural, optical, morphological and electrical properties of nickel oxide nanoparticles*. *International Journal of Nanoparticles*, 2015. **Vol. 8**: p. 289-301.
74. Dong, C., et al., *Hydrothermal synthesis of Co₃O₄ nanorods on nickel foil*. *Materials Letters*, 2014. **123**: p. 187-190.
75. Brunauer, S., P.H. Emmett, and E. Teller, *Adsorption of Gases in Multimolecular Layers*. *Journal of the American Chemical Society*, 1938. **60**(2): p. 309-319.
76. Tang, X., et al., *The effect of the variation in material composition on the heterogeneous pore structure of high-maturity shale of the Silurian Longmaxi formation in the southeastern Sichuan Basin, China*. *Journal of Natural Gas Science and Engineering*, 2015. **23**: p. 464-473.
77. Fleischmann, S., A. Tolosa, and V. Presser, *Design of Carbon/Metal Oxide Hybrids for Electrochemical Energy Storage*. *Chemistry – A European Journal*, 2018. **24**(47): p. 12143-12153.
78. Mukhopadhyay, T., et al., *Effective mechanical properties of multilayer nano-heterostructures*. *Scientific Reports*, 2017. **7**(1): p. 15818.
79. Srivastava, N. and P.C. Srivastava, *Realizing NiO nanocrystals from a simple chemical method*. *Bulletin of Materials Science*, 2010. **33**(6): p. 653-656.
80. Choi, M., J.-C. Kim, and D.-W. Kim, *Waste Windshield-Derived Silicon/Carbon Nanocomposites as High-Performance Lithium-Ion Battery Anodes*. *Scientific Reports*, 2018. **8**(1): p. 960.
81. Guan, C., et al., *Hollow Co₃O₄ Nanosphere Embedded in Carbon Arrays for Stable and Flexible Solid-State Zinc–Air Batteries*. *Advanced Materials*, 2017. **29**(44): p. 1704117.
82. Yan, X., et al., *Nickel@Siloxene catalytic nanosheets for high-performance CO₂ methanation*. *Nature Communications*, 2019. **10**(1): p. 2608.

83. Chen, X., et al., *Synthesis of “Clean” and Well-Dispersive Pd Nanoparticles with Excellent Electrocatalytic Property on Graphene Oxide*. Journal of the American Chemical Society, 2011. **133**(11): p. 3693-3695.
84. Zhang, W., et al., *Lithiation/Delithiation Synthesis of Few Layer Silicene Nanosheets for Rechargeable Li–O₂ Batteries*. Advanced Materials, 2018. **30**(15): p. 1705523.
85. Lamiel, C., et al., *Microwave-assisted binder-free synthesis of 3D Ni-Co-Mn oxide nanoflakes@Ni foam electrode for supercapacitor applications*. Chemical Engineering Journal, 2017. **316**: p. 1091-1102.
86. Zhang, Y., et al., *Influence of Magnesia on Demoulding Strength of Colloidal Silica-Bonded Castables*. REVIEWS ON ADVANCED MATERIALS SCIENCE, 2019. **58**(1): p. 32-37.
87. Turner, N.H. and A.M. Single, *Determination of peak positions and areas from wide-scan XPS spectra*. Surface and Interface Analysis, 1990. **15**(3): p. 215-222.
88. Tyuliev, G. and S. Angelov, *The nature of excess oxygen in Co₃O₄+ε*. Applied Surface Science, 1988. **32**(4): p. 381-391.
89. Haber, J. and L. Ungier, *On chemical shifts of ESCA and Auger lines in cobalt oxides*. Journal of Electron Spectroscopy and Related Phenomena, 1977. **12**(3): p. 305-312.
90. Hessels, J., et al., *Potential- and Buffer-Dependent Catalyst Decomposition during Nickel-Based Water Oxidation Catalysis*. ChemSusChem, 2020. **13**(21): p. 5625-5631.
91. Liu, H., et al., *Superior Hydrogen Sensing Property of Porous NiO/SnO(2) Nanofibers Synthesized via Carbonization*. Nanomaterials (Basel), 2019. **9**(9).
92. Okamoto, Y., T. Imanaka, and S. Teranishi, *Surface structure of CoO · MoO₃Al₂O₃ catalysts studied by X-ray photoelectron spectroscopy*. Journal of Catalysis, 1980. **65**(2): p. 448-460.
93. Haber, J., J. Stoch, and L. Ungier, *X-ray photoelectron spectra of oxygen in oxides of Co, Ni, Fe and Zn*. Journal of Electron Spectroscopy and Related Phenomena, 1976. **9**(5): p. 459-467.
94. Morales-Guio, C.G., L.-A. Stern, and X. Hu, *Nanostructured hydrotreating catalysts for electrochemical hydrogen evolution*. Chemical Society Reviews, 2014. **43**(18): p. 6555-6569.
95. Shinagawa, T., A.T. Garcia-Esparza, and K. Takahashi, *Insight on Tafel slopes from a microkinetic analysis of aqueous electrocatalysis for energy conversion*. Scientific Reports, 2015. **5**(1): p. 13801.
96. Zhang, B., et al., *Interface engineering: The Ni(OH)₂/MoS₂ heterostructure for highly efficient alkaline hydrogen evolution*. Nano Energy, 2017. **37**: p. 74-80.
97. Liu, J., et al., *Mutually beneficial Co₃O₄@MoS₂ heterostructures as a highly efficient bifunctional catalyst for electrochemical overall water splitting*. Journal of Materials Chemistry A, 2018. **6**(5): p. 2067-2072.
98. Xu, Y.-F., et al., *Nickel/Nickel(II) Oxide Nanoparticles Anchored onto Cobalt(IV) Diselenide Nanobelts for the Electrochemical Production of Hydrogen*. Angewandte Chemie International Edition, 2013. **52**(33): p. 8546-8550.
99. Bai, Y., et al., *Engineering the surface charge states of nanostructures for enhanced catalytic performance*. Materials Chemistry Frontiers, 2017. **1**(10): p. 1951-1964.

100. Qiu, J., et al., *NiO/Co₃O₄ nanoheterostructure derived from nickelocene filled ZIF-67 for supercapacitors*. Journal of Alloys and Compounds, 2018. **763**: p. 966-974.
101. Zhu, L., et al., *A rhodium/silicon co-electrocatalyst design concept to surpass platinum hydrogen evolution activity at high overpotentials*. Nature Communications, 2016. **7**(1): p. 12272.
102. Sheng, M., et al., *Approaching the Volcano Top: Iridium/Silicon Nanocomposites as Efficient Electrocatalysts for the Hydrogen Evolution Reaction*. ACS Nano, 2019. **13**(3): p. 2786-2794.
103. Lian, K., S.J. Thorpe, and D.W. Kirk, *Electrochemical and surface characterization of electrocatalytically active amorphous Ni-Co alloys*. Electrochimica Acta, 1992. **37**(11): p. 2029-2041.
104. Mansour, A.N. and C.A. Melendres, *Characterization of α -Ni(OH)₂ by XPS*. Surface Science Spectra, 1994. **3**(3): p. 255-262.
105. McIntyre, N.S. and M.G. Cook, *X-ray photoelectron studies on some oxides and hydroxides of cobalt, nickel, and copper*. Analytical Chemistry, 1975. **47**(13): p. 2208-2213.
106. Tan, B.J., K.J. Klabunde, and P.M.A. Sherwood, *XPS studies of solvated metal atom dispersed (SMAD) catalysts. Evidence for layered cobalt-manganese particles on alumina and silica*. Journal of the American Chemical Society, 1991. **113**(3): p. 855-861.
107. Mrabet, C., et al., *Physical properties of La-doped NiO sprayed thin films for optoelectronic and sensor applications*. Ceramics International, 2016. **42**(5): p. 5963-5978.
108. Rivas-Murias, B. and V. Salgueiriño, *Thermodynamic CoO-Co₃O₄ crossover using Raman spectroscopy in magnetic octahedron-shaped nanocrystals*. Journal of Raman Spectroscopy, 2017. **48**(6): p. 837-841.
109. Mondal, A., et al., *NiO hollow microspheres as efficient bifunctional electrocatalysts for Overall Water-Splitting*. International Journal of Hydrogen Energy, 2018. **43**(47): p. 21665-21674.
110. Yan, X., et al., *From Water Oxidation to Reduction: Transformation from Ni_xCo_{3-x}O₄ Nanowires to NiCo/NiCoO_x Heterostructures*. ACS Applied Materials & Interfaces, 2016. **8**(5): p. 3208-3214.
111. Xia, K., et al., *Targeted Assembly of Ultrathin NiO/MoS₂ Electrodes for Electrocatalytic Hydrogen Evolution in Alkaline Electrolyte*. Nanomaterials, 2020. **10**(8).
112. Jo, S.G., et al., *Phase-Controlled NiO Nanoparticles on Reduced Graphene Oxide as Electrocatalysts for Overall Water Splitting*. Nanomaterials, 2021. **11**(12).
113. Jiang, J., et al., *Highly efficient hydrogen evolution reaction of Co₃O₄ supports on N-doped carbon nanotubes in an alkaline solution*. Ionics, 2020. **26**(7): p. 3437-3446.
114. Li, Y., et al., *3D self-supported FeOP film on nickel foam as a highly active bifunctional electrocatalyst for urea-assisted overall water splitting*. Materials Research Bulletin, 2018. **100**: p. 72-75.

115. Van Phuc, T., et al., *Highly active Ni/Co-metal organic framework bifunctional electrocatalyst for water splitting reaction*. International Journal of Hydrogen Energy, 2022. **47**(54): p. 22787-22795.
116. Tan, X., et al., *Core-shell structured MoS₂/Ni₉S₈ electrocatalysts for high performance hydrogen and oxygen evolution reactions*. Materials Research Bulletin, 2022. **146**: p. 111626.
117. Yue, M., et al., *Hydrogen energy systems: A critical review of technologies, applications, trends and challenges*. Renewable and Sustainable Energy Reviews, 2021. **146**: p. 111180.
118. Xie, X., et al., *Oxygen Evolution Reaction in Alkaline Environment: Material Challenges and Solutions*. Advanced Functional Materials, 2022. **32**(21): p. 2110036.
119. Xu, X., et al., *High-Performance Perovskite Composite Electrocatalysts Enabled by Controllable Interface Engineering*. Small, 2021. **17**(29): p. 2101573.
120. Fei, L., et al., *Understanding the bifunctional catalytic ability of electrocatalysts for oxygen evolution reaction and urea oxidation Reaction: Recent advances and perspectives*. Chemical Engineering Journal, 2023. **471**: p. 144660.
121. Van Phuc, T., et al., *Highly CO selective Ca and Zn hybrid metal-organic framework electrocatalyst for the electrochemical reduction of CO₂*. Current Applied Physics, 2021. **27**: p. 31-37.
122. Jana, J., et al., *Nano-Dimensional Carbon Nanosphere Supported Non-Precious Metal Oxide Composite: A Cathode Material for Sea Water Reduction*. Nanomaterials, 2022. **12**(23): p. 4348.
123. Park, H., et al., *Enhanced Electrochemical Properties and OER Performances by Cu Substitution in NiCo₂O₄ Spinel Structure*. Nanomaterials, 2020. **10**(9): p. 1727.
124. Jiao, Y., et al., *Design of electrocatalysts for oxygen- and hydrogen-involving energy conversion reactions*. Chemical Society Reviews, 2015. **44**(8): p. 2060-2086.
125. Hong, W.T., et al., *Toward the rational design of non-precious transition metal oxides for oxygen electrocatalysis*. Energy & Environmental Science, 2015. **8**(5): p. 1404-1427.
126. Yu, M.Q., L.X. Jiang, and H.G. Yang, *Ultrathin nanosheets constructed CoMoO₄ porous flowers with high activity for electrocatalytic oxygen evolution*. Chemical Communications, 2015. **51**(76): p. 14361-14364.
127. Fang, L., et al., *Hierarchical CoMoO₄ nanoneedle electrodes for advanced supercapacitors and electrocatalytic oxygen evolution*. Electrochimica Acta, 2018. **259**: p. 552-558.
128. Xun, S., et al., *MOF-derived cobalt oxides nanoparticles anchored on CoMoO₄ as a highly active electrocatalyst for oxygen evolution reaction*. Journal of Alloys and Compounds, 2019. **806**: p. 1097-1104.
129. Hu, Y., et al., *Understanding the sulphur-oxygen exchange process of metal sulphides prior to oxygen evolution reaction*. Nature Communications, 2023. **14**(1): p. 1949.
130. Deng, D., et al., *Catalysis with two-dimensional materials and their heterostructures*. Nature Nanotechnology, 2016. **11**(3): p. 218-230.
131. Novoselov, K.S., et al., *Two-dimensional gas of massless Dirac fermions in graphene*. Nature, 2005. **438**(7065): p. 197-200.

132. Zulqarnain, M., et al., *FeCoSe₂ Nanoparticles Embedded in g-C₃N₄: A Highly Active and Stable bifunctional electrocatalyst for overall water splitting*. Scientific Reports, 2020. **10**(1): p. 6328.
133. Jana, J., et al., *Improved kinetics of reduction of alkaline water on the g-CN-supported transition metal oxide/boride hetero-interface: A case study*. International Journal of Energy Research, 2022. **46**(11): p. 14979-14993.
134. Huynh, N.-D., et al., *2D siloxene supported NiO/Co₃O₄ electrocatalyst for the stable and efficient hydrogen evolution reaction*. Current Applied Physics, 2022. **44**: p. 102-109.
135. Ngo, Y.-L.T. and S.H. Hur, *Low-temperature NO₂ gas sensor fabricated with NiO and reduced graphene oxide hybrid structure*. Materials Research Bulletin, 2016. **84**: p. 168-176.
136. Hasmin, H.F., C. Imawan, and V. Fauzia, *The Role of Temperature in the Hydrothermal Synthesis on the Structural and Morphological Properties of MoS₂*. Journal of Physics: Conference Series, 2021. **1951**(1): p. 012014.
137. Yu, H., et al., *Hierarchically porous three-dimensional electrodes of CoMoO₄ and ZnCo₂O₄ and their high anode performance for lithium ion batteries*. Nanoscale, 2014. **6**(18): p. 10556-10561.
138. Ma, D., et al., *Highly active nanostructured CoS₂/CoS heterojunction electrocatalysts for aqueous polysulfide/iodide redox flow batteries*. Nature Communications, 2019. **10**(1): p. 3367.
139. Xiao, H., et al., *Excess Activity Tuned by Distorted Tetrahedron in CoMoO₄ for Oxygen Evolution*. ENERGY & ENVIRONMENTAL MATERIALS, 2022. **n/a**(n/a): p. e12495.
140. Wei, W., K. Sun, and Y.H. Hu, *An efficient counter electrode material for dye-sensitized solar cells—flower-structured 1T metallic phase MoS₂*. Journal of Materials Chemistry A, 2016. **4**(32): p. 12398-12401.
141. Liu, Y.-R., et al., *In situ sulfurized CoMoS/CoMoO₄ shell–core nanorods supported on N-doped reduced graphene oxide (NRGO) as efficient electrocatalyst for hydrogen evolution reaction*. Journal of Materials Chemistry A, 2017. **5**(6): p. 2885-2896.
142. Yang, Y., et al., *Hierarchical Nanoassembly of MoS₂/Co₉S₈/Ni₃S₂/Ni as a Highly Efficient Electrocatalyst for Overall Water Splitting in a Wide pH Range*. Journal of the American Chemical Society, 2019. **141**(26): p. 10417-10430.
143. McIntyre, N.S., et al., *X-ray photoelectron spectroscopic studies of thin film oxides of cobalt and molybdenum*. Surface and Interface Analysis, 1990. **15**(4): p. 265-272.
144. Battistoni, C., et al., *Octahedral vs tetrahedral coordination of the co(II) ion in layer compounds: Co_xZn_{1-x}In₂S₄ (0 ≤ x ≤ 0.46) solid solution*. Journal of Physics and Chemistry of Solids, 1986. **47**(9): p. 899-903.
145. de Jong, A.M., et al., *Sulfidation mechanism by molybdenum catalysts supported on silica/silicon(100) model support studied by surface spectroscopy*. The Journal of Physical Chemistry, 1993. **97**(24): p. 6477-6483.
146. Kasztelan, S., et al., *Preparation of Co-Mo-γAl₂O₃ and Ni-Mo-γAl₂O₃ catalysts by ph regulation of molybdenum solution. characterization of supported species and hydrogenation activities*. Applied Catalysis, 1983. **7**(1): p. 91-112.

147. Sun, Y., et al., *Atomically-thin two-dimensional sheets for understanding active sites in catalysis*. Chemical Society Reviews, 2015. **44**(3): p. 623-636.
148. Meng, J., et al., *Efficient $MMoO_4$ ($M = Co, Ni$) carbon cloth electrodes for water oxidation*. Inorganic Chemistry Frontiers, 2017. **4**(11): p. 1791-1797.
149. Zhang, W., et al., *A facile ion-conversion-exchange strategy for designing nitrogen-doped $CoMoO_4@Co_3O_4$ double-shell nanoboxs: A competitive candidate for supercapacitor and oxygen evolution reaction*. Journal of Energy Storage, 2023. **57**: p. 106170.
150. Wu, Z., et al., *Facile synthesis and excellent electrochemical performance of reduced graphene oxide- Co_3O_4 yolk-shell nanocages as a catalyst for oxygen evolution reaction*. Journal of Materials Chemistry A, 2016. **4**(35): p. 13534-13542.
151. Bao, W., et al., *Interface engineering of the $NiCo_2O_4@MoS_2/TM$ heterostructure to realize the efficient alkaline oxygen evolution reaction*. International Journal of Hydrogen Energy, 2023. **48**(33): p. 12176-12184.
152. Pei, X., et al., *Ion-change promoting Co nanoparticles@N-doped carbon framework on Co_2SiO_4/rGO support forming "double-triple-biscuit" structure boosts oxygen evolution reaction*. Carbon Neutralization, 2023. **2**(1): p. 115-126.
153. Yang, L., et al., *Metal-Organic-Framework-Derived Hollow $CoS_x@MoS_2$ Microcubes as Superior Bifunctional Electrocatalysts for Hydrogen Evolution and Oxygen Evolution Reactions*. ACS Sustainable Chemistry & Engineering, 2018. **6**(10): p. 12961-12968.
154. Liang, D., et al., *MOFs-derived core-shell $Co_3Fe_7@Fe_2N$ nanoparticles supported on rGO as high-performance bifunctional electrocatalyst for oxygen reduction and oxygen evolution reactions*. Materials Today Energy, 2020. **17**: p. 100433.
155. Abd-Elrahim, A.G. and D.-M. Chun, *Nanosized $Co_3O_4-MoS_2$ heterostructure electrodes for improving the oxygen evolution reaction in an alkaline medium*. Journal of Alloys and Compounds, 2021. **853**: p. 156946.
156. Li, Y., et al., *A novel strategy to synthesize $CoMoO_4$ nanotube as highly efficient oxygen evolution reaction electrocatalyst*. Catalysis Communications, 2019. **131**: p. 105800.
157. Guangzhi, Y., et al., *Three-dimensional crumpled reduced graphene oxide/ Co_9S_8 nanocomposites as efficient electrocatalyst for oxygen evolution reaction*. Journal of Alloys and Compounds, 2022. **905**: p. 164253.
158. Suliman, M.A., et al., *Interfacial coupling of amorphous cobalt boride with g- C_3N_4 nanosheets for superior oxygen evolution reaction*. Materials Letters, 2020. **268**: p. 127593.
159. Borthakur, P., et al., *CoS_2 Nanoparticles Supported on rGO, g- C_3N_4 , BCN, MoS_2 , and WS_2 Two-Dimensional Nanosheets with Excellent Electrocatalytic Performance for Overall Water Splitting: Electrochemical Studies and DFT Calculations*. ACS Applied Energy Materials, 2021. **4**(2): p. 1269-1285.
160. Hu, M., Z. Yao, and X. Wang, *Graphene-Based Nanomaterials for Catalysis*. Industrial & Engineering Chemistry Research, 2017. **56**(13): p. 3477-3502.
161. Ganesan, V. and J. Kim, *Multi-shelled CoS_2-MoS_2 hollow spheres as efficient bifunctional electrocatalysts for overall water splitting*. International Journal of Hydrogen Energy, 2020. **45**(24): p. 13290-13299.

162. Li, Y., et al., *Abundant heterointerfaces in MOF-derived hollow CoS₂-MoS₂ nanosheet array electrocatalysts for overall water splitting*. Journal of Energy Chemistry, 2021. **57**: p. 99-108.
163. Xiong, Q., et al., *Cobalt Covalent Doping in MoS₂ to Induce Bifunctionality of Overall Water Splitting*. Advanced Materials, 2018. **30**(29): p. 1801450.
164. Zhao, Z.-Y., et al., *Co-Modified MoS₂ Hybrids as Superior Bifunctional Electrocatalysts for Water Splitting Reactions: Integrating Multiple Active Components in One*. Advanced Materials Interfaces, 2019. **6**(11): p. 1900372.
165. Yang, J., et al., *MoS₂-CoS₂ heteronanosheet arrays coated on porous carbon microtube textile for overall water splitting*. Journal of Power Sources, 2021. **514**: p. 230580.
166. Tong, Y., et al., *Nitrogen-Incorporated Cobalt Sulfide/Graphene Hybrid Catalysts for Overall Water Splitting*. ChemSusChem, 2020. **13**(18): p. 5112-5118.
167. Tao, B., et al., *An MoS₂/NiCo₂O₄ composite supported on Ni foam as a bifunctional electrocatalyst for efficient overall water splitting*. Journal of Physics and Chemistry of Solids, 2021. **150**: p. 109842.
168. Lee, W.H., et al., *Electrode reconstruction strategy for oxygen evolution reaction: maintaining Fe-CoOOH phase with intermediate-spin state during electrolysis*. Nature Communications, 2022. **13**(1): p. 605.
169. Schenck, C.V., J.G. Dillard, and J.W. Murray, *Surface analysis and the adsorption of Co(II) on goethite*. Journal of Colloid and Interface Science, 1983. **95**(2): p. 398-409.
170. Wang, Q., et al., *Sulfur vacancies engineered self-supported Co₃S₄ nanoflowers as an efficient bifunctional catalyst for electrochemical water splitting*. Applied Catalysis B: Environmental, 2023. **322**: p. 122104.
171. Song, J., et al., *A review on fundamentals for designing oxygen evolution electrocatalysts*. Chemical Society Reviews, 2020. **49**(7): p. 2196-2214.
172. Jana, J., et al., *Designing a bimetallic transition metal oxide/hydroxide composite for effective electrocatalytic oxygen evolution reaction*. Applied Surface Science, 2021. **562**: p. 150253.
173. Swathi, S., et al., *Rare earth metal (Sm)-doped NiMnO₃ nanostructures for highly competent alkaline oxygen evolution reaction*. Nanoscale Advances, 2022. **4**(11): p. 2501-2508.
174. Karuppasamy, K., et al., *Revealing the effect of various organic ligands on the OER activity of MOF-derived 3D hierarchical cobalt oxide @ carbon nanostructures*. Journal of Alloys and Compounds, 2023. **934**: p. 167909.
175. Liu, Y., et al., *Nickel/Nickel Oxide-Nitrogen Self-Doped Carbon Nanosheets for Electrocatalytic Oxygen and Hydrogen Evolution Reactions*. ACS Applied Nano Materials, 2022. **5**(2): p. 2953-2961.
176. Kang, S., et al., *Transition Metal Compounds on Functionalized Multiwall Carbon Nanotubes for the Efficient Oxygen Evolution Reaction*. ACS Applied Nano Materials, 2023. **6**(6): p. 4319-4327.
177. Wang, Z., et al., *S-Doped Ni_{0.5}Co_{0.5}Fe₂O₄ Porous Single-Crystalline Nanosheets for Electrocatalytic Oxygen Evolution*. ACS Applied Nano Materials, 2024. **7**(6): p. 6196-6204.

178. Flores-Lasluisa, J.X., et al., *Transition metal oxides with perovskite and spinel structures for electrochemical energy production applications*. Environmental Research, 2022. **214**: p. 113731.
179. Zhang, Y., et al., *Regulation Strategy of Transition Metal Oxide-Based Electrocatalysts for Enhanced Oxygen Evolution Reaction*. Accounts of Materials Research, 2022. **3**(10): p. 1088-1100.
180. Zhu, K., et al., *The roles of oxygen vacancies in electrocatalytic oxygen evolution reaction*. Nano Energy, 2020. **73**: p. 104761.
181. Huang, H. and J.-J. Zhu, *The electrochemical applications of rare earth-based nanomaterials*. Analyst, 2019. **144**(23): p. 6789-6811.
182. Wang, X., et al., *Recent advances in rare-earth-based materials for electrocatalysis*. Chem Catalysis, 2022. **2**(5): p. 967-1008.
183. Hosono, E., et al., *The Fabrication of an Upright-Standing Zinc Oxide Nanosheet for Use in Dye-Sensitized Solar Cells*. Advanced Materials, 2005. **17**(17): p. 2091-2094.
184. Joya, M.R., J.E. Alfonso, and L.C. Moreno, *Photoluminescence and Raman studies of α -MoO₃ doped with erbium and neodymium*. Current Science (Bangalore), 2019. **116**(10): p. 1690-1695.
185. Goel, R., R. Jha, and C. Ravikant, *Investigating the structural, electrochemical, and optical properties of p-type spherical nickel oxide (NiO) nanoparticles*. Journal of Physics and Chemistry of Solids, 2020. **144**: p. 109488.
186. Liu, S., et al., *Interfacial oxygen vacancies at Co₃O₄-CeO₂ heterointerfaces boost the catalytic reduction of NO by CO in the presence of O₂*. Applied Catalysis B: Environmental, 2023. **323**: p. 122151.
187. Mukhtar, A., et al., *Structural characterization of self-assembled chain like Fe-FeO_x Core shell nanostructure*. Nanoscale Research Letters, 2019. **14**(1): p. 308.
188. Sheikh, T.A., et al., *4-Hexylresorcinol sensor development based on wet-chemically prepared Co₃O₄@Er₂O₃ nanorods: A practical approach*. Journal of Industrial and Engineering Chemistry, 2018. **66**: p. 446-455.
189. Alam, M.W., et al., *Effect of Mo doping in NiO nanoparticles for structural modification and its efficiency for antioxidant, antibacterial applications*. Scientific Reports, 2023. **13**(1): p. 1328.
190. Prabakaran, D.D.M., et al., *Precipitation method and characterization of cobalt oxide nanoparticles*. Applied Physics A, 2017. **123**(4): p. 264.
191. Lassoued, A., et al., *Synthesis, structural, morphological, optical and magnetic characterization of iron oxide (α -Fe₂O₃) nanoparticles by precipitation method: Effect of varying the nature of precursor*. Physica E: Low-dimensional Systems and Nanostructures, 2018. **97**: p. 328-334.
192. Tavakkoli, M., et al., *Mesoporous Single-Atom-Doped Graphene-Carbon Nanotube Hybrid: Synthesis and Tunable Electrocatalytic Activity for Oxygen Evolution and Reduction Reactions*. ACS Catalysis, 2020. **10**(8): p. 4647-4658.
193. Song, K., et al., *Three-dimensional self-supported CuCo₂O₄ nanowires@NiO nanosheets core/shell arrays as an oxygen electrode catalyst for Li-O₂ batteries*. Journal of Materials Chemistry A, 2021. **9**(5): p. 3007-3017.

194. Liu, L., et al., *Probing the Crystal Plane Effect of Co₃O₄ for Enhanced Electrocatalytic Performance toward Efficient Overall Water Splitting*. ACS Applied Materials & Interfaces, 2017. **9**(33): p. 27736-27744.
195. Chuang, T.J., C.R. Brundle, and D.W. Rice, *Interpretation of the x-ray photoemission spectra of cobalt oxides and cobalt oxide surfaces*. Surface Science, 1976. **59**(2): p. 413-429.
196. Tan, B.J., K.J. Klabunde, and P.M.A. Sherwood, *X-ray photoelectron spectroscopy studies of solvated metal atom dispersed catalysts. Monometallic iron and bimetallic iron-cobalt particles on alumina*. Chemistry of Materials, 1990. **2**(2): p. 186-191.
197. Zhang, G., et al., *Constructing ultrathin CoP nanomeshes by Er-doping for highly efficient bifunctional electrocatalysts for overall water splitting*. Journal of Materials Chemistry A, 2019. **7**(10): p. 5769-5778.
198. Zhang, Y., et al., *Enhanced charge separation and conductivity of hematite enabled by versatile NiSe₂ nanoparticles for improved photoelectrochemical water oxidation*. Applied Materials Today, 2022. **28**: p. 101552.
199. Guan, D., et al., *Utilizing ion leaching effects for achieving high oxygen-evolving performance on hybrid nanocomposite with self-optimized behaviors*. Nature Communications, 2020. **11**(1): p. 3376.
200. Helen McCay, M., *Chapter 23 - Hydrogen: An Energy Carrier*, in *Future Energy (Second Edition)*, T.M. Letcher, Editor. 2014, Elsevier: Boston. p. 495-510.
201. Meng, Y., et al., *Recent advances in the application of phosphates and borates as electrocatalysts for water oxidation*. Materials Today Nano, 2020. **12**: p. 100095.
202. Rekha, P., S. Yadav, and L. Singh, *A review on cobalt phosphate-based materials as emerging catalysts for water splitting*. Ceramics International, 2021. **47**(12): p. 16385-16401.
203. Wang, Z., et al., *A facile co-precipitation synthesis of robust FeCo phosphate electrocatalysts for efficient oxygen evolution*. Electrochimica Acta, 2018. **264**: p. 244-250.
204. Duraivel, M., S. Nagappan, and K. Prabakar, *Anion intercalated nickel iron hydrogen phosphate hydrate for full water splitting application*. Renewable Energy, 2023. **219**: p. 119529.
205. Mishra, R.K., et al., *Potentialities of nanostructured SnS₂ for electrocatalytic water splitting: A review*. Journal of Alloys and Compounds, 2022. **921**: p. 166018.
206. Zhang, B., et al., *g-C₃N₄-modulated bifunctional SnO₂@g-C₃N₄@SnS₂ hollow nanospheres for efficient electrochemical overall water splitting*. Applied Surface Science, 2022. **589**: p. 153016.
207. Dong, C., et al., *Manipulating oxygenate adsorption on N-doped carbon by coupling with CoSn alloy for bifunctional oxygen electrocatalyst*. Green Energy & Environment, 2023. **8**(5): p. 1417-1428.

List of publications

1. Ngoc-Diem Huynh, Hur Seung Hyun, Kang Sung Gu. Tuning the dehydrogenation performance of dibenzyl toluene as liquid organic hydrogen carriers. *International Journal of Hydrogen Energy*. 2021;46:34788-96.
2. Ngoc-Diem Huynh, Jana Jayasmita, Nivetha Ravi, Van Phuc Tran, Chung Jin Suk, Hur Seung Hyun. 2D siloxene supported NiO/Co₃O₄ electrocatalyst for the stable and efficient hydrogen evolution reaction. *Current Applied Physics*. 2022;44:102-9.
3. Jana Jayasmita, Nivetha Ravi, Ngoc-Diem Huynh, Van Phuc Tran, Kang Sung Gu, Chung Jin Suk, Hur Seung Hyun. Improved kinetics of reduction of alkaline water on the g-CN-supported transition metal oxide/boride hetero-interface: A case study. *International Journal of Energy Research*. 2022;46:14979-93.
4. Ngoc-Diem Huynh, Choi Won Mook, Hur Seung Hyun. Exploring the Effects of Various Two-Dimensional Supporting Materials on the Water Electrolysis of Co-Mo Sulfide/Oxide Heterostructure. *Nanomaterials*2023.
5. Nivetha Ravi, Jana Jayasmita, Ravichandran S, Ngoc-Diem Huynh, Van Phuc Tran, Chung Jin Suk, Hur Seung Hyun, Two-dimensional bimetallic Fe/M- (Ni, Zn, Co and Cu) metal organic framework as efficient and stable electrodes for overall water splitting and supercapacitor applications. *Journal of Energy Storage*. 2023;61:106702.
6. Ngoc-Diem Huynh, Jana Jayasmita, Hur Seung Hyun, Influence of Er₂O₃ on Transition Metal Oxides in Water oxidation application (*Under review*).